ANL-12/21

Crack Growth Rate Testing of Alloy 600 Nozzle Sections from the Replacement Pressure Vessel Head at Davis-Besse Reactor

Nuclear Engineering Division

About Argonne National Laboratory
Argonne is a U.S. Department of Energy laboratory managed by UChicago Argonne, LLC under contract DE-AC02-06CH11357. The Laboratory's main facility is outside Chicago, at 9700 South Cass Avenue, Argonne, Illinois 60439. For information about Argonne and its pioneering science and technology programs, see www.anl.gov.

DOCUMENT AVAILABILITY

Online Access: U.S. Department of Energy (DOE) reports produced after 1991 and a growing number of pre-1991 documents are available free via DOE's SciTech Connect (http://www.osti.gov/scitech/)

Reports not in digital format may be purchased by the public from the National Technical Information Service (NTIS):
U.S. Department of Commerce
National Technical Information Service
5301 Shawnee Rd
Alexandra, VA 22312
www.ntis.gov
Phone: (800) 553-NTIS (6847) or (703) 605-6000
Fax: (703) 605-6900
Email: **orders@ntis.gov**

Reports not in digital format are available to DOE and DOE contractors from the Office of Scientific and Technical Information (OSTI):
U.S. Department of Energy
Office of Scientific and Technical Information
P.O. Box 62
Oak Ridge, TN 37831-0062
www.osti.gov
Phone: (865) 576-8401
Fax: (865) 576-5728
Email: **reports@osti.gov**

Disclaimer
This report was prepared as an account of work sponsored by an agency of the United States Government. Neither the United States Government nor any agency thereof, nor UChicago Argonne, LLC, nor any of their employees or officers, makes any warranty, express or implied, or assumes any legal liability or responsibility for the accuracy, completeness, or usefulness of any information, apparatus, product, or process disclosed, or represents that its use would not infringe privately owned rights. Reference herein to any specific commercial product, process, or service by trade name, trademark, manufacturer, or otherwise, does not necessarily constitute or imply its endorsement, recommendation, or favoring by the United States Government or any agency thereof. The views and opinions of document authors expressed herein do not necessarily state or reflect those of the United States Government or any agency thereof, Argonne National Laboratory, or UChicago Argonne, LLC.

ANL-12/21

Crack Growth Rate Testing of Alloy 600 Nozzle Sections from the Replacement Pressure Vessel Head at Davis-Besse Reactor

prepared by
B. Alexandreanu, Y. Chen, K. Natesan and W. J. Shack
Nuclear Engineering Division
Argonne National Laboratory

February 2012

Abstract

In the last decade there have been two inspections which have identified primary water stress corrosion cracking (SCC) at the Davis-Besse plant. The current report presents crack growth rate (CGR) and corrosion fatigue data obtained from tests on Davis-Besse material (Alloy 600) removed from the replacement reactor pressure vessel head. Intergranular (IG) cracking was extensive in the test samples. Secondary cracks, crack branching, and ligaments were also observed. The fracture surface also revealed IG cracking under fatigue precracking in primary water. Most of the SCC CGRs appear to rank at the 75th percentile, and can be as high as 90th percentile when compared to an industry database of Alloy 600 crack growth rates. The activation energy for SCC growth in the replacement material is similar to that of typical Alloy 600.

Contents

Abstract **3**

Executive Summary **5**

1 Introduction **7**

2. Experimental **11**

2.1. Metallography analysis 11

2.2. CT Specimens 11

2.3. PWSCC Test Facilities 13

2.4. CGR Test Methodology 16

2.5. Analysis of Crack Growth Rate Data 18

3 Microstructural Characterization **21**

4. Results **24**

4.1. Specimen DB-5 24

4.2. Specimen DB-4 47

4.3. Specimen DB-3 61

5. Discussion **74**

5.1. Cyclic CGRs 74

5.2. SCC CGRs 75

5.3. Microstructural Analysis 77

5.4. Activation Energy for SCC Growth 79

6 Conclusion **81**

Aknowledgments **82**

References **83**

Executive Summary

Over the past ten years at the Davis-Besse Nuclear Power Plant, primary water stress corrosion cracking (PWSCC) flaws in reactor pressure vessel (RPV) upper head penetrations have been identified in two different RPV heads. In March 2002, borated water was found to have leaked from cracked control rod drive mechanisms (CRDMs) directly above the reactor, and this leak led to significant degradation of the ferritic steel head.[1] In March 2010, during a scheduled refueling outage, ultrasonic examinations performed on the CRDM nozzles found that twelve of the nozzles inspected did not meet acceptance criteria. Subsequent examinations found new cracks in 24 vessel head penetrations and associated welds, including one substantial enough to leak boric acid. After both incidents, material from the affected nozzles was harvested and tested at Argonne National Laboratory (ANL) to determine whether the stress corrosion crack (SCC) growth rates are consistent with our understanding of this degradation phenomenon.

The current report presents the data obtained from tests on Davis-Besse material (Alloy 600 heat M7929) removed from the replacement RPV head that has been in use since 2004, and as of March 2010 had 5.5 effective full power years of operation. Following the March 2010 inspection, material from control rod drive mechanism (CRDM) nozzle #4, which was found to have a through wall indications was made available to the NRC, and testing of the nozzle material was initiated at ANL in November 2010. The objective of these tests was to determine the SCC crack growth rates (CGRs) of the Alloy 600 CRDM nozzles in the replacement RPV upper head. The measured CGRs were compared to the results from the nozzle #3 from the original head (Alloy 600 heat M3935) that was previously tested at ANL[2] and the disposition curve for alloy 600 base material that was proposed by industry.[3] The experimental approach is typical of that used in all SCC CGR tests at ANL and consists of in-situ fatigue precracking transitioning to SCC cracking, and multiple measurements of PWSCC CGRs.

Testing at ANL enabled the measurement of both cyclic and PWSCC CGRs under several loading conditions on three samples cut from the replacement Davis-Besse CRDM nozzle #4 (Alloy 600 heat M7929) in two orientations. Following testing in a pressurized water reactor (PWR) environment, the cross sections and fracture surfaces were examined. The findings can be summarized as follows:

1. The mechanical fatigue behavior of the Alloy 600 heat M7929 removed from CRDM nozzle #4 in the replacement Davis-Besse RPV head appears similar to that of most Alloy 600 materials. However, the environmental enhancement of cyclic rates is higher than expected for typical Alloy 600. The corrosion fatigue behavior appears similar to that for Alloy 600 heat M3935 removed from CRDM nozzle #3 of the original Davis-Besse RPV head and previously tested at ANL.[2]

2. Most of the SCC CGRs obtained on the Alloy 600 from the replacement Davis-Besse RPV head CRDM nozzle #4 appear to rank at the 75th to as high as the 90th percentile of crack growth rate data obtained for multiple alloy 600 heats (EPRI MRP-55 disposition curve).[3] The crack

[1] U.S. NRC Information Notice 2002–11, "Recent Experience with Degradation of Reactor Pressure Vessel Head," March 12, 2002.

[2] Alexandreanu, B., O. K. Chopra, and W. J. Shack, "Crack Growth Rates of Nickel Alloys from the Davis-Besse and V. C. Summer Power Plants in a PWR Environment," NUREG/CR-6921, ANL-05/55, November 2005.

[3] PWR Materials Reliability Program Alloy 600 Issues Task Group, "Materials Reliability Program (MRP) Crack Growth Rates for Evaluating Primary Water Stress Corrosion Cracking (PWSCC) of Thick-Wall Alloy 600 Materials," MRP-55, Revision 1, Electric Power Research Institute, Palo Alto, CA, 2002.

propagation direction (circumferential-longitudinal vs. circumferential-radial, consistent with the ASTM E616 Criteria) does not seem to affect the measured CGRs.

3. The activation energy for SCC growth in the Alloy 600 heat M7929 removed from CRDM nozzle #4 in the replacement Davis-Besse RPV head appears similar to that of typical Alloy 600.

4. The post-test examination of the cross section and fracture surface of the specimens revealed that intergranular (IG) cracking was extensive. Secondary cracks, crack branching, and ligaments were observed.

5. The fracture surface revealed IG cracking under fatigue precracking in primary water. This behavior is not usually observed in Alloy 600, and has only been observed in the Davis-Besse nozzle #3 specimens tested previously.[2] This observation is consistent with the increased PWSCC susceptibility of these Alloy 600 heats.

6. The microstructure Alloy 600 heat M7929 was examined and found to have a largely carbide-free grain boundary network. Instead, the carbides decorate what seem to be the ghost boundaries of a prior network. By contrast, Alloy 600 heat M3935 removed from CRDM nozzle #3 of the original Davis-Besse RPV head had an adequate grain-boundary carbide decoration. Based on only the difference in microstructures the lack of grain boundary carbides, Alloy 600 heat M7929 used in CRDM nozzle #4 in the replacement RPV head appears to be more susceptible to SCC than Alloy 600 heat M3935 used in CRDM nozzle #3 of the original RPV head.

1 Introduction

In a nuclear reactor, the fission process can be controlled using the control rods, which are raised or lowered by the control rod drive mechanisms (CRDMs). The control rods have a high boron content which absorbs neutrons, hence, lowering the control rods into the core of the reactor slows down the fission process and reduces the reactor power output. During operation, the control rods are usually removed from the reactor, and the operators and safety systems use the full insertion of the control rods to shutdown the reactor. The CRDMs are mounted on nozzles welded to the reactor pressure vessel (RPV) head (Fig. 1).

CRDM penetrations in the RPV closure heads are one of the major locations of component PWSCC.[1] In the fall of 1991, during an over–pressurization test, a leak was discovered in the CRDM nozzle at the Bugey 3 plant in France. Subsequent inspections of CRDM penetrations in the early 1990s in foreign PWRs indicated that ≈6.5% of the nozzles in French plants had axial cracks on the nozzle inner surface, while only ≈1.25% of the nozzles that were inspected in other plants had axial cracks.[2] Inspection of the CRDM nozzles in seven plants in the U.S. (Point Beach 1, Oconee 2, Cook 2, Palisades, North Anna 1, Millstone 2, and Ginna) at this time suggested that the cracking was much less frequent than in the French plants. None of the cracks found in U.S. plants was through–wall, and until late 2000, no additional leaks occurred in pressure–vessel head penetrations. In November 2000, leaks from axial through–wall cracks were identified at Oconee Unit 1 and, in February 2001, at Arkansas Nuclear One Unit 1.[3] During the next 15 months, inspections at Oconee Units 2 and 3 and followup inspection at unit 1 identified both axial and circumferential cracks in reactor–vessel head penetrations.[4] The presence of circumferential cracks, in particular, raised concerns regarding structural integrity.[5,6] Cracks have also been found in pressure–vessel head penetrations at North Anna Unit 2.[7]

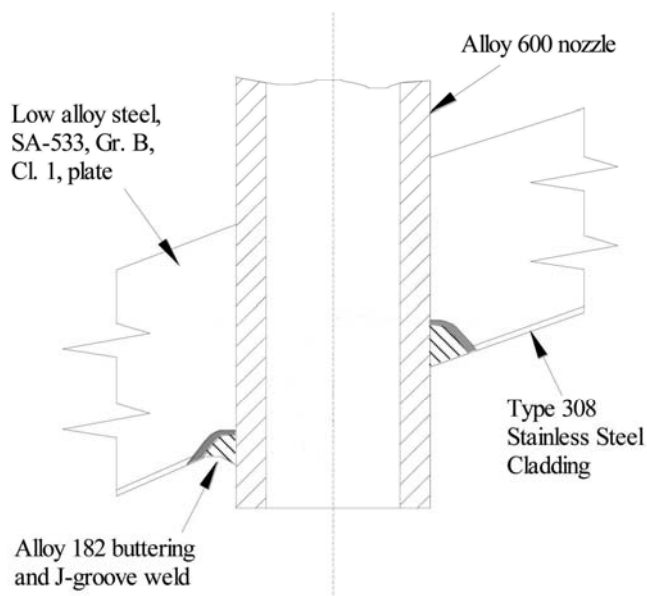

Figure 1.

Schematic of the CRDM nozzle – RPV head weld.

In the last decade there have been two occurrences of PWSCC at the Davis-Besse plant. In March 2002, the borated water had leaked from cracked CRDMs and led to significant degradation of the ferritic steel head.[8] As such, downstream of nozzle #3, a triangular cavity, about 127 mm [5 in] wide and 178 mm [7 in] long, had penetrated completely through the thickness of the low-alloy steel reactor pressure vessel head, leaving only a layer of SS cladding. After the 2002 occurrence, Davis-Besse received a replacement head from a mothballed reactor in Midland, Michigan, before restarting in 2004.

In March 2010, during a scheduled refueling outage, ultrasonic examinations performed on the CRDM nozzles found that tweleve of the nozzles inspected did not meet acceptance criteria. Subsequent examinations found indications of cracking in 24 of 69 nozzles and associated J-groove welds, including at least one flaw in the alloy 600 nozzle material that was substantial enough to leak primary coolant. After both occurrences, material from the affected nozzles was harvested and tested at Argonne National Laboratory (ANL) to determine SCC growth rates and material microstructure.

The metallographic examination and SCC testing of nozzle #3 material (Alloy 600 heat M3935) was conducted at ANL in 2003-2004.[9] The nozzle piece that was made available to ANL consisted of a 2.5”-long ring resulting from cuts at 2.5 cm [1 in] and 8.9 cm [3.5 in] from the bottom of the nozzle (Fig. 1). The metallographic examination found a relatively uniform microstructure with adequate grain boundary carbide coverage. In light of these findings, the results of the SCC tests were rather surprising. These will be briefly summarized in this section.

The testing approach at ANL allows for the determination of both environmental fatigue and SCC CGRs. Following PWSCC testing in primary water, the fracture surface of each specimen is examined. Figure 2 shows the cyclic CGRs for the Alloy 600 nozzle material measured in the PWR environment as a function of the rates expected in air under the same loading conditions. The deviation from the first diagonal is a measure of environmental enhancement. The results indicate that the fatigue behavior is consistent with that expected for Alloy 600; however, subsequent, gentler loading conditions lead to significant environmental enhancement of the cyclic CGRs. Hence, it was decided that the corrosion fatigue curve developed for generic Alloy 600[10] underestimates the observed behavior, and a new curve was generated to describe the unique behavior of this particular heat of material.[9] As evident in Fig. 3, the SCC CGRs were higher than predicted by the proposed CGR disposition curve for Alloy 600,[11] which is based on a 75th percentile estimate using all the available Alloy 600 data. The measured SCC CGRs were found to correspond to ≈95th percentile values of the available data. The fact that this alloy exhibits such high environmental enhancement of the cyclic CGRs was further substantiated by the analysis of the fracture surface. As shown in Fig. 4, this material exhibits an intergranular (IG) fracture mode even during precracking under cyclic loading. The fracture started in a transgranular (TG) fracture mode, but changed to intergranular almost at the first grain boundary encountered (Figs. 4a and b). For the remainder of the test the fracture mode remained exclusively smooth IG (Fig. 4c). An IG fracture mode during precracking is uncommon and suggests higher than average susceptibility to IG SCC.

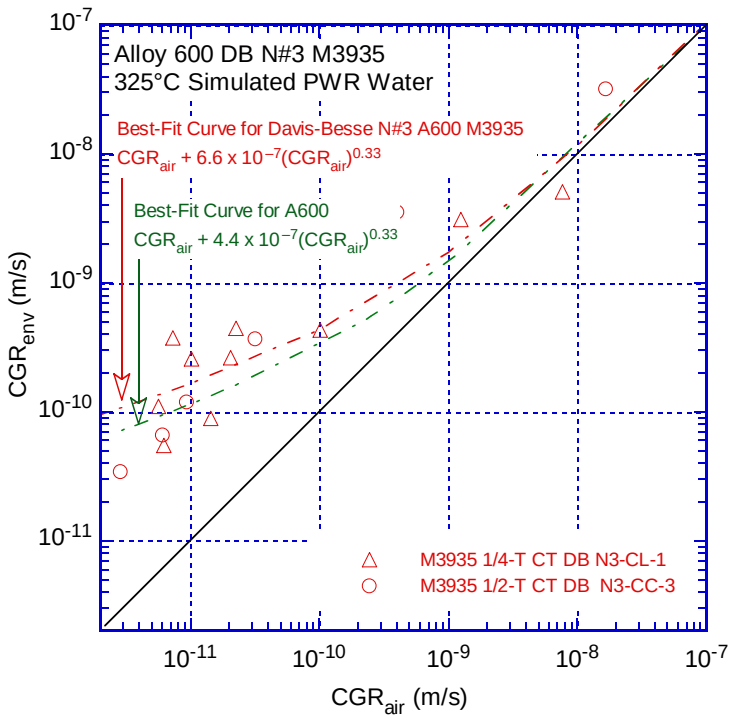

Figure 2.

Cyclic CGRs for Alloy 600 heat M3935 from DB nozzle #3.[9] Corrosion fatigue curves for typical Alloy 600 (green)[10], and Alloy 600 heat M3935 (red)[9] are included.

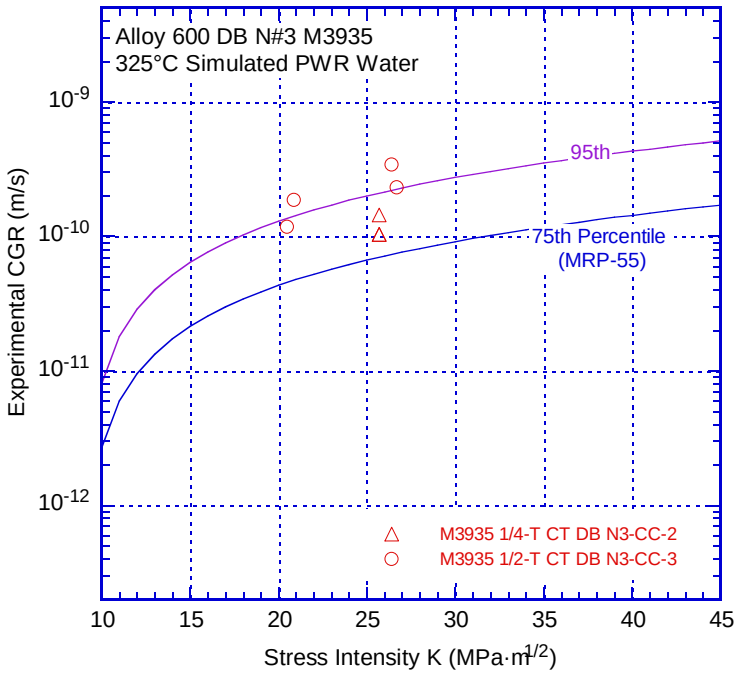

Figure 3.

SCC CGR data for Alloy 600 heat M3935 from the original Davis-Besse nozzle #3.[9] Proposed disposition curves[11] for 75th and 95th percentiles are shown.

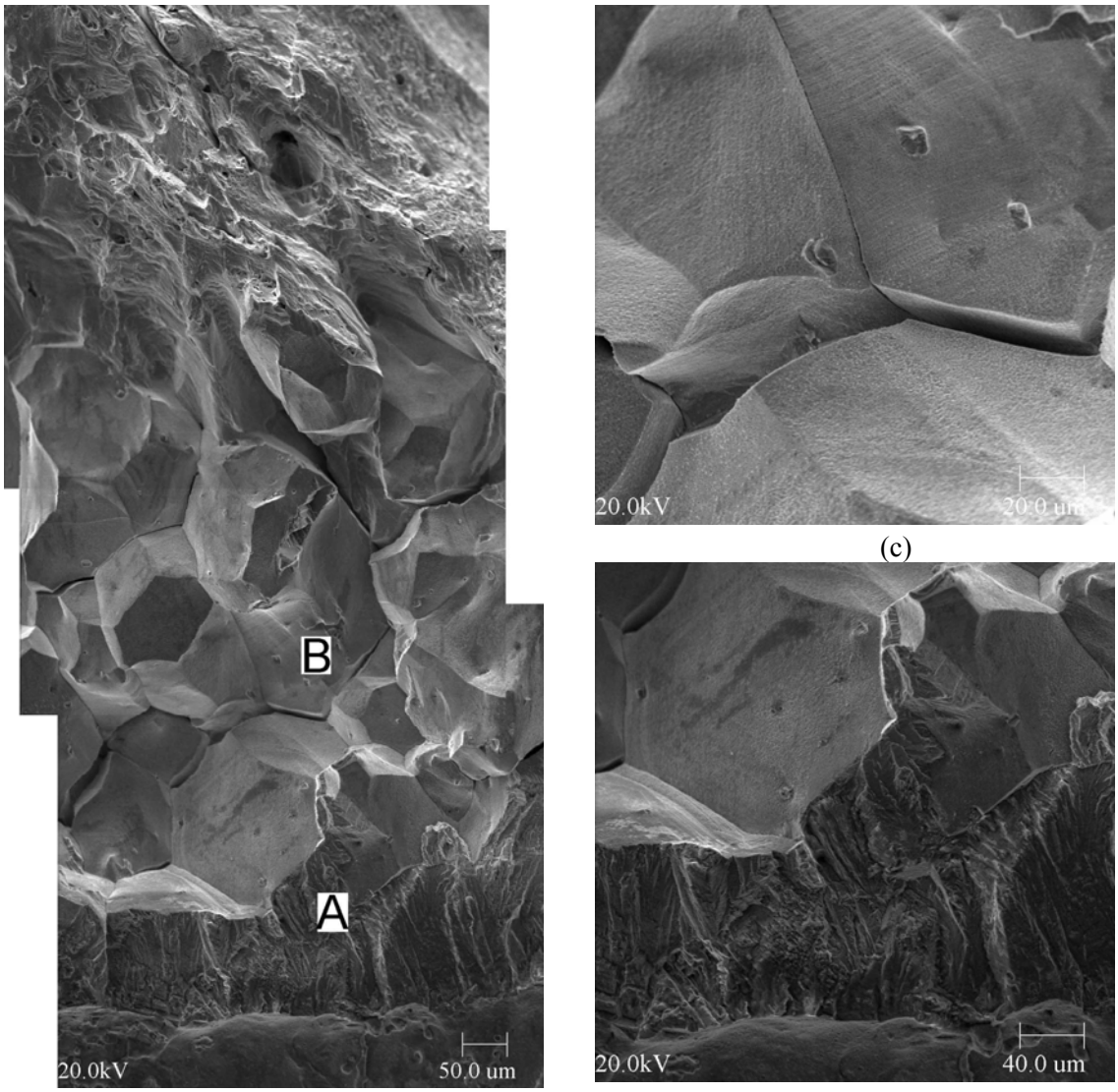

(a) (b) (c)

Figure 4. Fracture surface of Alloy 600 heat M3935 Davis-Besse Specimen N3CC-2[9] (a), and high-magnification micrographs at locations A (b) and B (c).

Following the March 2010 inspection, material from the replacement head CRDM nozzle #4 (Alloy 600 heat M7929) was made available to the ANL staff in November 2010. The specific objective of the tests was to determine the SCC CGRs for the replacement material and compare the results with those from the nozzle #3 (Alloy 600 heat M3935) reported by ANL in 2005,[9] as these alloys share a common manufacturer (Babcock & Wilcox Tubular Products Divison), are approximately of the same vintage, and likely received a similar heat treatment with a final mill anneal estimated at 871-927ºC (1600-1700ºF).[12] For a broader perspective, the results were also compared with the industry-proposed disposition curve for Alloy 600.[11] The experimental approach was typical of that used in all SCC CGR tests at ANL, and mirrored the approach used previously for the original nozzle #3 material testing. In this approach, precracking is conducted in-situ to verify the well-established fatigue behavior of the alloy. Next, the specimen is transitioned to SCC cracking by increasing the load ratio and rise times. Cyclic CGRs are continuously monitored and compared with the corrosion fatigue data available for this alloy. Finally, SCC CGRs are determined at constant load or constant load with periodic unloading.

2. Experimental

The crack growth rate tests on the Davis-Besse replacement nozzle #4 material (Alloy 600 heat M7929) were conducted in simulated PWR environments at temperatures of 290-350°C [554-662°F] in accordance with American Society for Testing and Materials (ASTM) Designation E 647, "Standard Test Method for Measurement of Fatigue Crack Growth Rates," and ASTM E-1681,[13] "Standard Test Method for Determining a Threshold Stress Intensity Factor for Environment-Assisted Cracking of Metallic Materials under Constant Load."[14] Depending on the dimensions of the available material and the desired crack direction with respect to the nozzle, the tests were performed on either 1/2-T or 1/4-T compact tension (CT) specimens. This section describes the materials used, provides the specimen configurations, and describes the CGR test methodology.

2.1 Metallography analysis

For the metallography analysis, the coupons were cut from the Alloy 600 CRDM nozzle #4 (heat M7929) to expose the same plane orientation as the CT specimens used in the PWSCC tests. The coupons were mechanically polished, and the surfaces were finished with diamond suspensions of 9, 3 and 1 μm. In order to reveal the microstructure, the specimens were etched using Beraha's reagent consisting of 100 mL stock solution (1000 ml water, 200 ml HCl, 24 g NH4FHF) and 0.3 – 0.6 g $K_2S_2O_5$.

In addition, the cross sections of the CT specimens were examined post test to determine the crack path. For this purpose, the side surfaces were polished as just described, followed by a 5% nital solution etch to reveal the grain boundaries and the narrow cracks.

The microstructure and the fracture surfaces were examined using standard optical and scanning electron microscopy (SEM).

2.2 CT Specimens

The Davis-Besse nozzle #4 section (Alloy 600 heat M7929) was cut from the bottom of the nozzle (see schematic in Fig. 1), and was decontaminated at BWXT Inc. in Lynchburg, VA. Given the available material dimensions, five CT test specimens were machined following ANL specifications (Fig. 5) in two dimensions (½T CT and ¼T CT) and two orientations, circumferential-longitudinal (CL) and circumferential-radial (CR). Both ½T CT specimens are in the CL orientation, and all three ¼T CTs are in the CR orientation. The location of each specimen is shown in Fig. 6. Specimens marked DB 1-3 are in the CR orientation, and specimens DB-4 and DB-5 are in the CL orientation.

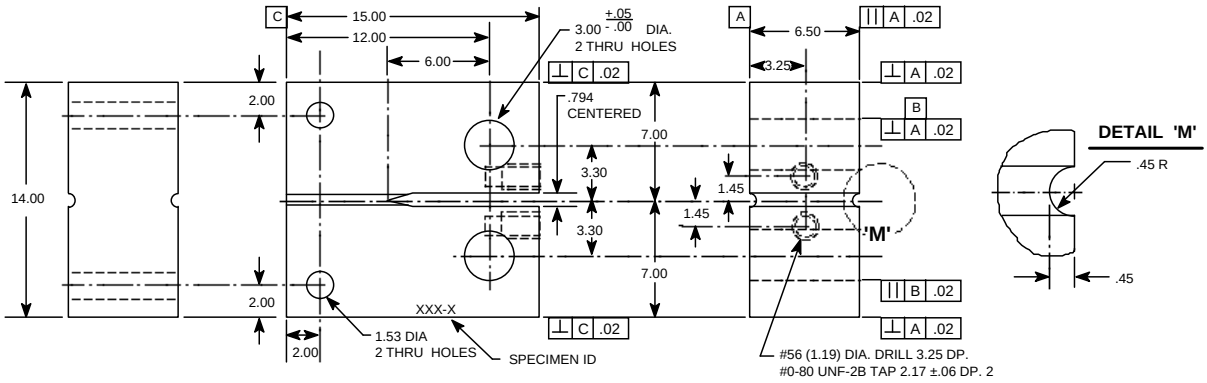

(a)

Figure 5. Configuration of (a) ¼T and (b) ½T CT specimens.

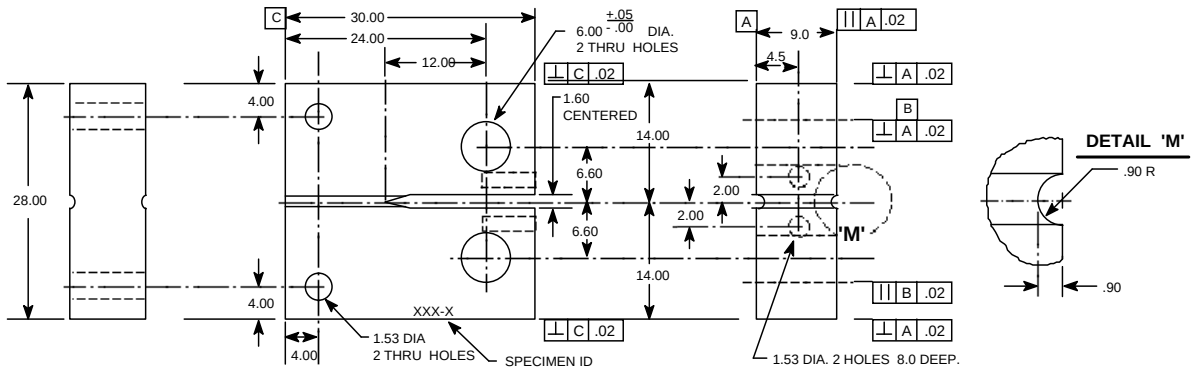

(b)

Figure 5. (Cont.)

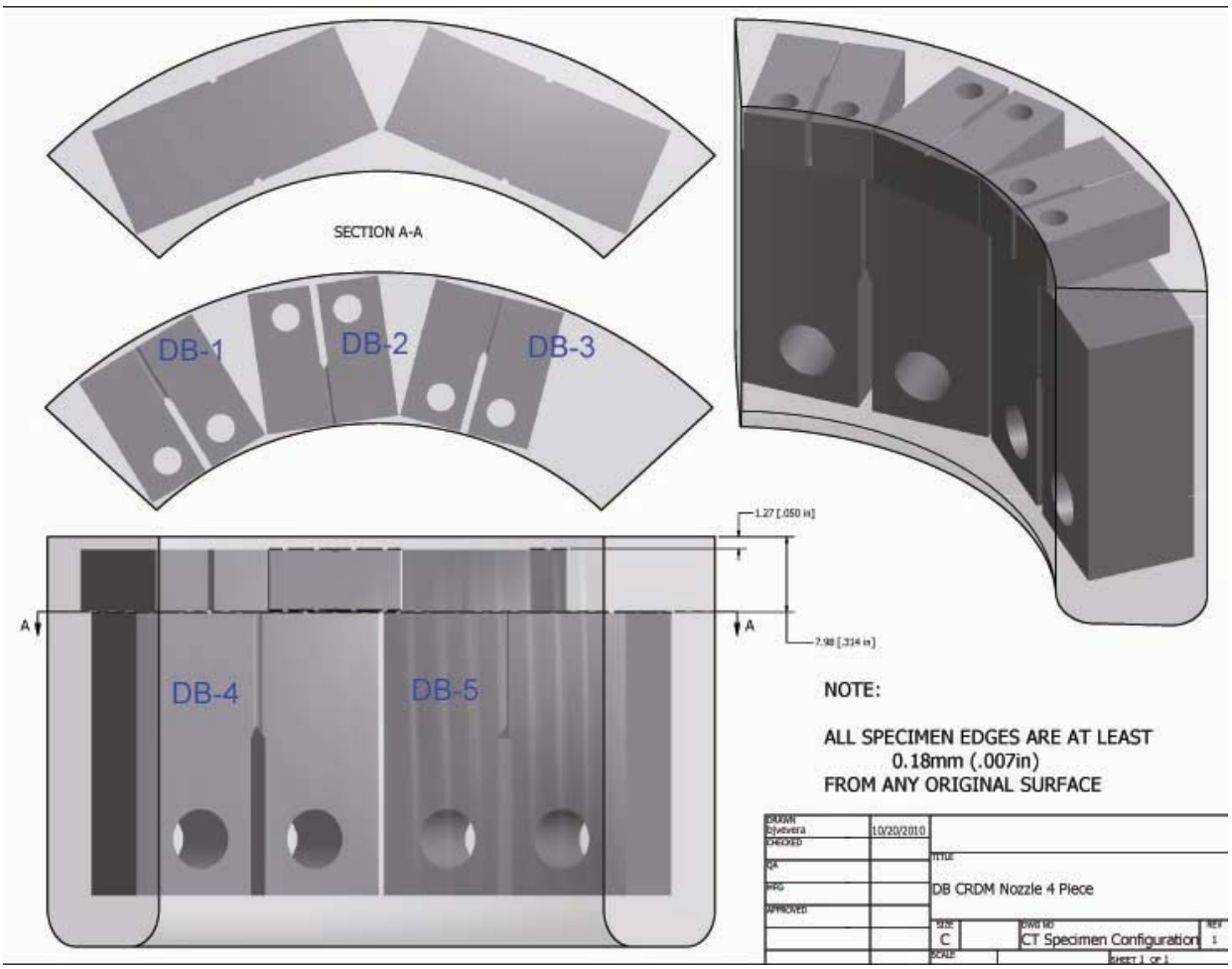

Figure 6. Location of test specimens in the Davis-Besse nozzle #4 section (Alloy 600 heat M7929)

The Health Physics staff at ANL reviewed the procedure used by BWXT to free-release potentially radioactive materials, and one Argonne HP staff travelled to the BWXT site in Lynchburg to observe the actual activity measurements. The specimens were next shipped to ANL, where an additional set of activity measurements was performed by HP personnel before they were free released to Argonne staff.

The dimensions of the CT test specimens were checked by the Central Shops Quality Control (QC) staff at ANL. In general, good agreement was found with the dimensions supplied by BWXT; however, on one ½T CT specimen (DB-4), the side grooves were found not to be parallel to each other; hence, on one side the specimen notch was almost outside the side groove. To make this specimen usable, the 0.15-mm discrepancy was corrected by enlarging the side grooves from 0.9 mm [0.035 in] to 1.6 mm [0.063 in]. Two sides of the specimen were also machined to make them parallel.

2.3 PWSCC Test Facilities

The CGR tests were conducted in two test facilities—one equipped with 2-liter stainless steel (SS) autoclave and one with a 6-liter SS autoclave. Each system has a suite of calibrated instrumentation, including digitally controlled hydraulic loading and load cells, and an independent water loop to maintain a simulated PWR environment with water chemistry monitoring. The test systems are nearly identical except for the maximum load rating of the test frame and the volume of the autoclave vessel. A detailed description of the test system with the 2-liter autoclave is provided in this section.

The 2-liter autoclave test facility allows test temperatures of up to 350°C [662°F]. Figure 7 is a photograph showing the entire test system. The servo-hydraulic test frame consists of a load train, an autoclave support frame, and autoclave. The hydraulic actuator is mounted on bottom of the test frame, with the load train components located above it. The load cell is located at the bottom of the pull rod. An Instron Model 8800 system is used to control the load on the specimen. The test temperature is maintained by heater bands mounted on the autoclave body.

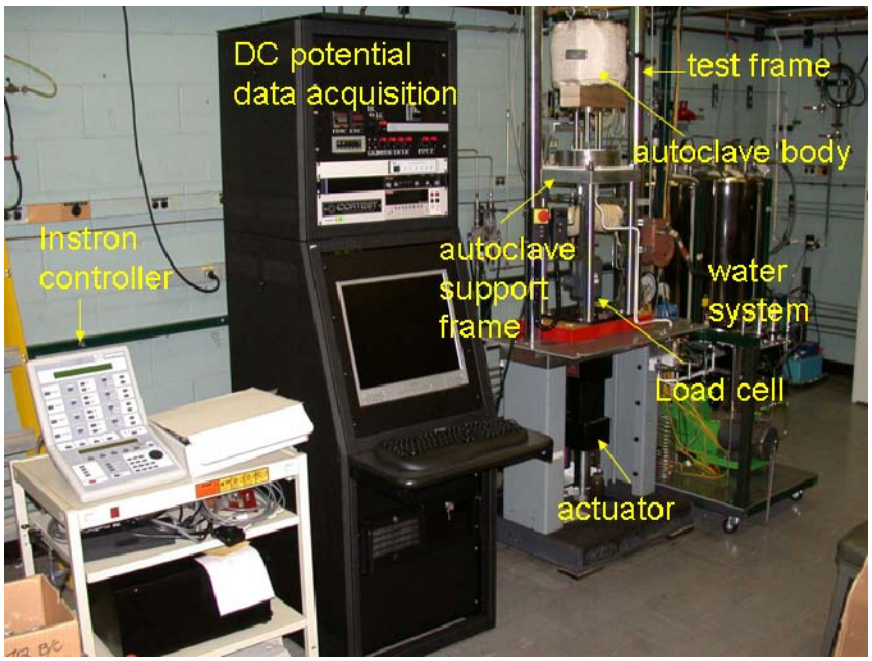

Figure 7. Layout of the 2-liter SCC test system.

The autoclave support frame consists of a thick plate supported by four compression rods (Fig.8). The internal load frame that contains the test specimen consists of a top plate supported by three rods. The upper two-piece clevis assembly is fastened to the top plate of the internal load frame, and the lower piece clevis assembly is connected to the pull rod. The specimen to be tested is mounted between the clevises. The specimen and clevises are kept electrically insulated from the load train by using oxidized Zircaloy pins and mica washers to connect the clevises to the rest of the load train. Water is circulated through a port in the autoclave head, which serves both as inlet and outlet. A schematic diagram of the recirculating water system is shown in Fig. 9.

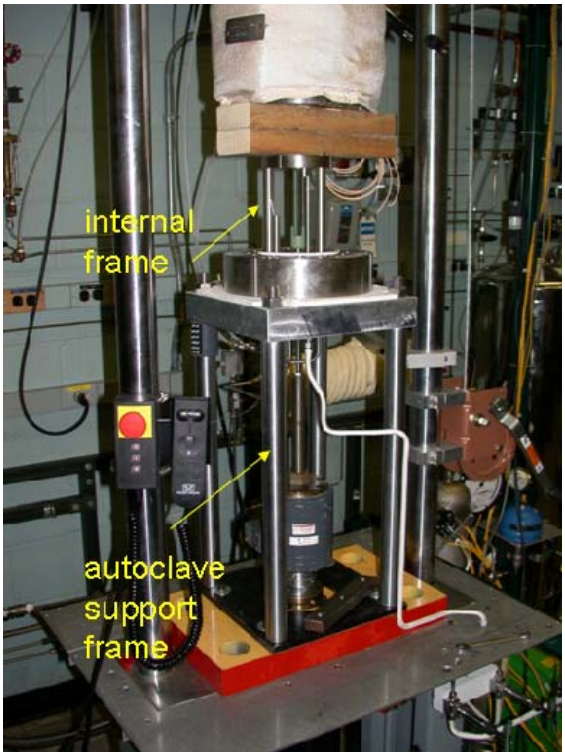

Figure 8.
Photograph of the specimen load train for the 2-liter autoclave.

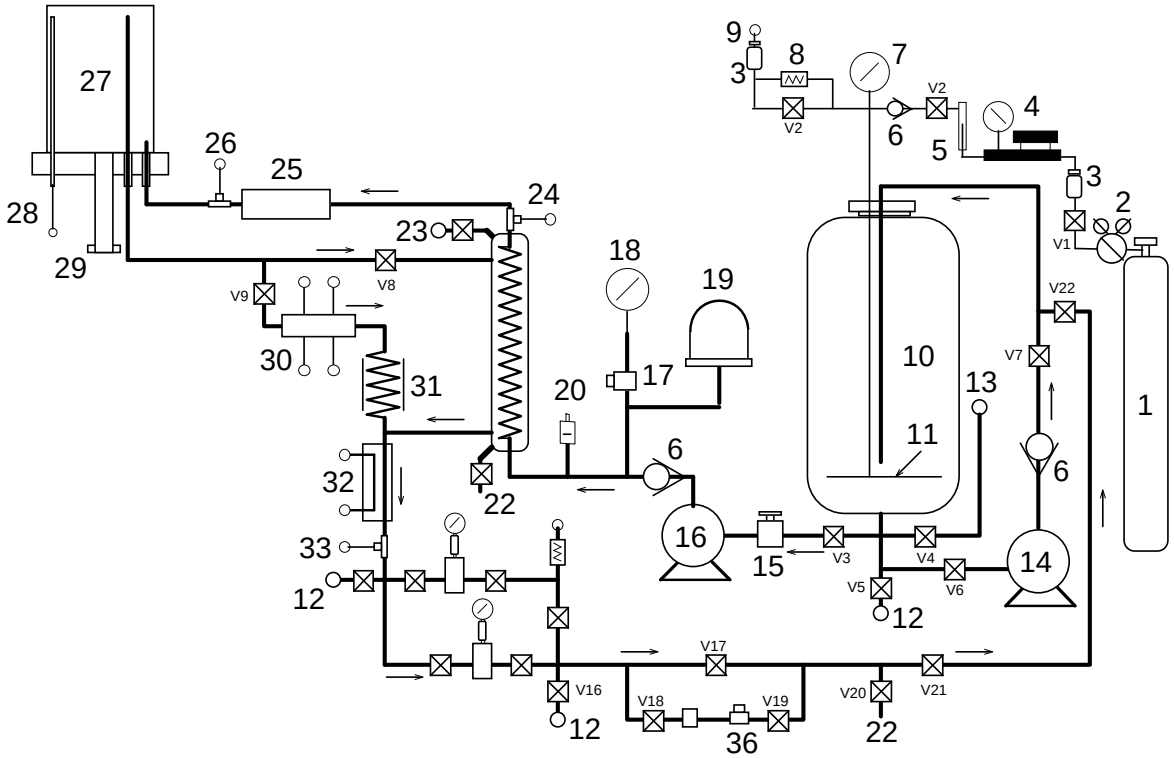

1. COVER GASS SUPPLY TANK
2. TWO-STAGE HIGH-PRESSURE REGULATOR
3. FLASH ARRESTOR
4. LOW-PRESSURE REGULATOR
5. FLOW METER
6. CHECK VALVE
7. COMPOUND VACUUM & PRESSURE GAUGE
8. PRESSURE RELIEF VALVE
9. VENT TO AIR & FLASH ARRESTOR
10. FEEDWATER STORAGE TANK
11. SPARGE TUBE
12. WATER SAMPLE PORT
13. FEEDWATER FILL PORT
14. FEEDWATER TANK RECIRCULATION PUMP
15. SOLENOID VALVE
16. HIGH-PRESSURE PUMP
17. PRESSURE TRANSDUCER
18. HIGH-PRESSURE GAUGE
19. ACCUMULATOR
20. RUPTURE DISC
21. HEAT EXCHANGER (HX)
22. DRAIN
23. SYSTEM BLEED PORT
24. HEAT EXCHANGER OUTLET TC
25. AUTOCLAVE PREHEATER
26. PREHEATER OUTLET TC
27. COMMERCIAL AUTOCLAVE
28. THERMOWELL
29. “BAL SEAL” RETAINER
30. ECP CELL
31. AIR-COOLED COIL
32. WATER COOLED HEAT EXCHANGER
33. BACK-PRESSURE REGULATOR (BPR) INLET TC
34. BPR
35. PH METER
36. CONDUCTIVITY METER

Figure 9. Schematic diagram of the recirculating 2-liter autoclave system.

The simulated PWR feedwater contains 2 ppm Li as LiOH, 1000 ppm B as HBO_3, ≈2 ppm dissolved hydrogen (≈23 cm^3/kg), and less than 10 ppb dissolved oxygen (DO).[15] Water is circulated at relatively low flow rates (15-25 mL/min). The test temperatures were 320°C [608°F] or 325°C [617°F]. Tests periods at temperatures different from those two were conducted at constant potential from the Ni/NiO line.[16]

Crack extensions are monitored by the reversing-DC potential difference method, Fig.10. In this method, a constant DC current is passed through the test specimen and the crack length is measured through the changes in the electrical voltage at the crack mouth. The electrical voltage measured across the crack mouth is related to the unbroken crack ligament resistance through the Ohm's law. Thus, as the crack advances, the length of the unbroken ligament decreases and its resistance increases. In short, as the crack advances the voltage measured across the crack mouth increases. Figure 10 shows a typical configuration of a CT specimen instrumented for crack growth measurements by the DC potential method: the current leads are welded on the top and bottom surfaces of the specimen, and potential leads are welded on the front face of the specimen across the machined notch but on diagonal ends. Also, to compensate for the effects of changes in resistivity of the material with time, an internal reference bar of the same material being tested is installed in series, near the test specimen. The voltage readings across the reference bar are used to normalize potential drop measurements for the CT test specimen. The changes potential drop measurements for the CT test specimen are transformed into crack advance data using correlations developed for the specimen geometry of interest. In practice, voltage readings are taken successively as the current is reversed, and, typically, 800 voltage readings are needed to generate 1 crack advance data point with a resolution of approximately 1-2 µm [0.039-0.079 mils].

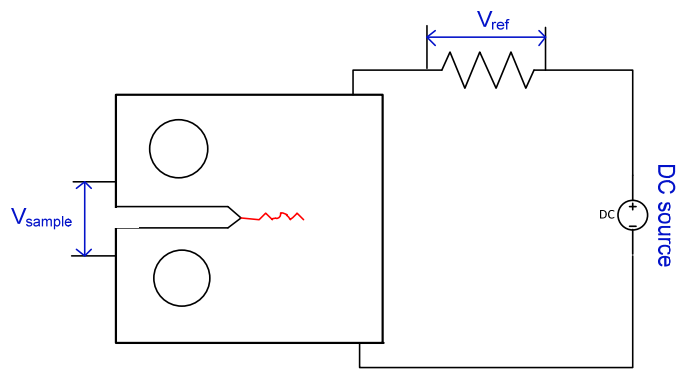

Figure 10. Principle of crack length measurement by the DC potential method.

2.4 CGR Test Methodology

A typical CGR test at ANL consists of three stages: in-situ precracking, transitioning to SCC, and the SCC growth stage. At the end of the test the specimen is broken open, and the fracture surface is examined. The objective of each stage will be highlighted next.

The objective of precracking is to produce a sharp crack tip. This is typically achieved by fatigue cracking, using a triangular waveform at load ratio R = 0.3[4], frequency of ≈1 Hz, and maximum stress intensity factor (K_{max}) of 20-25 MPa·m$^{1/2}$ [18.2-22.8 ksi·in$^{1/2}$]. Under rapid cyclic loading, the crack growth is dominated by mechanical fatigue; hence, the known fatigue behavior of the alloy being tested is expected to be reproduced. In turn, this step ensures that a straight crack front has been produced.

After approximately 0.5-mm (20 mils) extension in fatigue, the transitioning stage is initiated. The purpose of this stage is to transition from the fatigue/transgranular (TG) fracture mode to an SCC/intergranular (IG) fracture mode. As such, cycling is continued under loading conditions expected to foster environmental effects. In general, environmental enhancement of cyclic rates is typically observed under loading conditions that would lead to CGRs between 10^{-11} and 10^{-9} m/s in air. To generate these rates, the load ratio R is increased incrementally to 0.5-0.7, and the loading waveform is changed to a slow/fast sawtooth with rise times of 30-1000 s and unload time of 12 s. Transitioning to an

[4] Load ratio R = K_{min}/K_{max}

IG SCC fracture mode is assessed by analyzing the cyclic rates. The analysis, described in detail in Section 2.4, relies in principle on superposition. Thus, under cyclic loading, the measured CGR is the superposition of mechanical fatigue, corrosion fatigue, and SCC components. Thus, a crack is considered "transitioned" when the SCC component is non-zero, that is, the measured CGR is larger than the sum of the fatigue and corrosion fatigue components. Once the crack is transitioned to IG SCC, the specimen is set at constant load. By eliminating the mechanical fatigue and corrosion fatigue components, constant load allows for the SCC CGR to be measured directly. However, as the crack grows in an IG fracture mode, it typically follows the least resistant grain boundary path. As such, crack branching develops, and that in turn results in unbroken/uncracked ligaments. As described in the previous section, the DC potential method measures the potential drop across the unbroken ligament in the sample; hence, the ligaments formed during preferential SCC cracking confound the DC potential measurement by making the crack appear shorter than it is in reality. As a result, the crack advance measured on the fracture surface of the specimen at the end of the test is almost always longer than that measured in-situ. Therefore, a correction of the DC potential data is almost always needed after the test is completed when the DC potential data is compared to the actual crack advance measured on the fracture surface. The downside of this approach is that in the case of SCC tests conducted under multiple conditions resulting in the same fracture mode, e.g., multiple stress intensity factors or multiple test temperatures, the fracture surface cannot be used to distinguish between the various test periods. Nevertheless, the uncertainty regarding the amount of crack growth during a test period at constant load can be minimized by introducing cycling loading at the end of that test period. This cyclic loading is typically a well-known condition for which the CGR is known precisely. If ligaments form during constant load, the resulting CGR during this subsequent test period is typically higher than the known rate. This is the case for as long as ligaments are broken, then the CGR eventually settles to the known rate once that process is complete. The point at which the rate settles to the known rate is interpreted to signal the actual extent of crack advance during the previous test period at constant load. This approach results in a conservative CGR as it does not take into account the growth due to cyclic loading.

As an alternative to the two approaches described previously, some form of cycling or periodic unloading (PU) is introduced during the constant load test period with the purpose of breaking the ligaments as they form, and allow for a more realistic SCC CGR to be measured in real time. As a guideline, the cycle/periodic unloading is chosen to be gentle enough not to drive the crack by itself, but aggressive enough to be effective at breaking the ligaments. These experimental challenges have been recognized in industry publications,[15] and periodic unloading with a minimum hold time of 1 h is, in fact, recommended.[15,17] Such conditions have been used to generate a large portion of the database used for generating the industry disposition curves.[15,17] The data generated at ANL conform to these guidelines. In addition, for each test conducted at ANL, the fatigue behavior is confirmed at the beginning of the test during precracking; this way the contributions from fatigue during constant load with periodic unloading or cycling plus hold conditions are calculated with precision during each test. Nevertheless, to increase confidence in the results, the objective of each ANL test is to measure the SCC CGR under not just one, but several loading conditions.

A post-test examination of the specimen is always conducted. Typically, all specimens are examined microscopically at the fracture surface and sometimes in the cross section. For the cross section examination, the two side surfaces are ground to remove the side grooves. The cross sections are then polished and etched. They are examined by scanning electron microscopy (SEM) to verify the planarity of the crack front and to determine the extent of crack branching. Next, the specimens are fractured to expose the fracture surface obtained during the test. The fracture surface is examined by SEM to measure the crack extension and to determine the fracture mode(s). The crack length measurements obtained on the fracture surface are used to correct the data obtained in-situ by the DC potential method. As described in the previous paragraph, the DC potential method typically underestimates the full extent of the crack, particularly during intergranular cracking. Hence, during the correction stage, the DC potential data is adjusted to match the measurements obtained on the fracture surface. The known relationships between the loading conditions and the expected fracture mode are used to the extent possible to substantiate the correction approach.

2.5 Analysis of Crack Growth Rate Data

Under cyclic loading, the CGR (m/s) in the environment, $\dot{a}_{env}$, can be expressed as the superposition of the rate in air (i.e., mechanical fatigue) and the rates due to corrosion fatigue and SCC ($\dot{a}_{CF}$ and $\dot{a}_{SCC}$, respectively), given as[18,19]

$$\dot{a}_{env} = \dot{a}_{air} + \dot{a}_{CF} + \dot{a}_{SCC} \,. \tag{1}$$

The cyclic CGRs for Ni alloys and welds in air were determined from correlations developed earlier at Argonne:,[18,19]

$$\dot{a}_{air} = \left(\frac{da}{dN}\right) / t_r = \left[C \cdot (1 - 0.82 \cdot R)^{-2.2} \cdot (\Delta K)^{4.1}\right] / t_r \,, \tag{2}$$

where da/dN is the growth rate per cycle, t_r is the rise time for the loading cycle, R is the load ratio (i.e., ratio of the minimum and maximum stress intensity factors K_{min}/K_{max}), ΔK is K_{max} - K_{min} in MPa $m^{1/2}$, and the constant C depends on the material and temperature. For Alloy 600, the constant (C_{A600}) is a third-order polynomial with respect to temperature T (°C),[18,19]

$$C_{A600} = 4.835 \times 10^{-14} + (1.622 \times 10^{-17})T - (1.490 \times 10^{-18})T^2 + (4.355 \times 10^{-21})T^3 \,. \tag{3}$$

In earlier Argonne work, correlations were developed to estimate the enhancement of cyclic CGRs in LWR environments relative to the CGRs in air under the same loading conditions. In the absence of any significant contribution of SCC to growth rate, the cyclic CGRs for Alloy 600, either in the solution annealed (SA) condition or the SA plus thermally treated (TT) condition, in ≈300 ppb dissolved oxygen (DO) water at 289°C [552°F] are given by the expression[18,19]

$$\dot{a}_{env,A600} = \dot{a}_{air,A600} + 4.4 \times 10^{-7} \cdot \left(\dot{a}_{air,A600}\right)^{0.33} \,. \tag{4}$$

In low-DO environments [e.g., hydrogen water chemistry for the boiling water reactor (BWR) or PWR environment] at 320°C [608°F], some alloys show little enhancement, while others show enhancement comparable to that predicted by Eq. 4.

For the Davis-Besse nozzle #3 alloy 600 heat M3935, Eq. 4 was believed to underestimate the observed behavior; hence, a new correlation was established for this alloy:[9]

$$\dot{a}_{env,A600} = \dot{a}_{air,A600} + 6.6\times10^{-7}\cdot\left(\dot{a}_{air,A600}\right)^{0.33}. \tag{5}$$

The SCC growth rate data for Alloy 600 have been reviewed by White and Hickling (EPRI Materials Reliability Program (MRP) -55[11]) to determine the effects of critical parameters such as stress intensity factor, temperature, material heat treatment, cold work, and water chemistry on growth rates. For Alloy 600, the CGR (m/s) under SCC conditions is represented by the expression,

$$\dot{a}_{A600} = \alpha\exp\left[-\frac{Q}{R}\left(\frac{1}{T}-\frac{1}{T_{ref}}\right)\right](K-K_{th})^{\beta}, \tag{6}$$

where:

Q	=	activation energy for crack growth
	=	130 kJ/mol (31.1 kcal/mol) for Alloy 600,
R	=	universal gas constant
	=	8.314×10^{-3} kJ/mol K (1.103×10^{-3} kcal/mol·°R),
T	=	absolute operating temperature in K (or °R),
T_{ref}	=	absolute reference temperature used to normalize the CGR data
	=	598 K (325°C)[617°F],
α	=	crack growth amplitude (2.67×10^{-12} at 598K (325°C) [617°F],
K	=	crack tip stress intensity factor (MPa·m$^{1/2}$),
K_{th}	=	crack tip stress intensity factor threshold (9 MPa·m$^{1/2}$), and
β	=	exponent 1.16.

Figure 11 illustrates how the superposition concept introduced earlier (Eq. 1) is used to analyze the cyclic CGR data generated in a PWSCC test. As described in the previous section, a typical test at ANL consists of three stages: in-situ precracking, transitioning to SCC, and the SCC growth stage. The precracking stage is dominated by mechanical fatigue, hence, in this stage of the test where CGR rates are typically larger than 10^{-9} m/s, the expectation is that the measured CGRs are close to those expected under the same loading conditions in air, $\dot{a}_{air}$, which is calculated using Eqs. 2 and 3. During the transitioning to SCC stage, cyclic loading is continued under loading conditions expected to induce environmental enhancement. The environmental enhancement is typically observed under loading conditions that lead to CGRs between 10^{-11} and 10^{-9} m/s in air, and the effect of the additional corrosion fatigue component is labeled $\dot{a}_{air} + \dot{a}_{CF}$ in the figure. For typical Alloy 600, the corrosion fatigue behavior is expressed by Eq. 4. Finally, if an SCC component is also present, the specimen response is expected to follow the curve labeled $\dot{a}_{air} + \dot{a}_{CF} + \dot{a}_{SCC}$ in the figure. For the purpose of the illustration shown in Fig. 11, the $\dot{a}_{SCC}$ component was calculated using Eq. 6, and represents the SCC CGR of an alloy with a cracking susceptibility ranking at the 75th percentile.

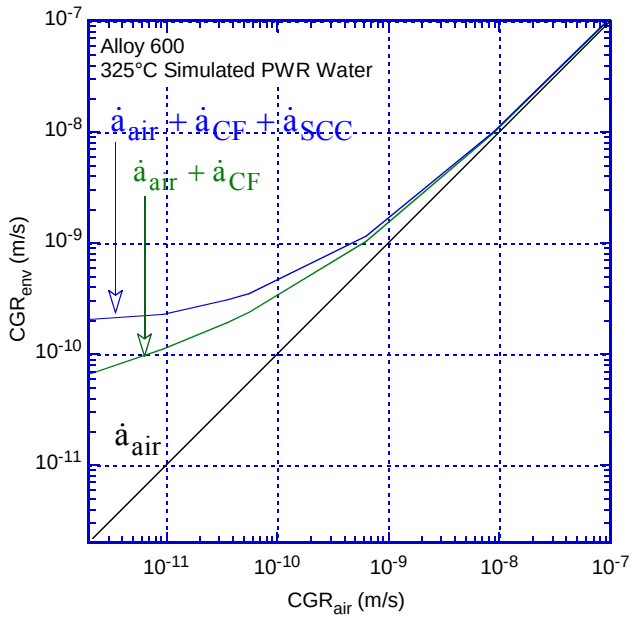

Figure. 11
Cyclic CGRs for typical Alloy 600 tested in a PWR environment. Corrosion fatigue (Eq. 4, green) and SCC (Eq. 6, blue) curves are included.

3 Microstructural Characterization

The Alloy 600 heat number M7929 CRDM nozzle #4 from the replacement head was subjected to a metallographic analysis similar to the one used previously for the nozzle #3 alloy. The focus was on the grain boundary microstructure, with special attention paid to grain boundary carbides. Grain boundary carbides have been found to have a profound impact on the SCC behavior of Alloy 600, affecting both crack initiation and propagation. Several early studies[20-21] reported correlations between high grain boundary carbide coverage and increased cracking resistance, and subsequent work[22-23] has isolated and established the beneficial effect of carbides on SCC behavior.

Figure 12 shows scanning electron microscopy (SEM) images of the microstructure of the replacement alloy. While some grain size variation can be observed in Fig. 12a, Fig. 12b shows what appear to be carbide-free grain boundaries. The grain size variation was explored further, but the only correlation was found with the distance to the inside diameter (ID) and outside diameter (OD) of the nozzle. Figure 13 shows the average grain diameter as a function of the distance to the ID. The average grain diameter was found to decrease slightly vs. distance from the ID.

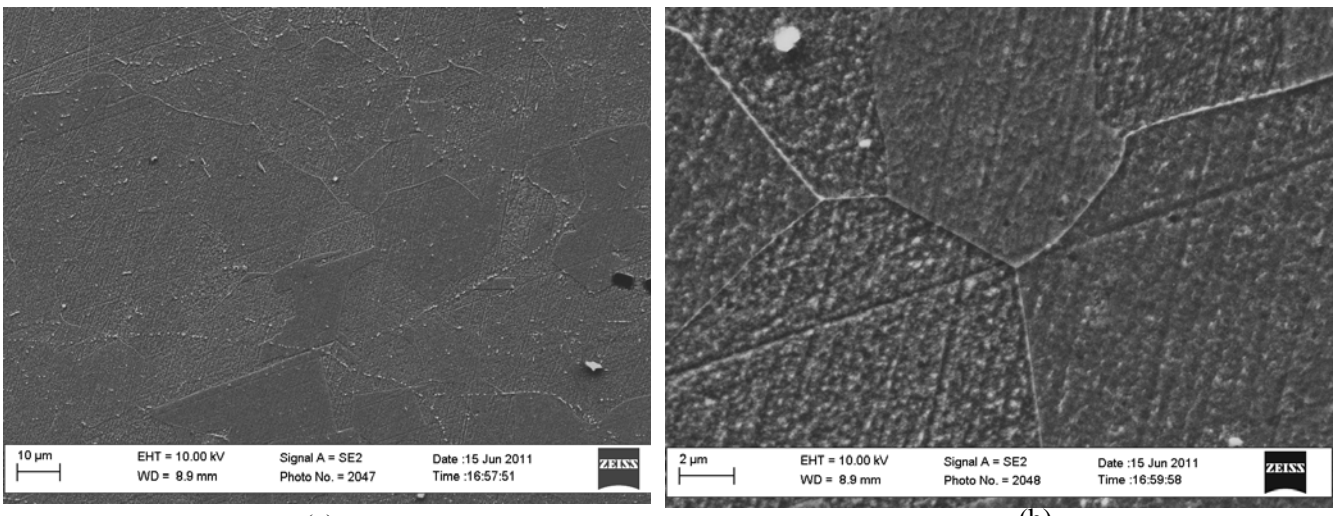

(a) (b)

Figure 12. Microstructure of the Davis-Besse replacement alloy 600 heat number M7929 CRDM nozzle #4: (a) general view and (b) carbide-free grain boundaries.

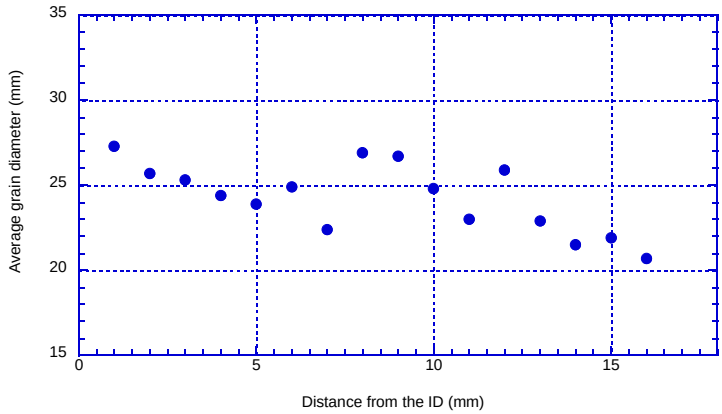

Figure 13.
Average grain diameter vs. the distance to the ID of the Davis-Besse replacement alloy 600 heat number M7929 CRDM nozzle #4.

The carbide distribution was also explored further. Figure 14 shows two images of the microstructure. Figure 14a shows the grain boundary network. Several TiN particles are indicated by arrows. Such particles have also been observed[9] in the nozzle #3 material (Alloy 600 heat M3935). Figure 14b is a dark field image of essentially the same area. This image also makes the carbides visible, and these also seem to be arranged in a network. However, there seems to very little correlation between the grain boundary network and the carbide network. Ideally, for optimum PWSCC resistance, the carbides should have been located at the grain boundaries. The desired microstructure is typically obtained by a heat treatment that puts the carbon in solution so that carbides precipitate at grain boundaries during cooling. The processing history of Alloy 600 heat M7929 alloy is unknown, however, the only known requirement for this material was for the final mill annealing temperature to be maintained above 871 (1600ºF) for a minimum of 10 minutes.[24] The microstructure shown in Fig. 14 suggests that the temperature (or the time at this temperature) were insufficient to solutionize the carbides.

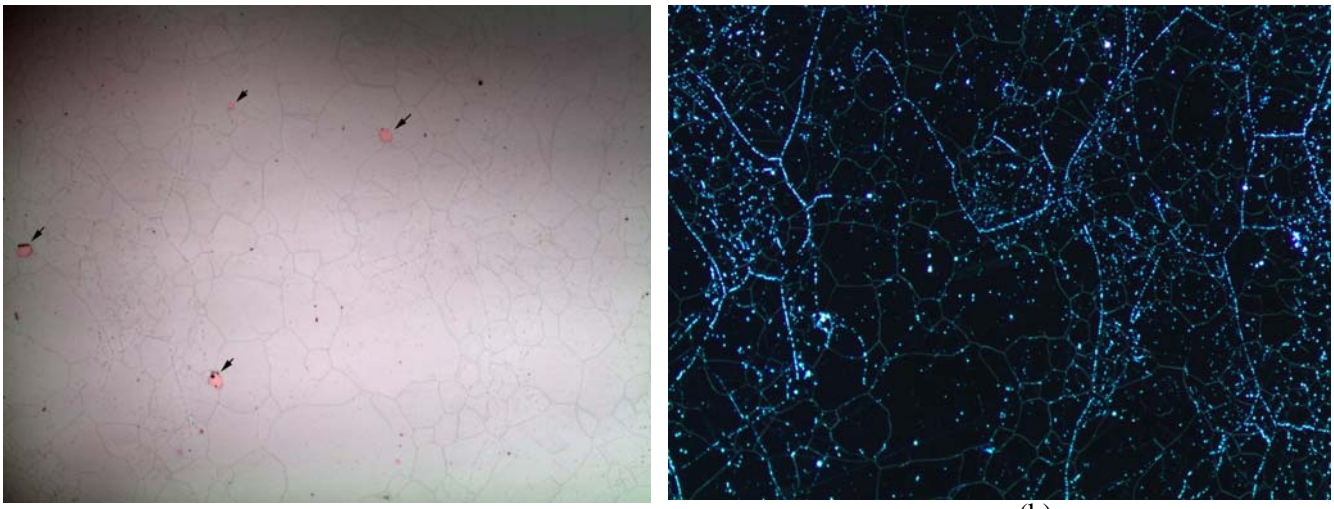

(a) (b)

Figure 14. Microstructure of the Davis-Besse replacement alloy 600 heat number M7929 CRDM nozzle #4: (a) grain boundary network and (b) grain boundary and carbide networks.

Figure 15 shows additional images obtained on the same Alloy 600 heat M7929 microstructure. These images were obtained at different magnifications and show that the grain boundary and carbide networks are indeed different. In Figs. 15 c, d, the red arrows indicate grain boundaries and blue arrows indicate carbides. While in a few isolated cases (Fig. 15c) some carbides appear to be on grain boundaries, the vast majority of carbides decorate what seem to be the ghost boundaries of a prior network. By contrast (Fig.16), the nozzle #3 alloy appears to have an adequate grain boundary carbide decoration. In short, the microstructure of nozzle #3 (Alloy 600 heat M3935) appears to be more consistent with what would be expected for an Alloy 600 thermally treated (TT) microstructure compared to the microstructure of the replacement alloy (Alloy 600 heat M7929). The possible implication of this microstructural difference with respect to IG SCC susceptibility will be discussed further in Section 5.3.

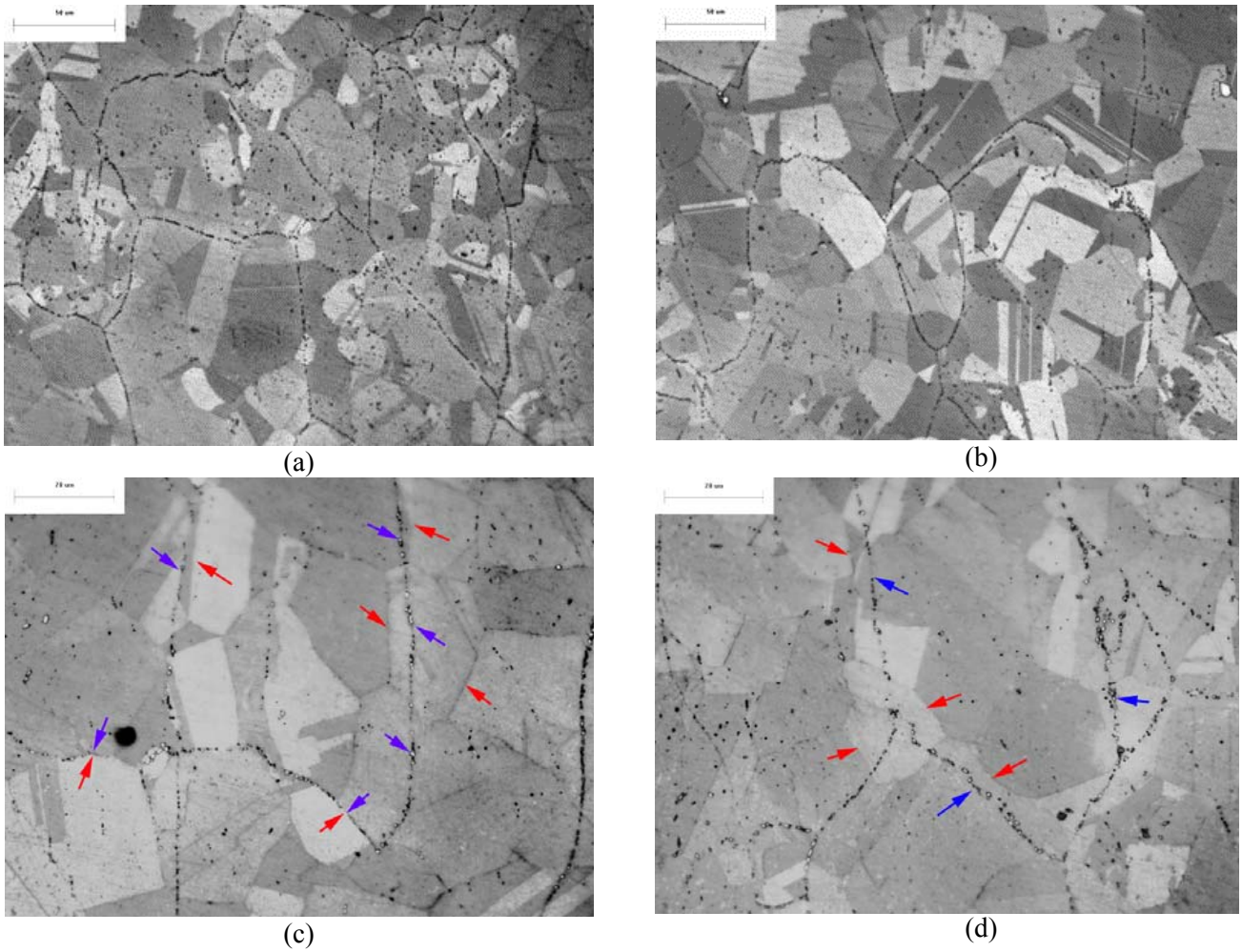

Figure 15. Microstructure of the Davis-Besse nozzle #4 replacement material (Alloy 600 heat M7929). Scale bar is 50 µm [0.002 in] for top row and 20 µm [0.0008 in] for bottom row. Red arrows indicate grain boundaries and blue arrows indicate carbides.

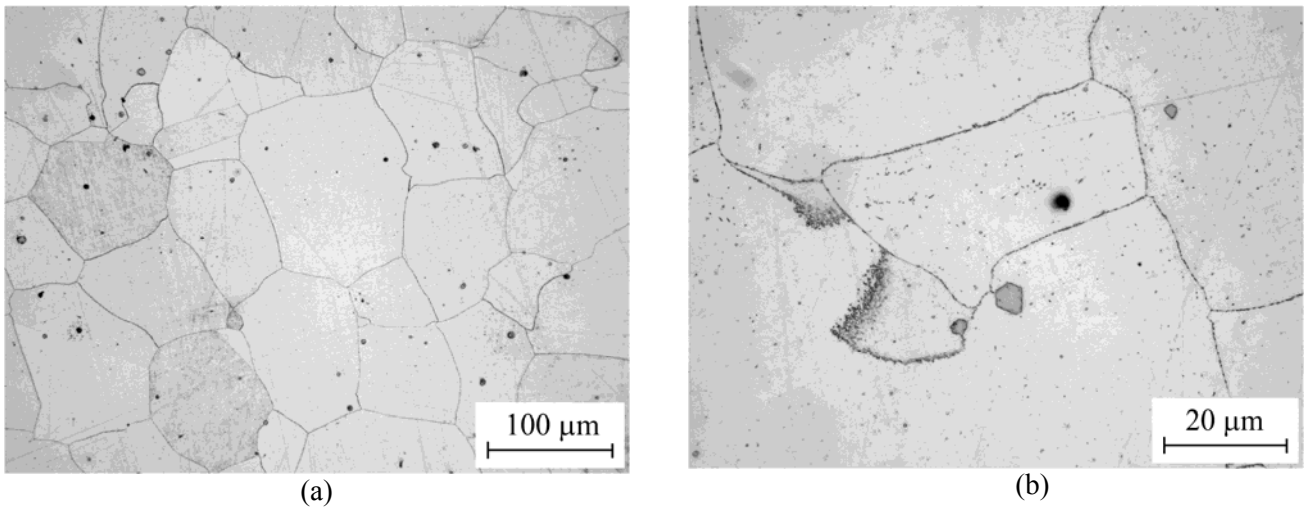

Figure 16. Microstructure of the Davis-Besse nozzle #3 material (Alloy 600 heat M3935) at two magnifications.

4. Results

This section presents the results of the SCC tests in chronological order. The test on Specimen DB-5 was initiated first, followed two months later by the test on Specimen DB-4. The test on Specimen DB-3 was initiated after both tests on specimens DB-4 and DB-5 were complete. This sequence allowed for the specific objectives for each test to be adjusted as needed.

4.1 Specimen DB-5

Specimen DB-5 was the first specimen to be tested. The initial objectives for the test were to obtain SCC CGRs at two stress intensity factors. Later on, several test periods at different temperatures were added in order to also determine the activation energy for SCC growth. The testing conditions for this specimen are given in Table 1, and the changes in crack length and K_{max} with time are shown in Fig. 17. The total extent of the crack measured on the fracture surface was 22% higher than the DC potential measurement. Given that the resulting fracture mode was predominantly IG for the entire test, the correction was applied uniformly across the data set. The data presented in the table and in the figure already reflect the 22% correction factor. In some instances, additional interpretation of the data was needed, and these cases will be discussed later in this section.

The test was initiated in simulated primary water at 325°C [617°F] with in-situ precracking (Pre a – Pre g), followed by transitioning (test periods 1-4). The goal of the first part (test periods 5-11) was to measure the SCC CGRs at relatively low stress intensity factors, 23.1-23.7 MPa $m^{1/2}$ [21.0-21.6 ksi $in^{1/2}$]. Next, in test periods 12-22, the SCC CGRs were measured at higher stress intensity factors, 27.5-29.0 MPa $m^{1/2}$ [25.0-26.4 ksi $in^{1/2}$]. In test periods 23-27, the test temperature was increased to 350°C [662°F] to evaluate the SCC CGRs at this higher temperature and to make a determination of the activation energy for SCC growth in this alloy. Next, the system was returned to the initial testing temperature (325°C [617°F]) in periods 28 and 29 to re-confirm the initial SCC CGRs. At the completion of the test periods in primary water, the system was brought to room temperature, drained of water, and two final confirmatory fatigue test periods were conducted in air. Additional details on all of these testing periods will be provided next.

Table 1. Crack growth data for specimen DB-5 (DB600-CL-2) of Alloy 600 in PWR water.[a]

Test Period	Test Time, h	Temp., °C	Load Ratio R	Rise Time, s	Down Time, s	Hold Time, s	K_{max}, MPa·m$^{1/2}$	ΔK, MPa·m$^{1/2}$	CGR_{env}, m/s	Estimated CGR_{air}, m/s	Crack Length, mm
Pre a	107	326.2	0.32	1	1		20.9	14.2	1.00E-08	9.78E-09	12.122
Pre b	122	325.6	0.31	100	100		20.9	14.4	6.35E-10	1.01E-10	12.160
Pre c	127	325.8	0.32	1	1		21.3	14.5	1.47E-08	1.04E-08	12.272
Pre d	130	326.0	0.32	2	2		21.5	14.6	1.12E-08	5.47E-09	12.348
Pre e	146	325.9	0.32	50	50		21.7	14.7	1.76E-09	2.26E-10	12.403
Pre f	151	326.0	0.32	1	1		22.3	15.2	2.17E-08	1.27E-08	12.596
Pre g	171	326.1	0.32	50	50		22.5	15.3	2.41E-09	2.66E-10	12.678
1	176	325.9	0.49	50	12		22.5	11.4	1.30E-09	1.27E-10	12.701
2	201	326.0	0.49	300	12		22.6	11.5	4.65E-10	2.19E-11	12.739
3	243	326.0	0.49	600	12		22.8	11.6	3.67E-10	1.12E-11	12.793
4	268	325.9	0.49	1000	12		23.0	11.7	2.93E-10	7.03E-12	12.816
5	340	326.3	1.00	0	0		23.1	0.0	4.50E-11	-	12.828
6	388	326.7	0.50	600	12		23.3	11.6	3.58E-10	1.18E-11	12.880
7	509	326.2	0.50	600	12	7200	23.3	11.7	6.08E-11	9.11E-13	12.913
8	774	326.5	1.00	0	0		23.4	0.0	1.10E-11	-	12.917
9	819	326.5	0.50	600	12		23.6	11.8	3.25E-10	1.23E-11	12.967
10	939	326.6	0.50	600	12	7200	23.7	11.8	6.42E-11	9.72E-13	13.000
11	1,069	326.0	0.50	12	12	7200	23.7	11.9	5.66E-11	1.05E-12	13.024
12	1,075	324.7	0.50	50	12		26.9	13.5	3.44E-09	2.53E-10	13.073
13	1,093	324.7	0.50	600	12		27.1	13.6	6.06E-10	2.17E-11	13.109
14	1,123	324.6	0.50	600	12	7200	27.2	13.6	1.83E-10	1.69E-12	13.134
15	1,452	324.6	1.00	0	0		27.5	0.0	1.33E-10	-	13.174
16	1,499	324.5	0.50	600	12		27.8	13.9	6.14E-10	2.40E-11	13.328
17	1,623	324.7	0.50	600	12	7200	28.2	14.1	1.60E-10	1.96E-12	13.403
18	1,794	324.4	0.50	12	12	7200	28.5	14.2	1.35E-10	2.21E-12	13.490
19	1,868	324.9	1.00	0	0		28.6	0.0	6.70E-11	-	13.499
20	2,394	325.3	1.00	0	0		29.0	0.0	6.49E-11	-	13.561
21	2,427	325.4	0.50	600	12		27.2	13.6	3.97E-10	2.21E-11	13.648
22	2,612	325.2	0.50	12	12	7,200	27.3	13.7	4.89E-11	1.86E-12	13.684
23	2,664	349.9	0.50	12	12	7,200	27.8	13.9	1.20E-10	2.36E-12	13.705
24	2,686	349.5	0.50	600	12		27.6	13.8	5.04E-10	2.74E-11	13.715
25	2,784	350.2	0.50	12	12	7,200	28.0	14.0	8.57E-11	2.44E-12	13.778
26	2,812	349.9	0.50	600	12		28.4	14.2	5.19E-10	3.07E-11	13.840
27	2,925	349.7	1.00	0	0		28.4	0.0	4.68E-11	-	13.854
28	3,102	324.5	0.54	12	12	7200	28.3	14.1	9.75E-11	2.14E-12	13.899
29	3,268	324.6	1.00	0	0		28.4	0.0	7.02E-11	-	13.939
30	3,297	21.7	0.30	2	2		29.5	20.7	1.08E-08	1.18E-08	14.217
31	3,299	21.7	0.30	1	1		29.8	20.8	1.41E-08	2.44E-08	14.269

[a]Simulated PWR water with 2 ppm Li, 1100 ppm B, and 2 ppm. DO<10 ppb. Conductivity is 21±3 μS/cm, and pH is 6.4.

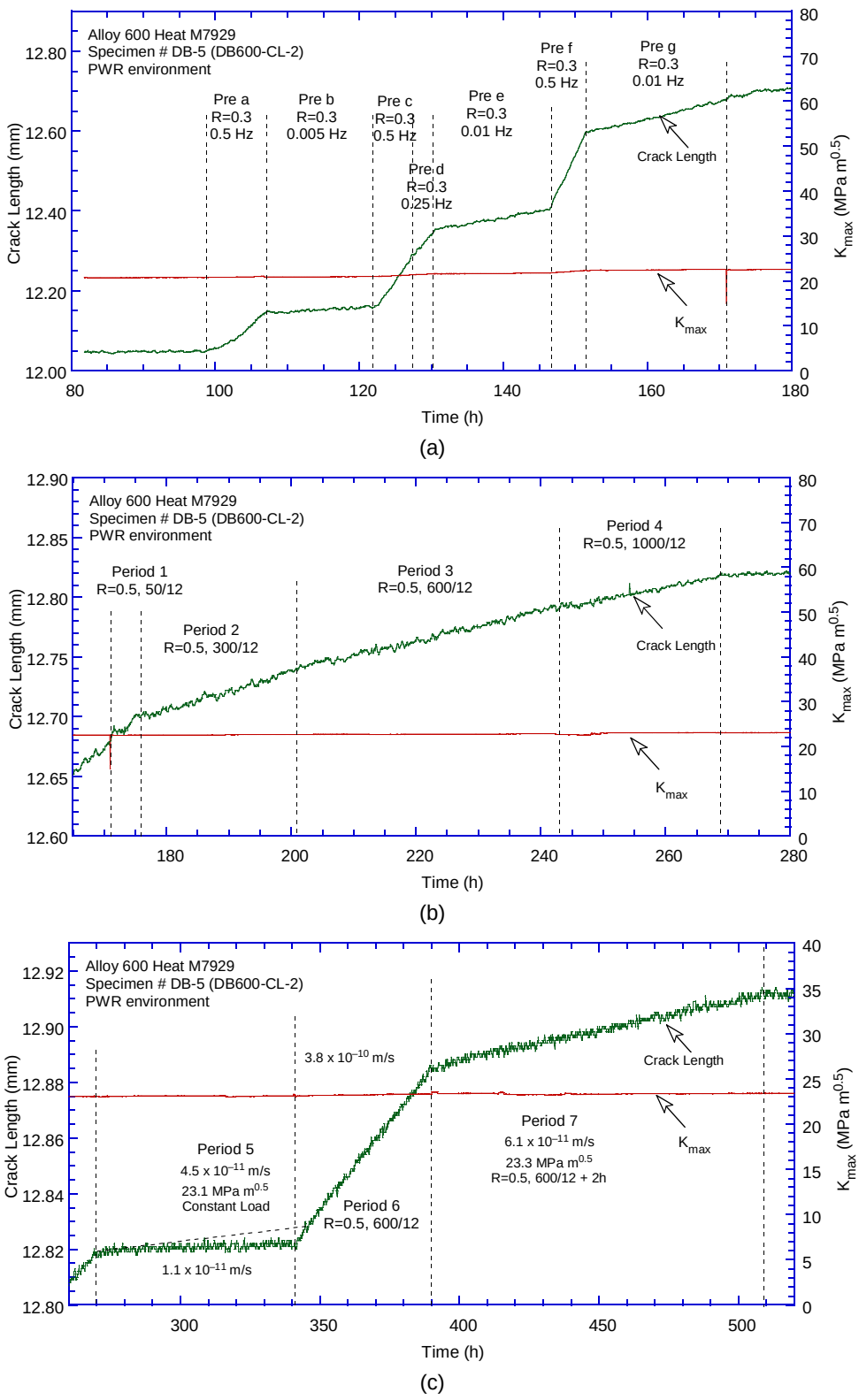

Figure 17. Crack length vs. time for Alloy 600 heat M7929 specimen DB-5 in simulated PWR environment during test periods: (a) precracking, (b) 1-4, (c) 5-7, (d) 8, (e) 9 and 10, (f) 11 and 12, (g) 13-16, (h) 17-19, (i) 20 and 21, (j) 22, (k) 23-27, (l) 28, (m) 29, and (n) 30 and 31 .

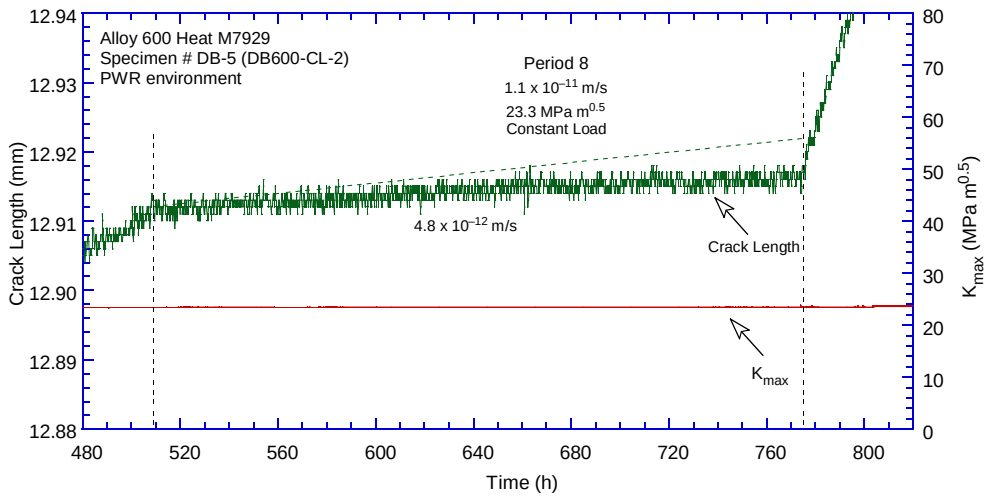

(d)

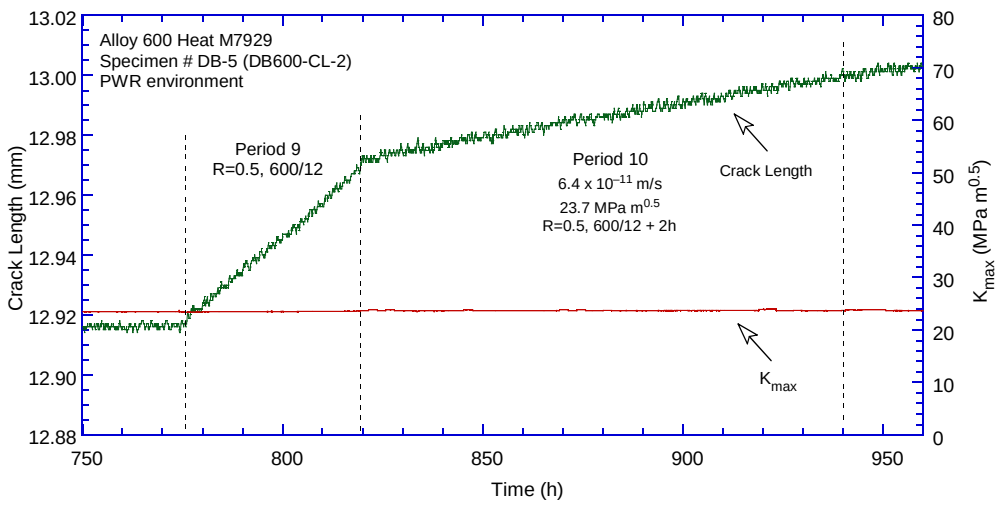

(e)

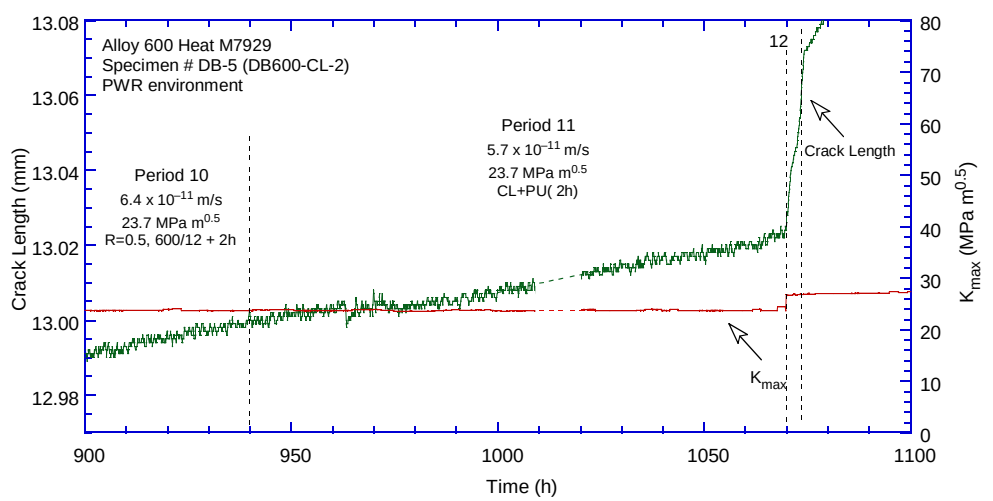

(f)

Figure 17. (cont.)

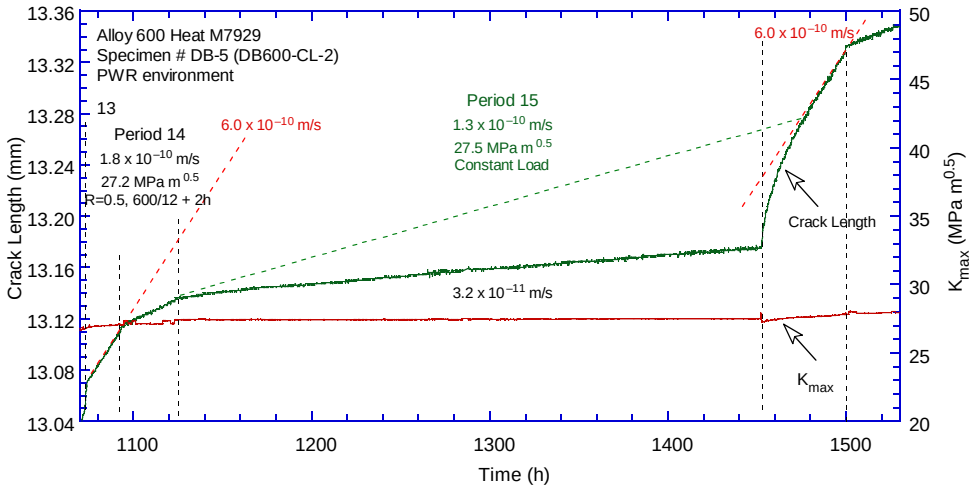

(g)

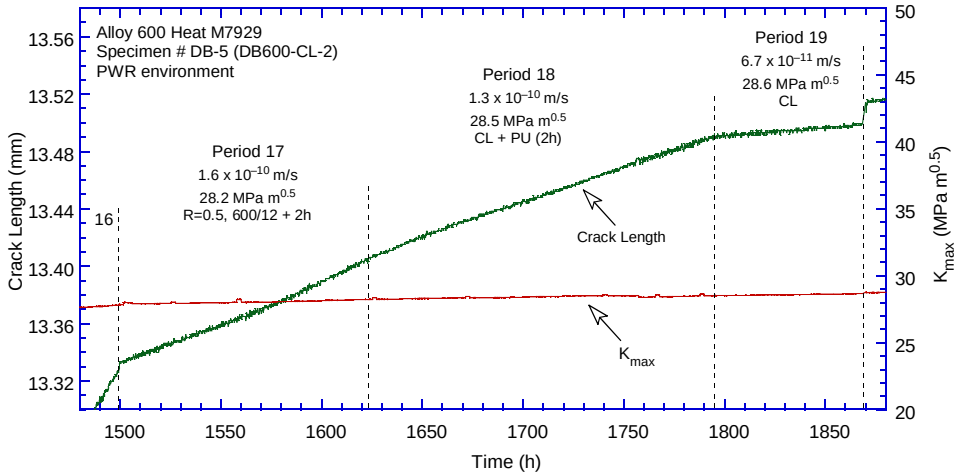

(h)

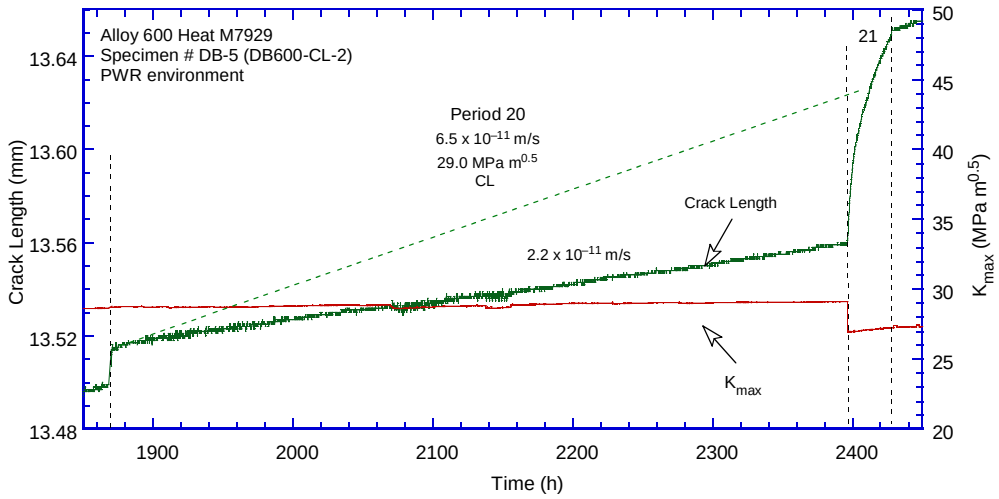

(i)

Figure 17. (cont.)

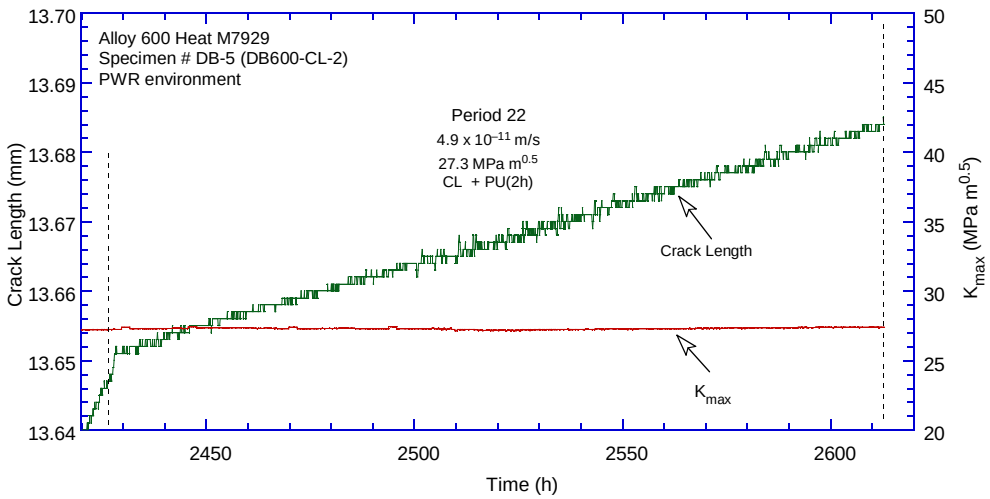

(j)

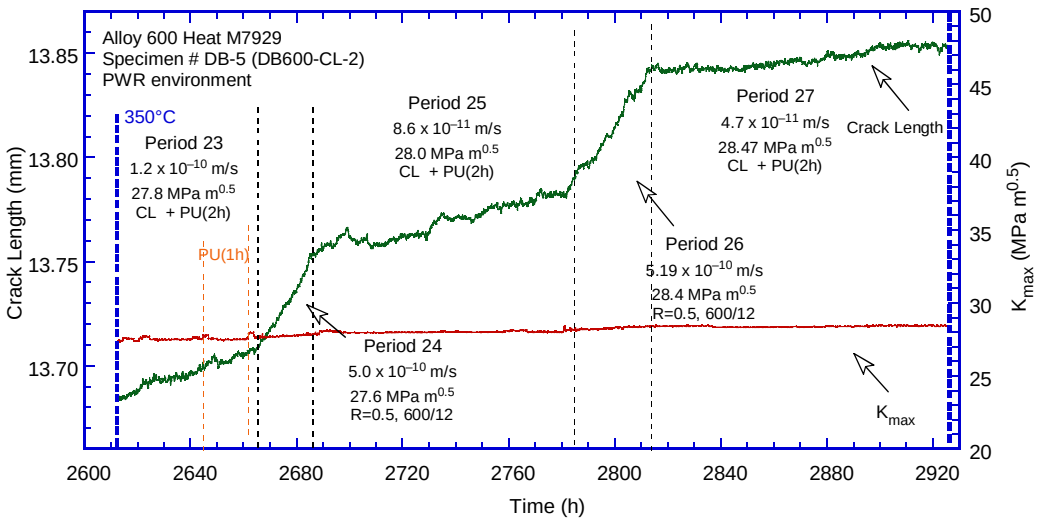

(k)

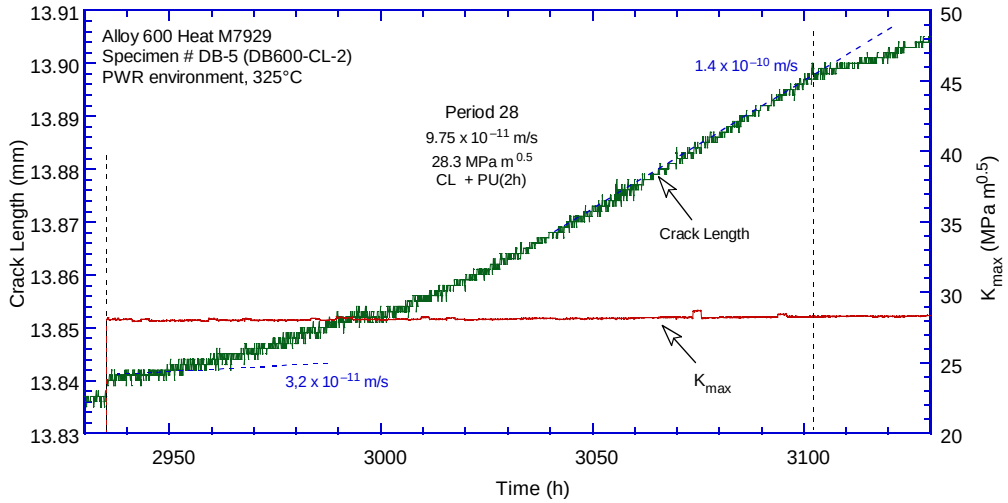

(l)

Figure 17. (cont.)

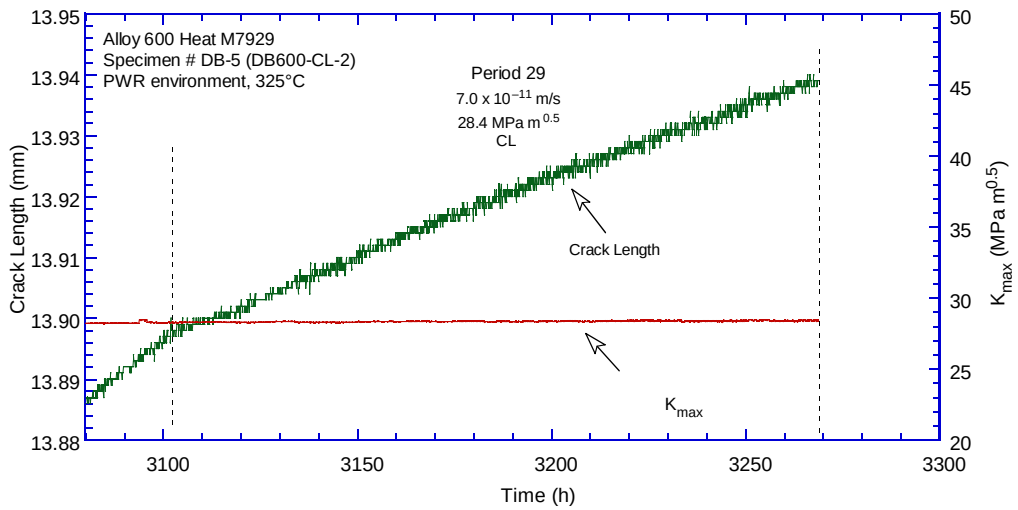

(m)

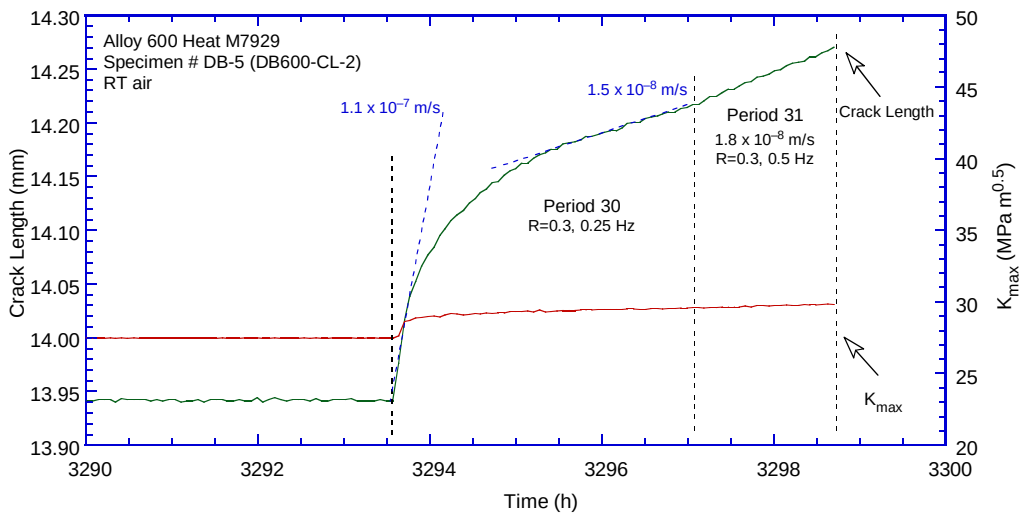

(n)

Figure 17. (cont.)

Following precracking in simulated primary water and transitioning in test periods 1-4, the specimen was set a constant load in period 5. Based on the analysis of the cyclic rates, the expectation was that the SCC CGR would be somewhat larger than was being measured. Hence, cycling was restarted in period 6. Upon the re-introduction of gentle cycling in period 6, some rapid growth at 4.9 x 10^{-10} m/s was observed before the CGR settled to 3.6 x 10^{-10} m/s, a rate consistent with that observed previously in test period 3 (Table 1). The crack extent at which the fatigue CGR stabilizes is indicated by the blue arrow in the Fig. 18. The initial rapid rate suggests that some ligaments were broken, and that the actual extent of the crack was larger. If the additional crack extent is taken into account, a conservative estimate for the SCC CGR for period 5 is ~ 4.5 x 10^{-11} m/s. The new, estimated rate for test period 5 is illustrated with a dotted line in Fig. 18. In the next test period (7), a 2-h hold was introduced determine the SCC CGR component by superposition. The SCC CGR component for test period 7 was calculated to be ~ 5.6 x 10^{-11} m/s, in good agreement with the corrected SCC CGR for period 5.

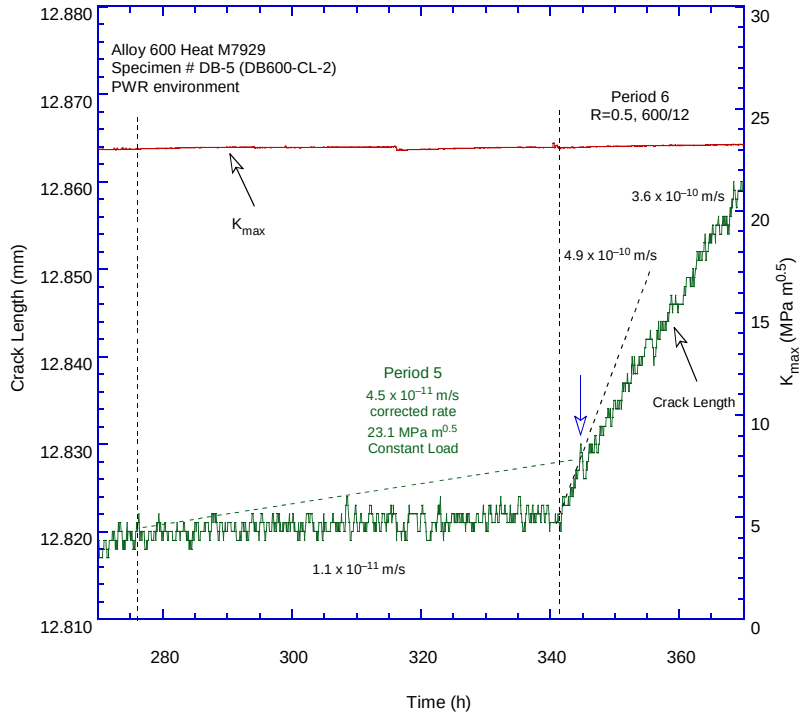

Figure 18.

Crack behavior after gentle cycling is introduced in test period 6.

The second constant load period of this test, period 8, again yielded a relatively low SCC CGR. Hence, gentle cycling conditions were restarted in test period 9. Upon the re-introduction of gentle cycling in period 9, some rapid growth at 6.3 x 10^{-10} m/s was observed before the CGR settled to 3.3 x 10^{-10} m/s (consistent with the rates measured in test periods 3 and 6), as shown in Fig. 19. Again, the behavior suggests that a ligament had formed, which, when taken into account, resulted in a corrected SCC CGR of ~1.1 x 10^{-11} m/s for test period 8. The new estimated rate for test period 8 is shown with a dotted line in Fig. 17d. Next, a 2-h hold was introduced in period 10 to determine the SCC CGR component by superposition. The SCC CGR component for this test period was calculated to be ~6.4 x 10^{-11} m/s.

The specimen was set at constant load with periodic unloading (2-h hold) in test period 11. During test period 11, approximately 10h worth of data was lost between approximately 1010h-1020h (Fig. 17f) due to a computer malfunction. Upon restarting the data acquisition, growth continued at the same rate. The resulting rate for test period 11 was 5.7 x 10^{-11} m/s, in agreement with the rates for periods 5 and 8 after correcting for the presence of ligaments. This test period concluded the evaluation of SCC CGRs at low stress intensity factors. The SCC CGR rates determined thus far put the susceptibility of this alloy at the 75th percentile EPRI MRP-55 curve.[11] Next, the specimen was tested at moderate stress intensity factors.

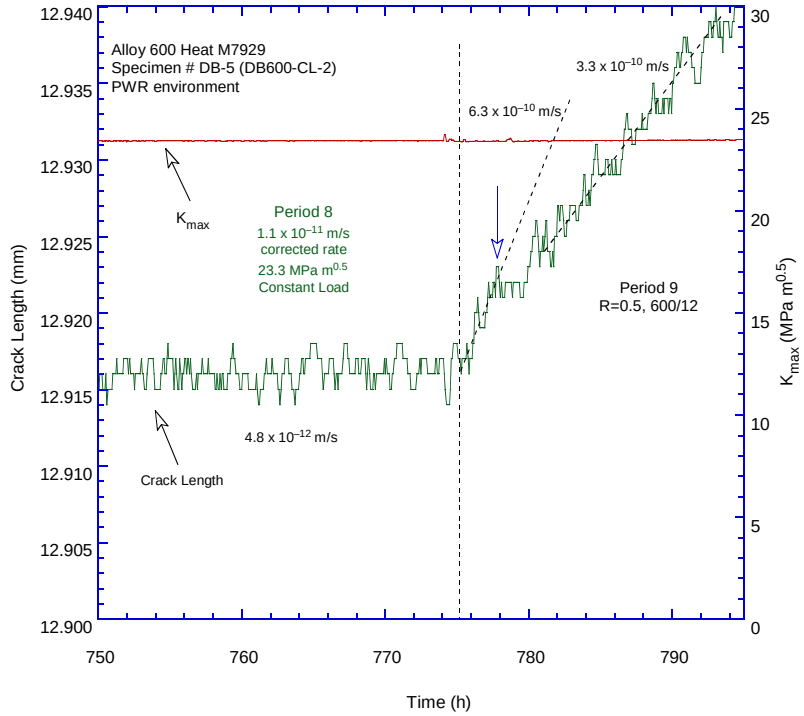

Figure 19.

Crack behavior after gentle cycling is introduced in test period 9.

The specimen was loaded to a higher stress intensity factor (≈ 27 MPa $m^{1/2}$ [24.5 ksi $in^{1/2}$], and two known cyclic conditions were reproduced in test periods 12 and 13. A 2-h hold was introduced in period 14 to assess the SCC CGR component. Growth was rapid, and the calculated SCC CGR component was 1.7 x 10^{-10} m/s. An attempt was made to confirm this rate at constant load in period 15.

The SCC CGR is period 15 was initially ≈5.0 x 10^{-11} m/s, then decreased to an average of 3.2 x 10^{-11} m/s. It was again suspected that ligaments were forming, in which case a large "jump" was expected when cyclic loading was resumed at the end of period 15. After period 15, cyclic loading similar to that of period 13 (Table 1) was introduced in period 16. The initial rate of 1 x 10^{-9} m/s was well above the known rate for this loading condition, consistent with the breaking-of-ligaments scenario that had been anticipated, Fig. 20. The CGR only settled at the known rate of 6.0 x 10^{-10} m/s after the crack passed 13.270 mm (see blue arrow in Fig. 20). When this additional amount of growth was taken into account, the SCC CGR for this period was conservatively estimated to be 1.3 x 10^{-10} m/s, consistent with the SCC CGR measured in test period 14.

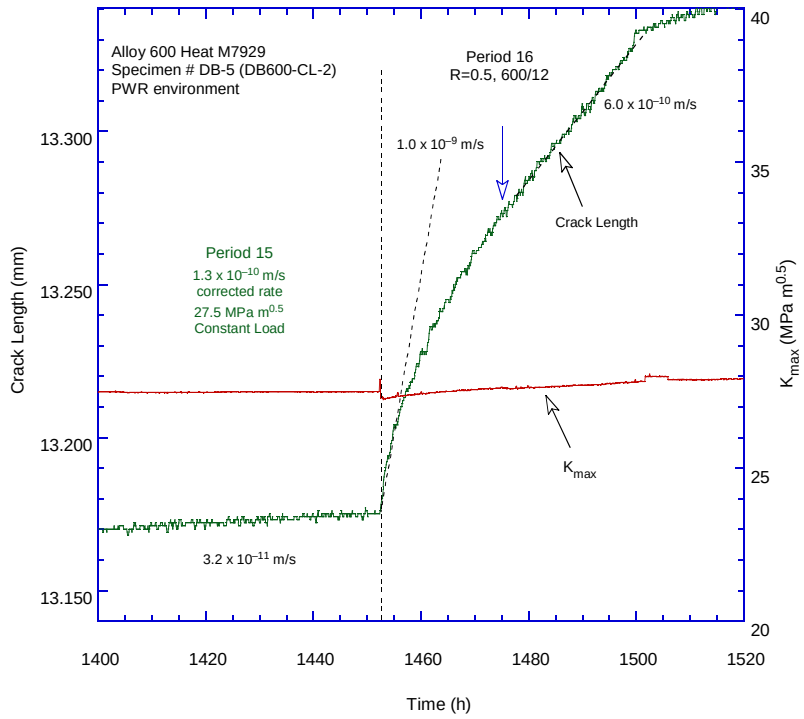

Figure 20.

Crack behavior after gentle cycling is introduced in test period 16.

Next, for further confirmation, a 2-h hold was introduced in test period 17, and the SCC CGR component was again calculated to be 1.6 x 10^{-10} m/s. Furthermore, when constant load with periodic unloading was introduced in period 18, the SCC CGR was measured to be 1.3 x 10^{-10} m/s. Constant load was again introduced in periods 19 and 20. In period 20, the SCC CGR measured by the DC potential method was 2.2 x 10^{-11} m/s. Cyclic loading was introduced in period 21, and the initial rate was, as before, well above the known rate for this loading condition, Fig. 21. The cyclic CGR eventually settled at 4.0 x 10^{-10} m/s after the crack passed the 13.630 mm mark (see the blue arrow in Fig. 21). When the additional growth was taken into account, the SCC CGR for test period 20 was found to be 6.5 x 10^{-11} m/s. The subsequent test period 22 at constant load with periodic unloading confirmed this rate. These latter rates are approximately a factor two less than the previous rates measured at similar stress intensity factors in test periods 15, 17 and 18, and are perhaps due to a more resistant microstructure. As such, the rate measured in period 22 was used as a baseline for the SCC CGR at 325ºC [617°F] for the temperature-dependence part of the test.

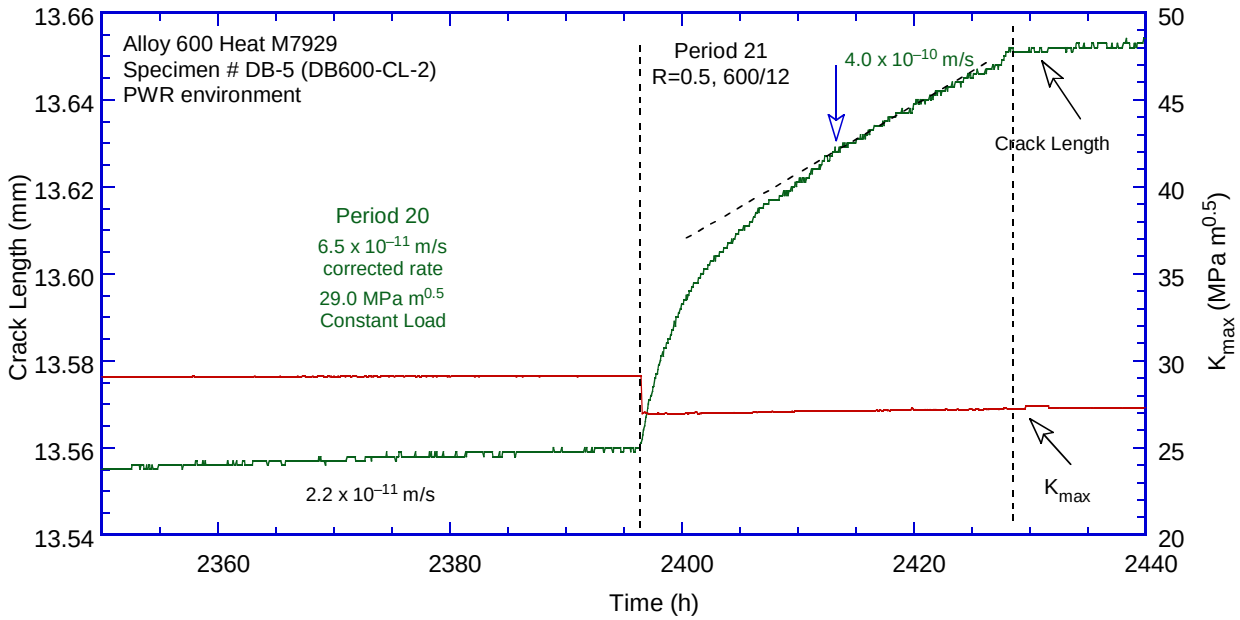

Figure 21. Crack behavior after gentle cycling introduced in test period 21.

Next, the temperature was increased to 350°C [662°F], and the dissolved hydrogen concentration in the water was increased to 45 cc/kg to maintain the same potential difference to the Ni/NiO line as the 325°C test condition. After the system was left to stabilize at the new test conditions of pressure and temperature, the DC potential was re-initialized.

Figure 17k shows the crack behavior at 350°C [662°F]. Growth in period 23 at constant load with periodic unloading (2 h) was initially relatively high (≈2.2 x 10^{-10} m/s), then the rate apparently began to diminish. Increasing the unloading rate to 1-h test period (between the two dotted orange lines in Fig. 17 k) did not change the crack growth rate. This lack of effect was not surprising, though, given that the mechanical contribution in this case is about 200 times less than the measured SCC CGR. While a more aggressive loading regimen would be appropriate in this situation, this change in test condition would fall outside of the criteria defined in MRP-55 criteria.[11] Subsequent cyclic loading in period 24 produced no CGR jump, hence, the average rate measured in period 23 was 1.2 x 10^{-10} m/s. Growth under cyclic loading in period 24 was well-behaved, and the environmental enhancement was consistent with previous periods. The specimen was set at constant load with periodic unloading (2 h) again in period 25. The CGR behavior was similar to that observed in period 23. The initial growth was fairly high (≈2.3 x 10^{-10} m/s), then settled to an average of 1.2 x 10^{-10} m/s. Cyclic loading was reintroduced in period 26, and, on average, growth was similar to that measured in period 24. The specimen was set at constant load in period 27, but the crack growth appeared to stall.

The system was returned to the initial testing conditions (325°C [617°F]) in period 28 (Fig. 17l) to reconfirm the base rate measured in period 22. The measured SCC rate was initially as expected (≈3.2 x 10^{-11} m/s), the began to increase and it eventually reached ≈1.4 x 10^{-10} m/s The latter CGR for test period 28 is clearly inconsistent with the rate measured in period 22, and is perhaps due to a more susceptible microstructure. Next, the specimen was set at constant load in period 29, and the measured rate was approximately 7.0 x 10^{-11} m/s. The specimen was not cycled at the end of the test period; the presumed ligaments were instead broken by cycling at room temperature. As a result, the ligaments

would be easily identified on the fracture surface by the difference in color between the surfaces tested in water and those tested in air.

For the final periods of the test, the system was brought to room temperature, drained of water, and two confirmatory test periods (30 and 31, Fig. 17n) were conducted in air with the purpose of exposing the ligaments. The initial CGR in period 30 was very high, approximately a factor 10 larger than expected—consistent with breaking of ligaments. Then, the rate settled close to the expected value, suggesting that the crack front had straightened. This known fatigue behavior was re-confirmed in test period 31, where the CGR was also close to the expected value.

After the test, the specimen was examined microscopically in cross section (CS) and at the fracture surface. Figures 22 and 23 show both sides of the specimen – designated CS1 and CS2 - after the side grooves were removed to expose the crack path. To provide greater detail, these SEM images are shown in two halves for each side of the specimen. Overall, the crack appears IG and extremely narrow. In addition, the IG fracture mode appears to start right from the notch, Fig. 24. It can easily be understood how such a narrow crack front can confound the DC potential measurements by shorting the two surfaces. There is also evidence of crack branching, but, for the most part, that was apparently kept under control by the loading schemes used. In fact, the cyclic rates for this test were highly reproducible. Nevertheless, there is strong evidence of crack branching toward the end of the test, which probably occurred during the test periods at 350°C. In these test periods, the cyclic schemes allowed by the EPRI MRP-55 criteria[11] are perhaps too gentle, and the crack is allowed to branch freely. Additional detail is provided in Fig. 25 (location 1 in Fig. 22b), where crack branching is so extensive that the various cracked grain boundaries do not appear to be connected.

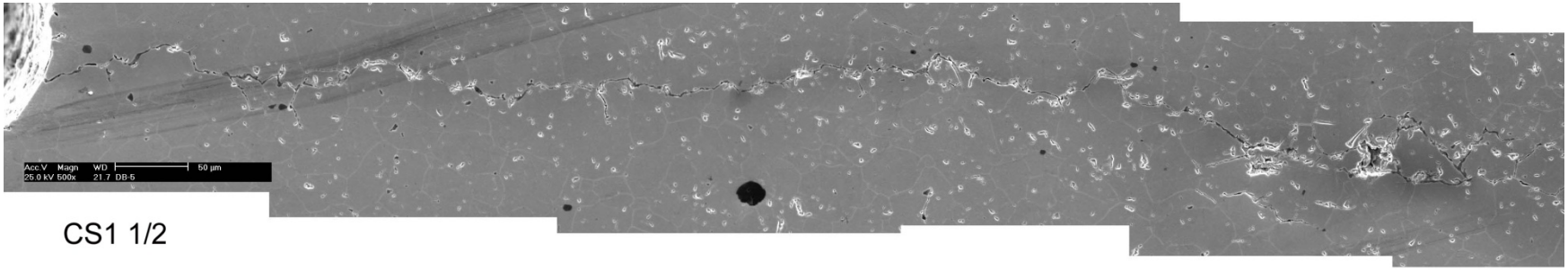

(a)

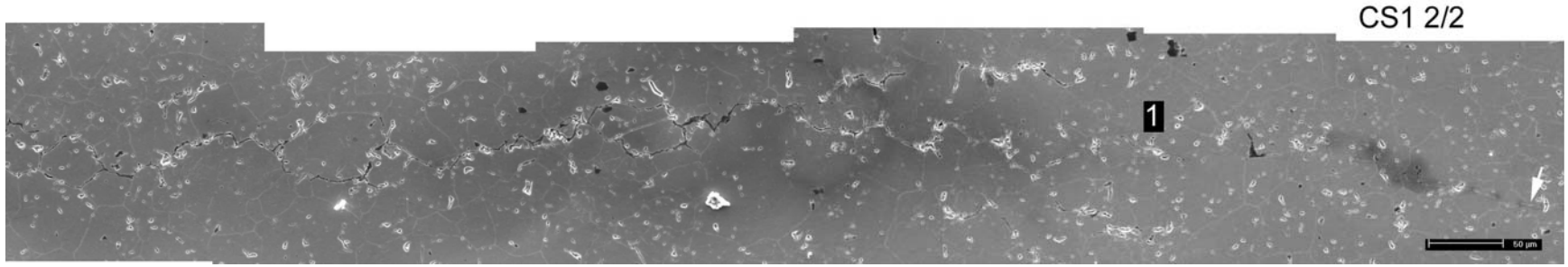

(b)

Figure 22. Cross section of specimen DB-5, first side CS1: (a) first half and (b) second half of the first cross section. Crack advance is from left to right. The arrow marks the end on the crack.

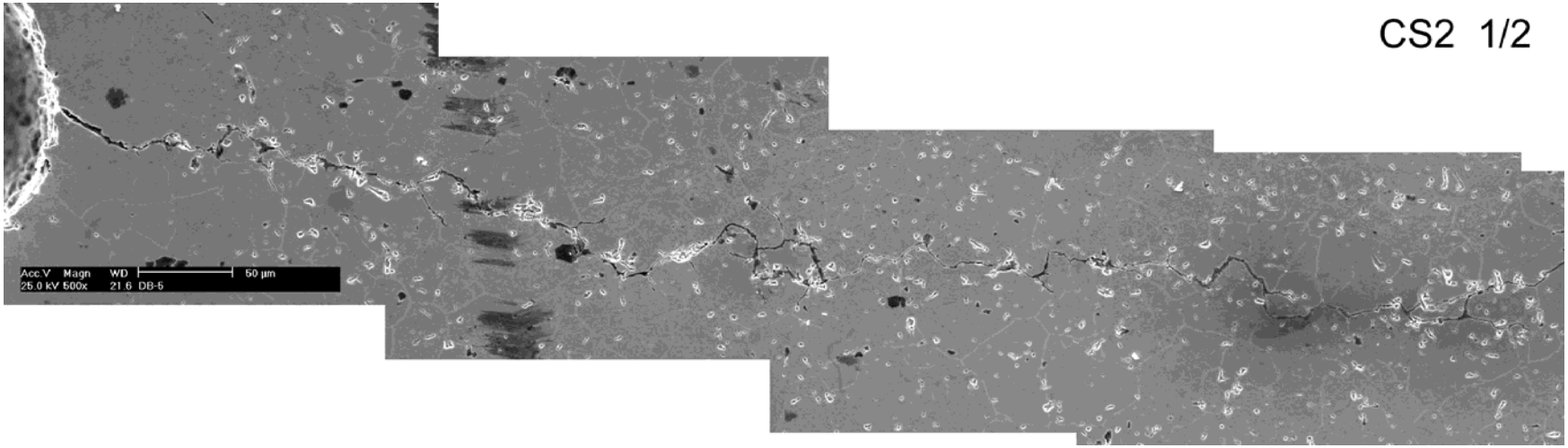

(a)

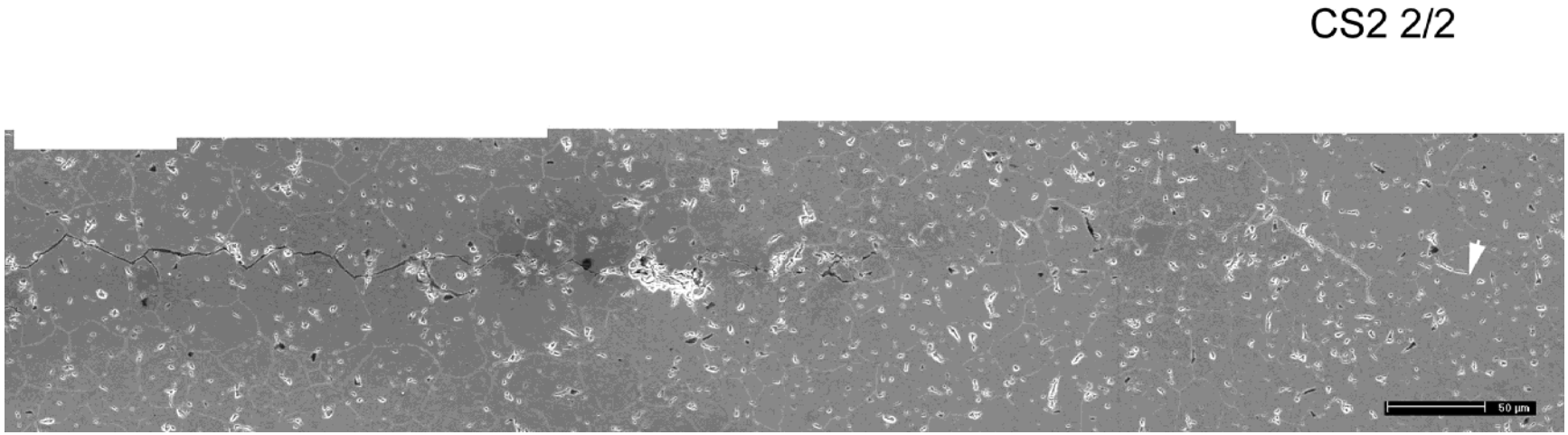

(b)

Figure 23. Cross section of specimen DB-5, second side CS2: (a) first half and (b) second half of the second cross section. Crack advance is from left to right. The arrow marks the end on the crack.

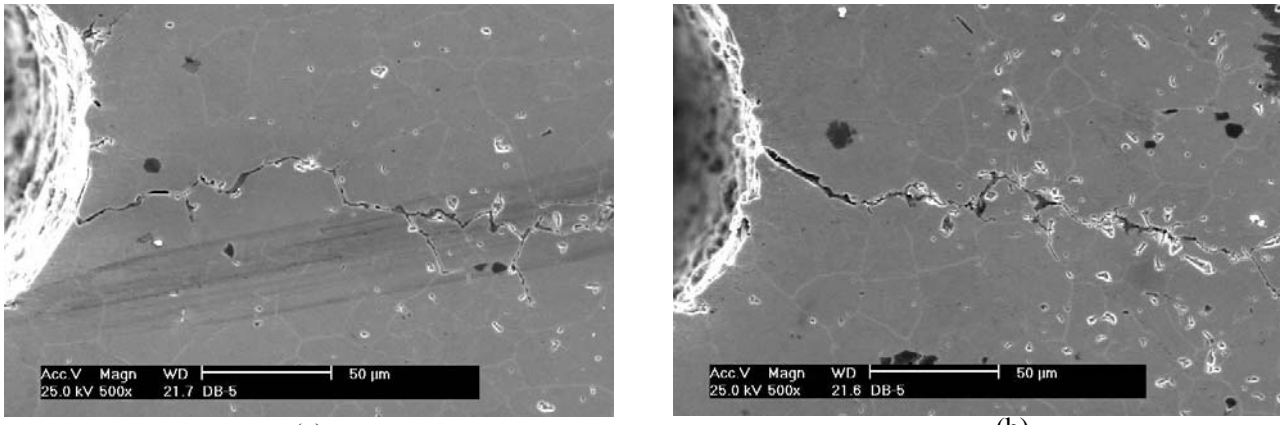

(a) (b)

Figure 24. Cross sections of specimen DB-5 in the region near the notch: (a) first side (CS1) and (b) second side (CS2). Crack advance is from left to right.

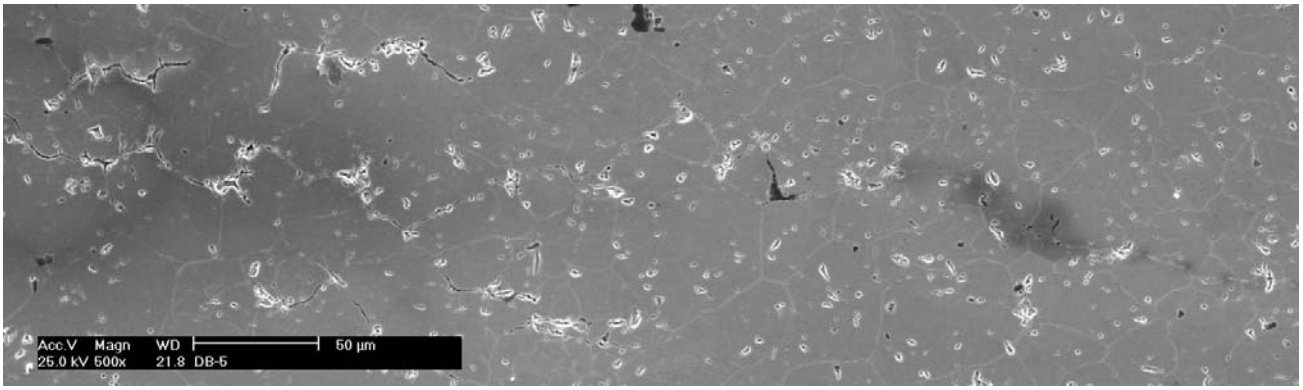

Figure 25. Crack branching on the cross section of specimen DB-5 (location 1 in Fig 22b). Crack advance is from left to right.

After the side surfaces were examined, the specimen was broken open, and the fracture surface was photographed and further examined by SEM. Figure 26 shows the entire fracture surface of specimen DB-5. The relationship with the two cross sections CS1 and CS2, as well as the important milestones of the test are indicated in the figure: the specimen was precracked in water for approximately 0.6 mm, then transitioned to an SCC fracture mode. The change in color/oxidation shows the demarcation between fast and slow cycling approximately. The pre-cracking front is relatively straight, while the SCC crack apparently advanced more rapidly on the right side (CS1) of the specimen than on the left side (CS2). In other words, the material on the left side appears to be less susceptible to cracking than that on the right side. During the two periods of fatigue in air at the end of the test, the coloration changed to light grey, in contrast to the (dark) oxidized surface from the test in water. Several ligaments originating into the water test region have been identified by their light grey appearance and several are indicated by yellow arrows in Fig. 26. It is important to note that the CGR behavior observed while braking these ligaments in

Fig. 17n – initially much faster than the expected value to which the CGR eventually settles - mirrors that reported several times during the test during fatigue test periods following constant load periods, Figs. 18-21.

The sample surface was also examined by SEM. The SEM image of the entire surface was broken into two halves, and these images are shown in Figs. 27 and 28. Not much detail can be distinguished at this magnification; however, the following is readily observed: i) the sample is fully engaged, and IG cracking is extensive, ii) the fracture mode does not appear to change between fatigue precracking and the rest of the test, and iii) secondary IG cracking (branching) is extensive in the later part of the test. In short, these details match the observations made for the cross sections.

Figure 29 is a larger magnification micrograph taken at location A in Fig. 27, and shows extensive IG cracking; the IG fracture mode started during precracking. Overall, the IG cracking observed on this specimen is smooth, as shown at higher magnification in Fig. 30. Figure 31 (location B in Fig. 28) shows extensive secondary cracking that occurred mainly in the later part of the test. This type of cracking leads to branching, and the ligaments of non-cracked material that are left behind can easily confound the DC potential measurements. One such ligament - displaying ductile rupture - can be seen in the center of Fig. 32 (location C in Fig. 28). Note the difference in height (focus) between the two IG areas adjacent to this ligament. This difference suggests that at that location cracking was propagating in two different planes. From an experimental perspective, cycling meeting the EPRI MRP-55[11] criteria appears to have been too gentle to reveal the full extent of crack advance.

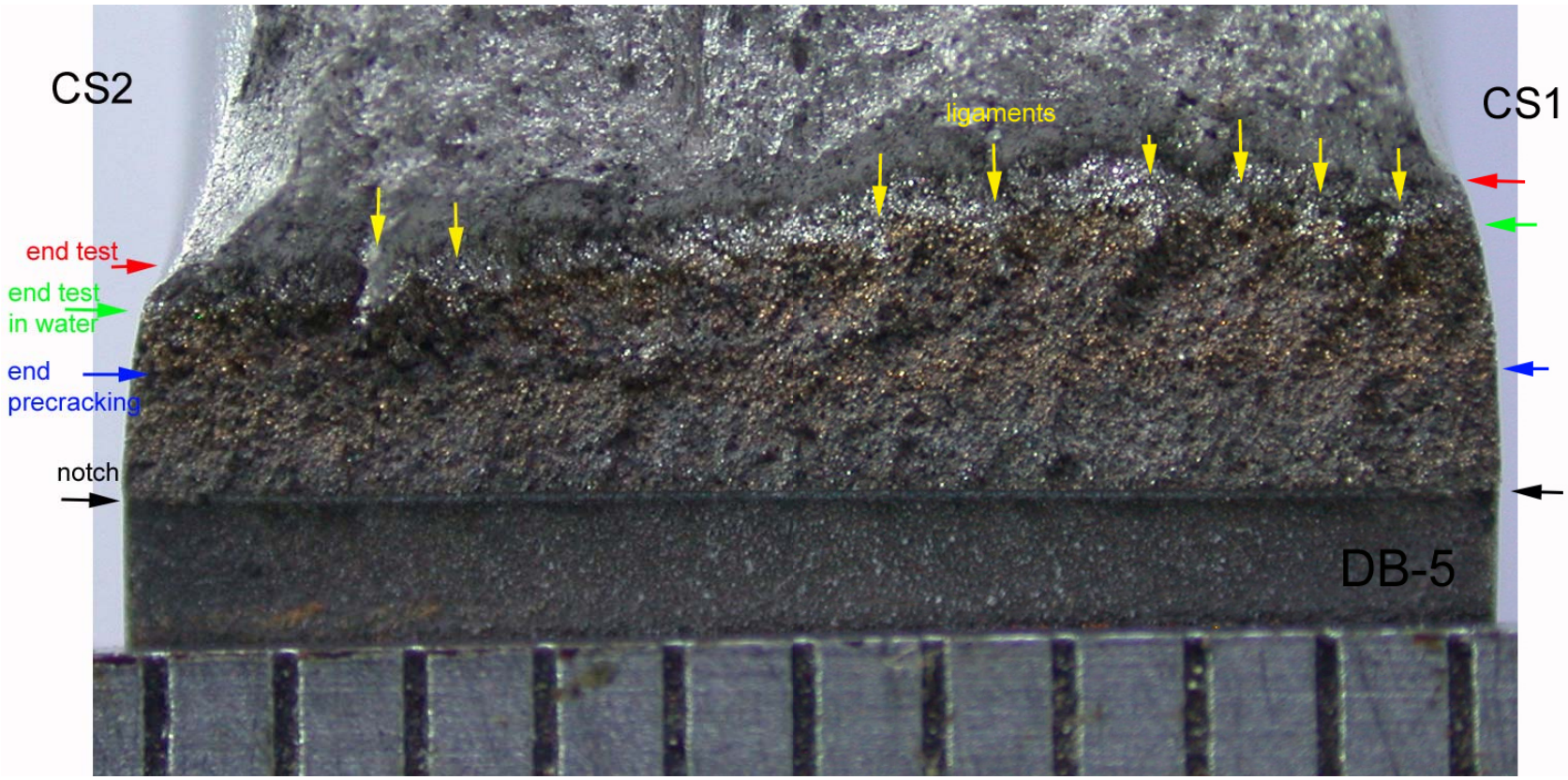

Figure 26. Fracture surface of specimen DB-5. Crack advance is from bottom to top.

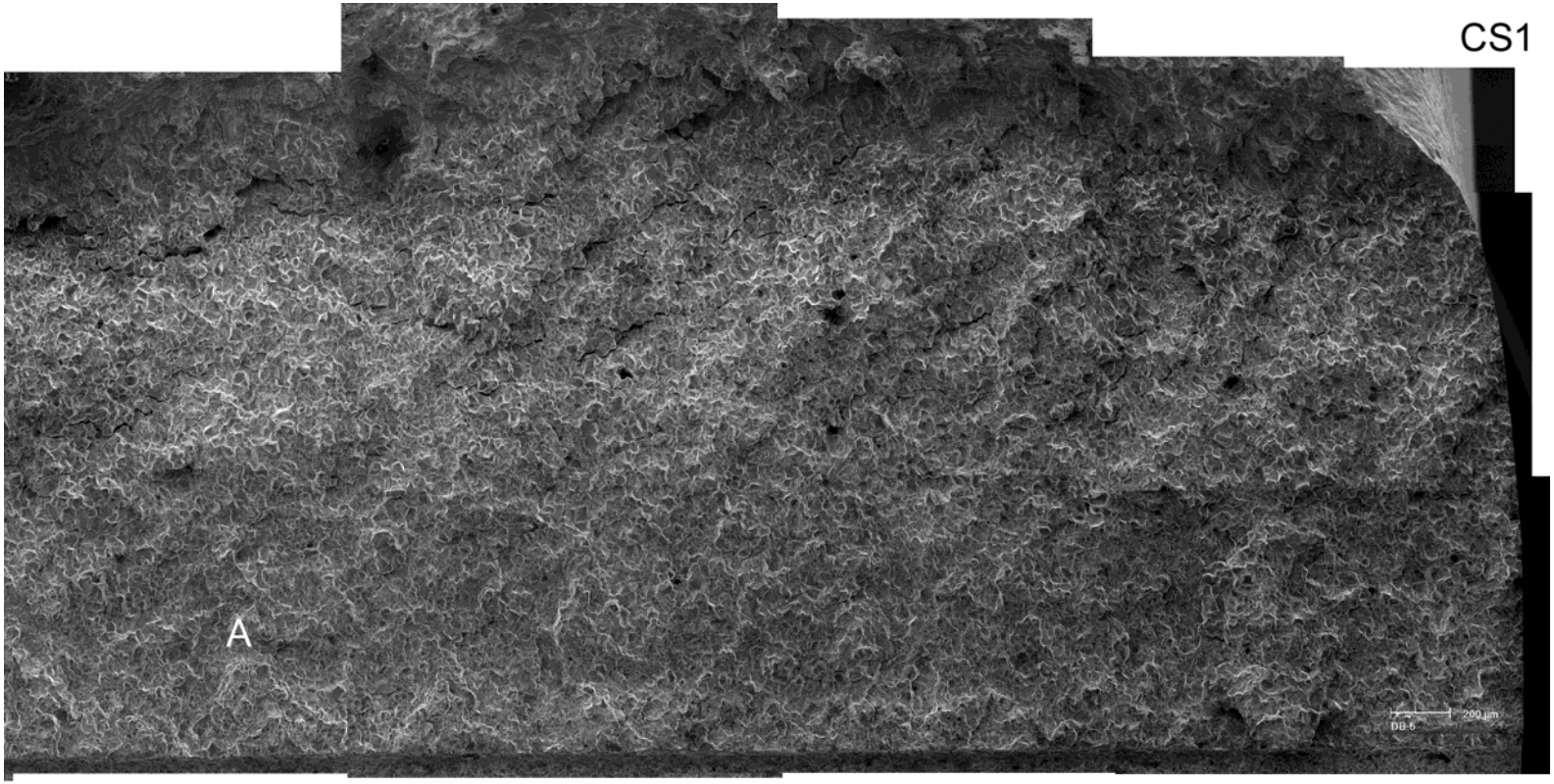

Figure 27. First half of the fracture surface of specimen DB-5. Crack advance is from bottom to top.

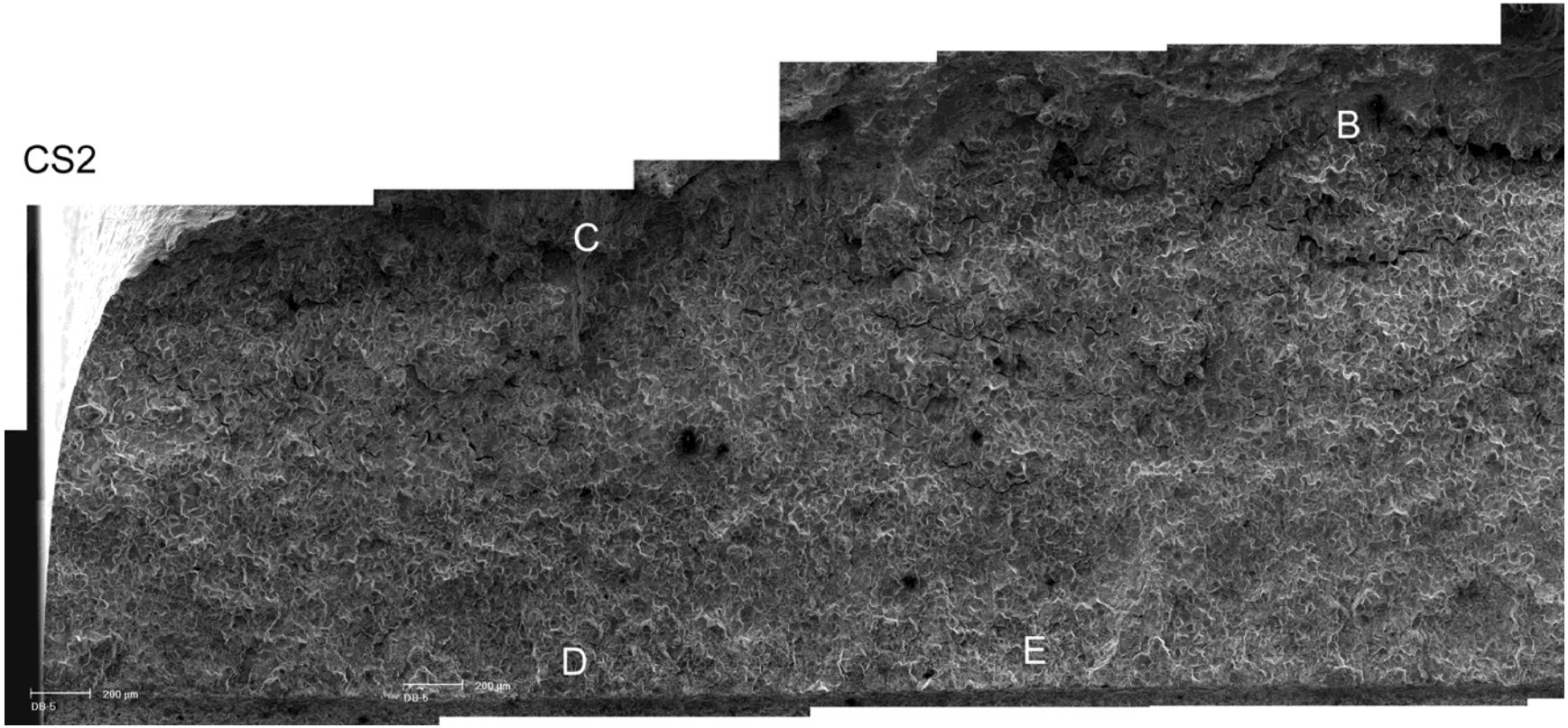

Figure 28. Second half of the fracture surface of specimen DB-5. Crack advance is from bottom to top.

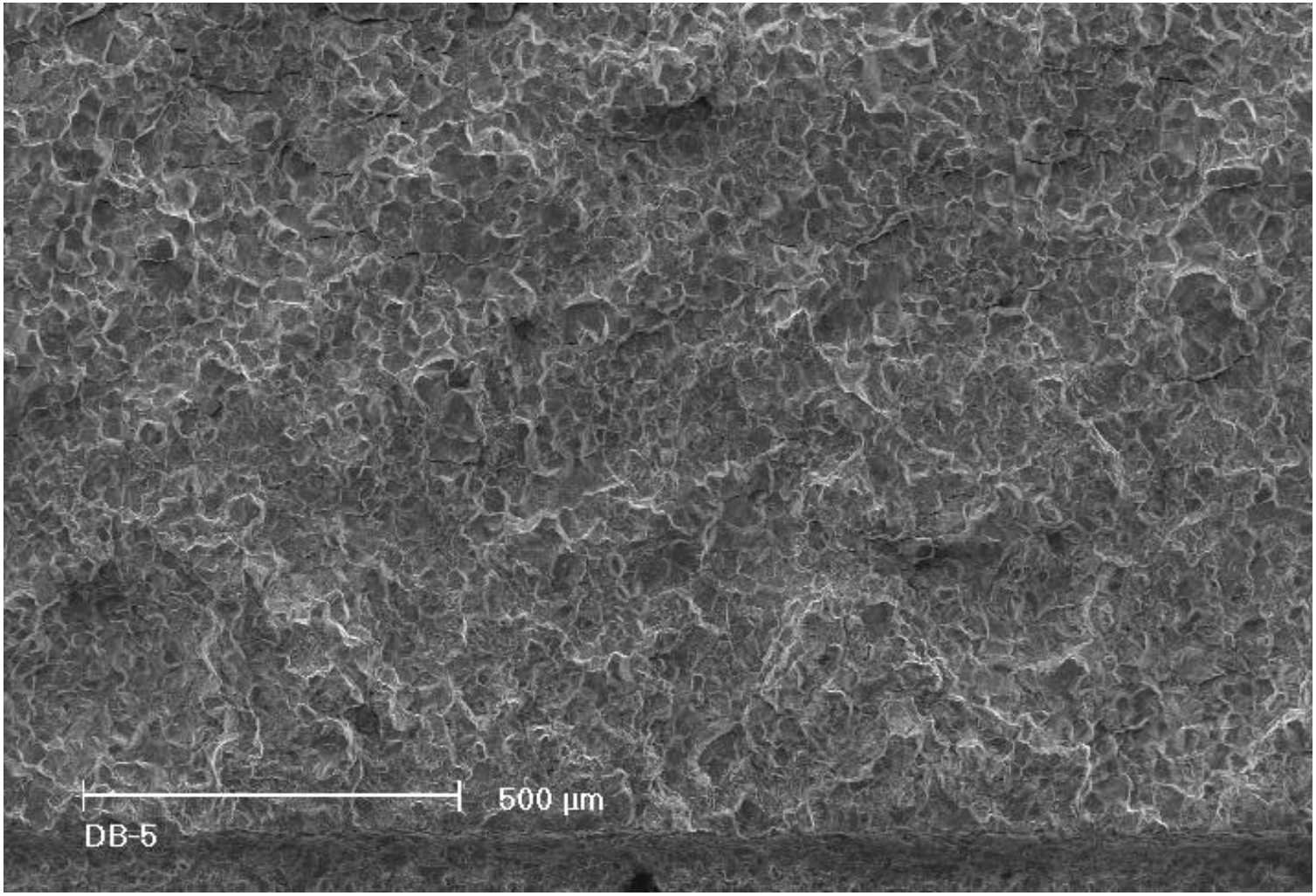

Figure 29. Fracture surface of specimen DB-5 at location A in Fig.27. Crack advance is from bottom to top.

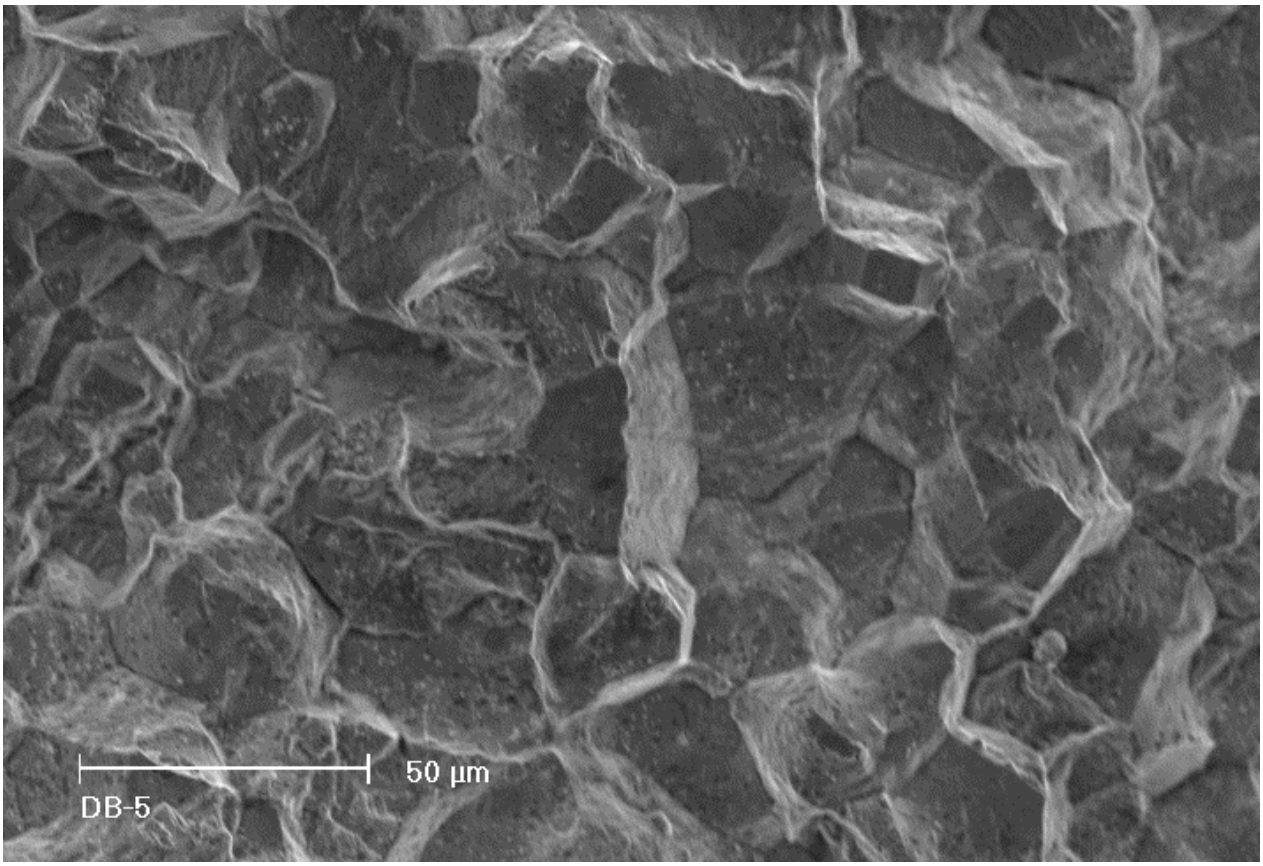

Figure 30. Smooth IG on the fracture surface of DB-5. Crack advance is from bottom to top.

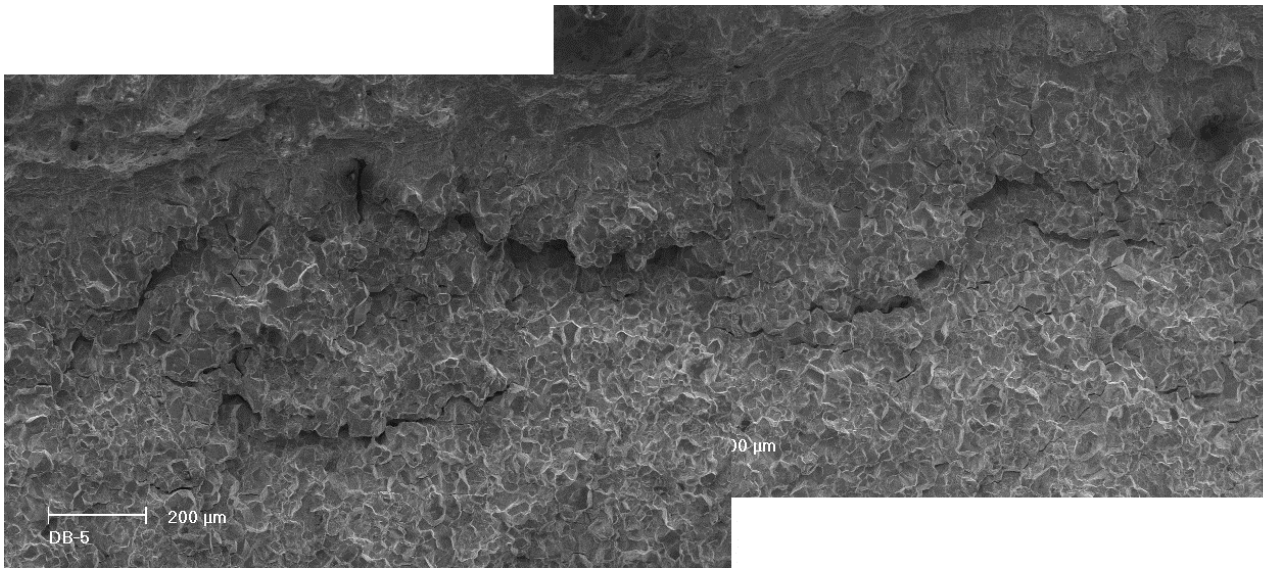

Figure 31. Crack branching on the fracture surface of specimen DB-5 (location B in Fig. 28). Crack advance is from bottom to top.

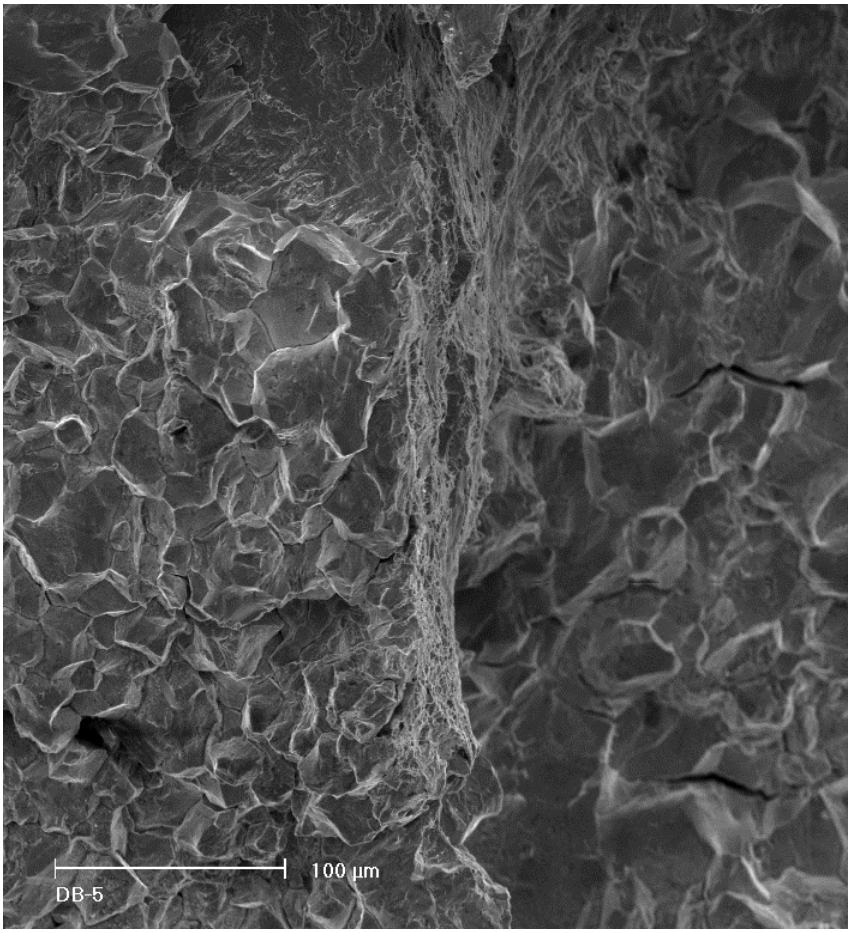

Figure 32. Ligament on the fracture surface of specimen DB-5 (location C in Fig. 28). Crack advance is from bottom to top.

One feature of high interest is the IG fracture mode observed during fatigue precracking. This feature is atypical of Alloy 600 (and other alloys, as well) because the expected fracture mode under such loading is TG. The only exception was the Alloy 600 heat M3935 from Davis-Besse nozzle #3 that was tested at ANL previously.[9]

Figure 33 shows two examples from the precracking region (locations D and E in Fig. 28) from the current specimen DB-5 (Alloy 600 heat M7929). The pictures show that within approximately 50 μm [0.002 in] from the sample notch, the fracture changes from TG to IG and continues as IG for the reminder of the test. A typical alloy would have exhibited a TG fracture mode during the fatigue precracking stage, which for this specimen was approximately 650 μm [0.026 in].

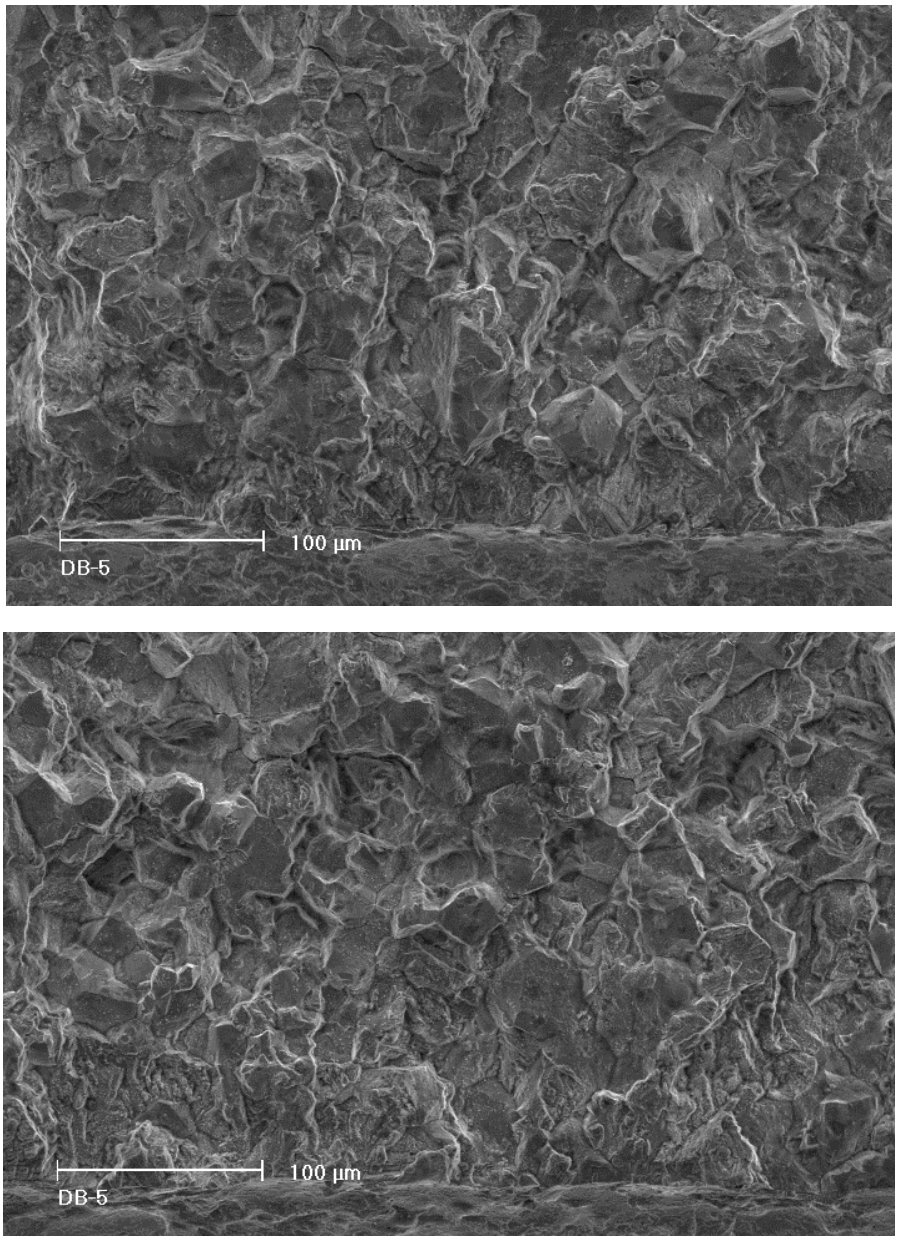

Figure 33. Fracture surface of specimen DB-5 showing the area near the notch during precracking at locations D (a) and E (b) in Fig. 28. Crack advance is from bottom to top.

4.2 Specimen DB-4

Specimen DB-4 was the second specimen to be tested. The objective for the test was to confirm the SCC CGR behavior observed with Specimen DB-5. The testing conditions for this specimen are given in Table 2, and the changes in crack length and K_{max} with time are shown in Fig. 34. The data presented in the table and in the figure reflect a 31% correction factor that was applied uniformly across the data set after the examination of the fracture surface.

In-situ precracking (Pre a – Pre i) was followed by transitioning (test periods 1-2). During period 2, an actuator component failed, and the load started to behave erratically. The system was stabilized, and load control was achieved in "low hydraulic pressure" at 215 h. Attempts to reproduce known fatigue conditions were not successful, and the DC potential measurements appeared to be shorted. At that time, the test was stopped, and the servo valve to the actuator was repaired, and the loading system was verified by an Instron® engineer. The specimen was examined visually to verify that no unexpected condition occurred. The operation of the DC potential system was also verified. Next, the test was restarted in room temperature air, and two known conditions were reproduced in periods 3 and 4. The system was brought back to operating temperature, and another known condition was reproduced in period 5 (similar to periods 7 and 10 for specimen DB-5, Table 1). Nevertheless, the shorting of the DC potential appeared to persist, and this condition imposed a limit on the range of cyclic loading that could be applied to this specimen. These effects will be discussed next.

The pattern of "drops" in the crack advance in period 6 during cyclic loading with 2h-hold at R=0.5 suggests that the two fracture surfaces are touching during unloading, thus causing the DC potential to briefly underestimate the crack length. The IG fracture mode during precracking only complicates the issue. Such an effect is plausible because the large side grooves likely removed the usual constraint on the cracking plane and allowed the crack to wander, causing the crack plane to be not as straight as it normally is in a specimen with more restrictive side groves.

With the above load pattern limitation in mind, two additional transitioning steps were undertaken in periods 7 and 8 at a higher load ratio (R=0.7) expecting to maintain the two fracture surfaces apart. The specimen was set at constant load in period 9, and constant load with periodic unloading in period 10. The crack was advanced by cyclic loading at the maximum allowed stress intensity factor in period 11, and set at constant load with periodic unloading at this stress intensity factor in period 12. The resulting rate seemed similar to those measured previously on specimen DB-5. After a brief period of cycling, the sample was again set at constant load with periodic unloading in test period 14, followed by constant load constant load in test period 15. As the crack appeared to stall towards the end of test period 15, cycling was re-introduced briefly in period 16. The cyclic CGR rate measured in period 16 seems consistent with those measured previously on this alloy. The specimen was again set at constant load in period 17, and the rate seems similar to those measured previously on this specimen at constant load or at constant load with periodic unloading.

In summary, the SCC CGRs measured on specimen DB-4 at 320°C [608°F] appear consistent with those measured on specimen DB-5 at similar stress intensity factors.

In the last part of the test, the temperature was lowered to 290°C [554°F] to determine the activation energy for SCC growth. The dissolved hydrogen concentration in the water was decreased to 11 cc/kg to maintain the same potential difference to the Ni/NiO line as the 320°C [608°F] test condition.

The SCC CGR measured in period 18 was low but consistent with the expected behavior. Subsequent constant load or constant load with periodic unloading periods produced no reliable data. It is believed that by this point in the test, crack branching reached levels that could not be minimized by gentle periodic unloading. Consequently, no valid crack growth rate date was obtained after test period 18.

Table 2. Crack growth data for specimen DB-4 (DB600-CL-1) of Alloy 600 in PWR water.[a]

Test Period	Test Time, h	Temp., °C	Load Ratio R	Rise Time, s	Down Time, s	Hold Time, s	K_{max}, MPa·m$^{1/2}$	ΔK, MPa·m$^{1/2}$	CGR_{env}, m/s	Estimated CGR_{air}, m/s	Crack Length, Mm
Pre a	74	319.0	0.33	1	1		21.7	14.5	1.25E-09	1.04E-08	12.045
Pre b	93	319.0	0.33	100	100		21.7	14.5	7.13E-11	1.05E-10	12.047
Pre c	101	319.6	0.33	1	1		21.9	14.7	6.80E-09	1.09E-08	12.107
Pre d	118	319.5	0.33	50	50		21.9	14.7	8.12E-10	2.19E-10	12.123
Pre e	124	319.5	0.33	1	1		22.3	15.0	1.26E-08	1.18E-08	12.261
Pre f	142	319.4	0.33	50	50		22.4	15.0	1.44E-09	2.40E-10	12.282
Pre g	143	319.4	0.33	1	1		22.6	15.2	1.50E-08	1.25E-08	12.362
Pre h	147	319.4	0.33	2	2		22.8	15.3	1.05E-08	6.46E-09	12.407
Pre i	148	319.4	0.33	5	5		22.8	15.3	5.27E-09	2.60E-09	12.415
Pre j	166	319.4	0.33	50	50		22.9	15.4	1.74E-09	2.64E-10	12.442
1	189	319.4	0.49	300	12		23.1	11.8	3.83E-10	2.28E-11	12.489
2	197	319.4	0.49	600	12		23.1	11.8	3.02E-10	1.14E-11	12.487
	339	319.4									13.196
3	343	27.8	0.30	5	5		23.5	16.4	2.54E-09	1.86E-09	13.343
4	346	27.9	0.30	1	1		23.5	16.5	1.60E-08	9.40E-09	13.356
5	372	319.6	0.50	50	12		20.5	10.3	1.19E-09	8.03E-11	12.440
6	579	319.7	0.50	600	12	7200	24.7	12.4	4.15E-11	1.11E-12	13.510
7	655	319.7	0.70	300	12		24.3	7.3	6.32E-11	6.81E-12	13.530
8	683	319.6	0.70	300	12	7200	24.3	7.3	1.69E-11	2.72E-13	13.529
9	942	319.5	1	0	0		24.4	0.0	4.30E-12	-	13.539
10	1180	319.7	0.50	12	12	7200	24.7	12.3	4.46E-11	1.19E-12	13.576
11	1,251	319.7	0.70	300	12		28.4	8.5	1.55E-10	1.28E-11	13.637
12	1,409	319.7	0.50	12	12	7,200	28.7	14.3	7.06E-11	2.21E-12	13.654
13	1,414	319.8	0.50	600	12		28.6	14.3	5.71E-10	2.61E-11	13.663
14	1,694	319.7	0.49	12	12	7,200	29.0	14.8	5.99E-11	2.42E-12	13.711
15	1,935	319.7	1	0	0		29.2	0.0	3.45E-11	-	13.730
16	1,940	319.7	0.50	600	12		29.6	14.8	7.53E-10	3.01E-11	13.810
17	2,673	319.5	1	0	0		29.8	0.0	3.69E-11	-	13.857
18	2,840	289.4	1	0	0		30.2	0.0	4.07E-12	-	13.869
19	3,025	289.4	0.5	12	12	7,200	30.4	15.2	-	-	13.902
20	3,114	289.4	1.00	0	0		30.2	0.0	-	-	13.866
21	3,124	289.4	0.50	12	12	14,400	30.4	15.2	-	-	13.901
22	3,151	289.4	1.00	0	0		30.4	0.0	-	-	13.904
23	3,223	289.4	0.50	12	12	28,800	30.4	15.2	-	-	13.895
24	3,245	289.4	1.00	0	0		30.3	0.0	-	-	13.890
25	3,295	289.4	0.50	12	12	28,800	30.4	15.2	-	-	13.906

[a]Simulated PWR water with 2 ppm Li, 1100 ppm B, and 2 ppm. DO<10 ppb. Conductivity was 21±3 µS/cm, and pH 6.4.

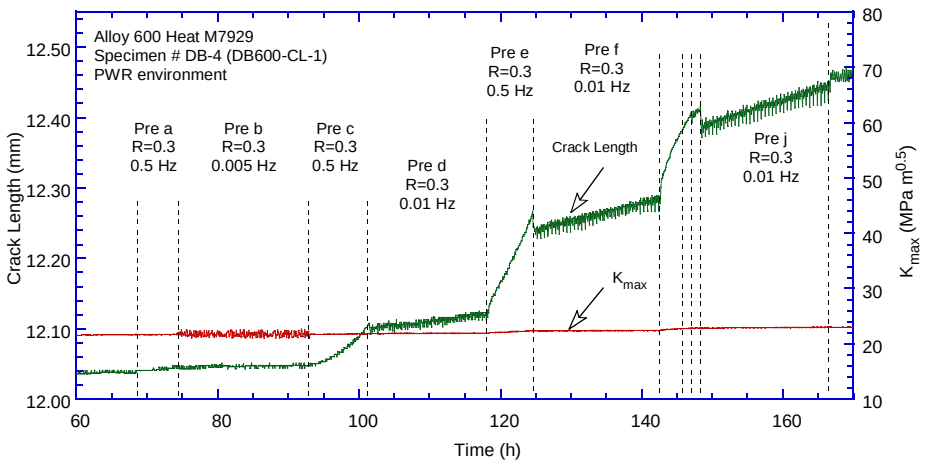

(a)

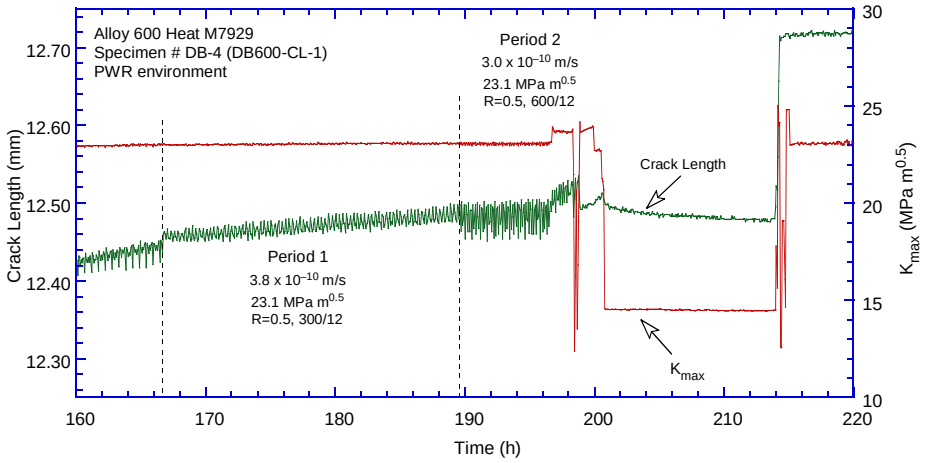

(b)

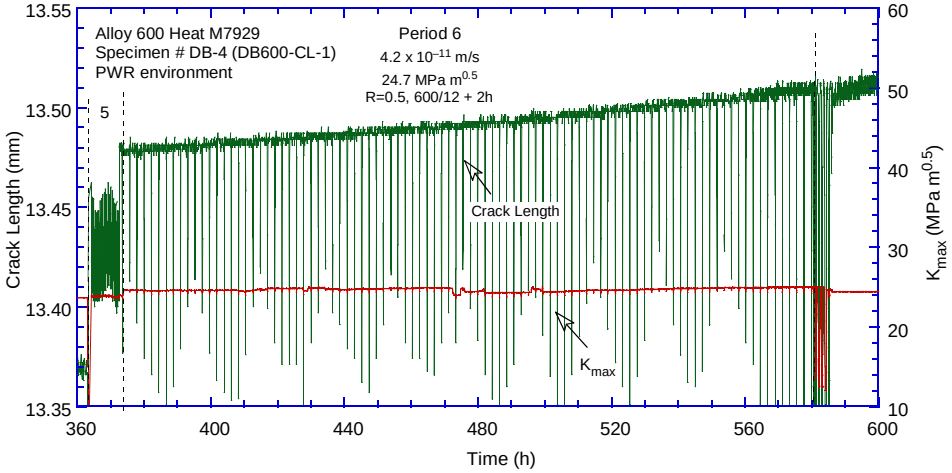

(c)

Figure 34. Crack length vs. time for Alloy 600 heat M7929 specimen DB-4 in simulated PWR environment during test periods: (a) precracking, (b) 1-2, (c) 5-6, (d) 7-8, (e) 9, (f) 10, (g) 11, (h) 12-13, (i) 14, (j) 15-16, (k) 17, and (l) 18.

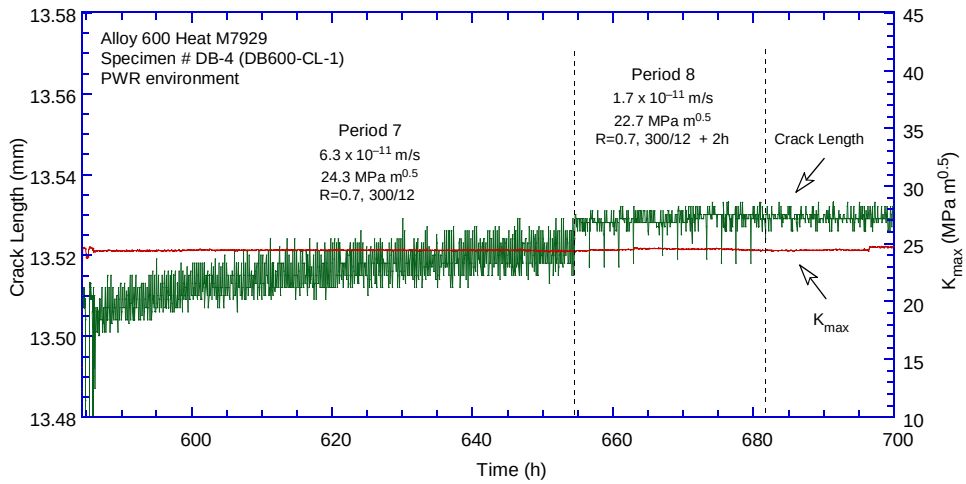

(d)

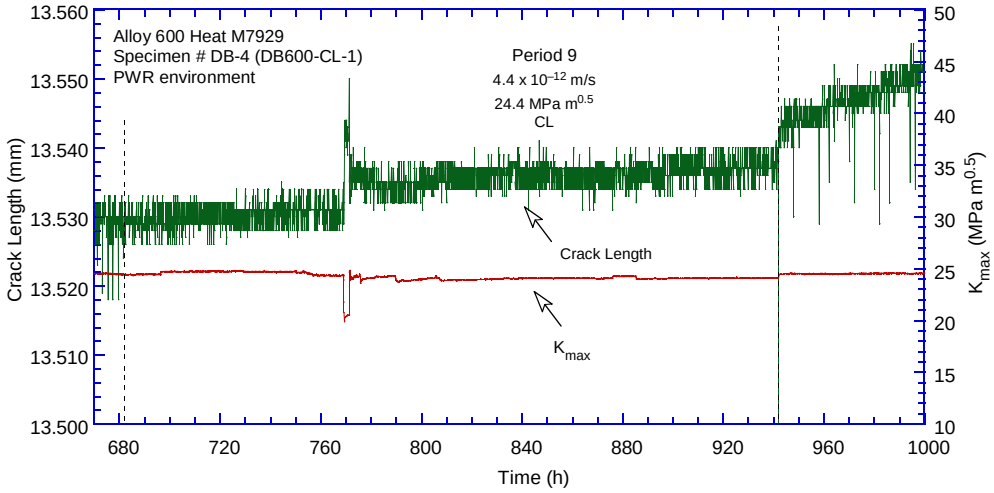

(e)

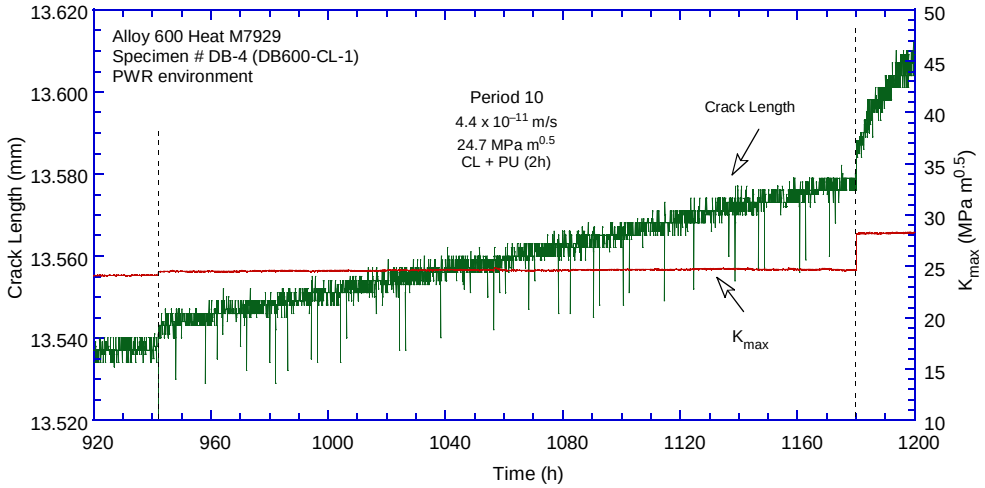

(f)

Figure 34. (cont.)

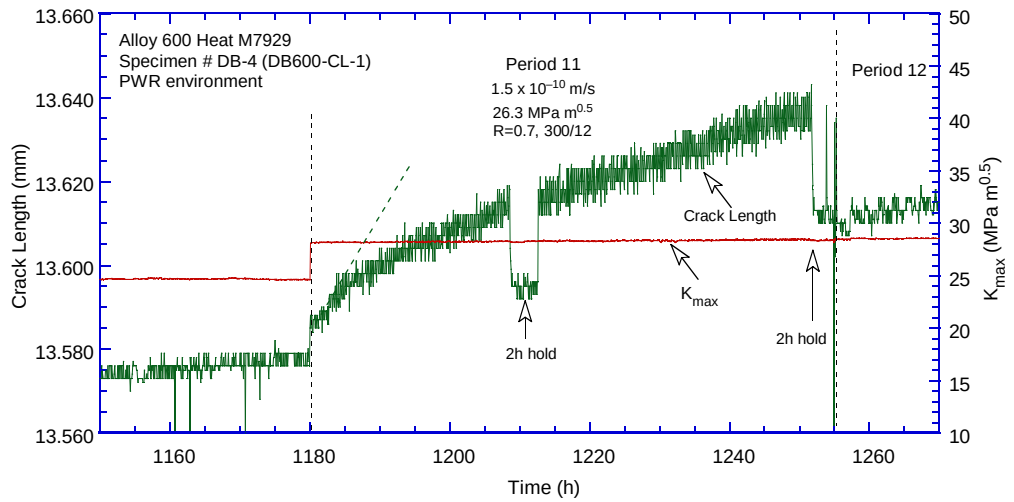

(g)

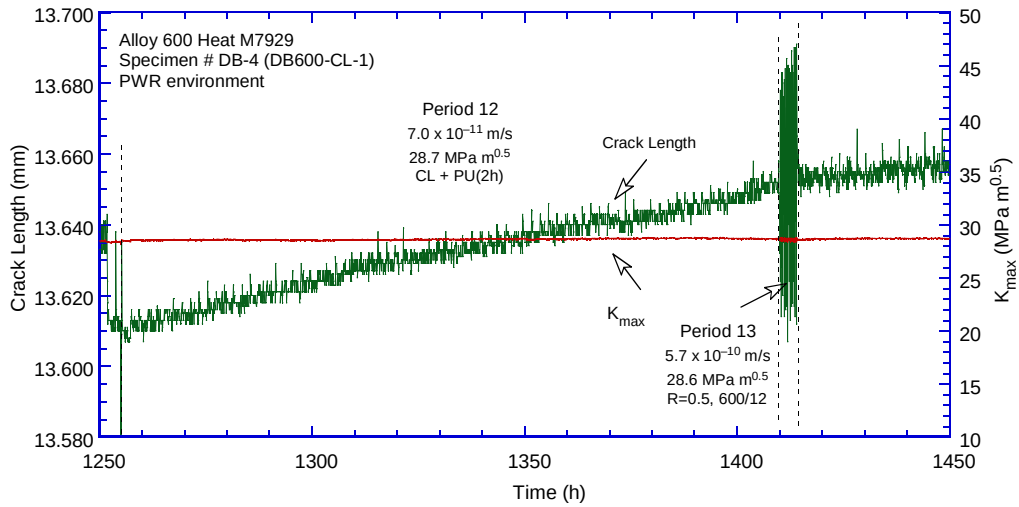

(h)

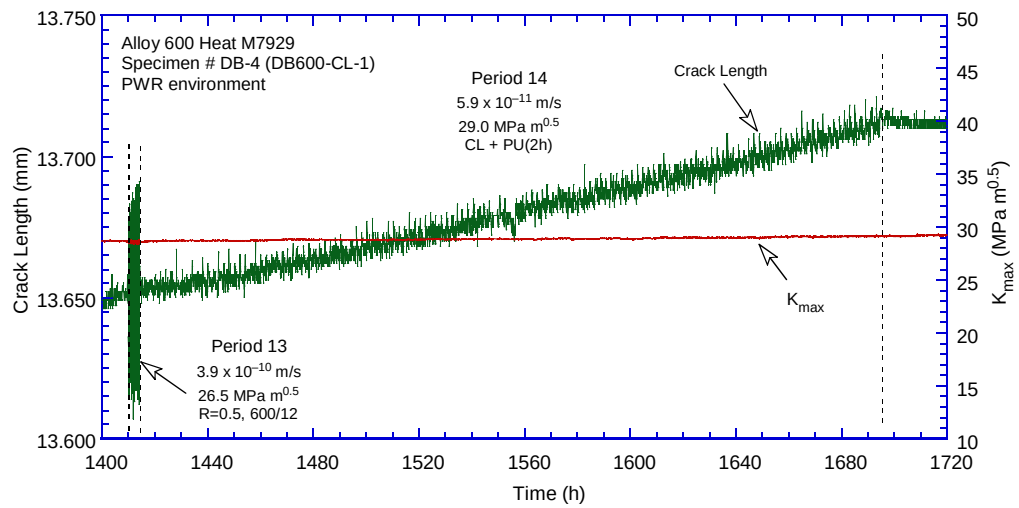

(i)

Figure 34. (cont.)

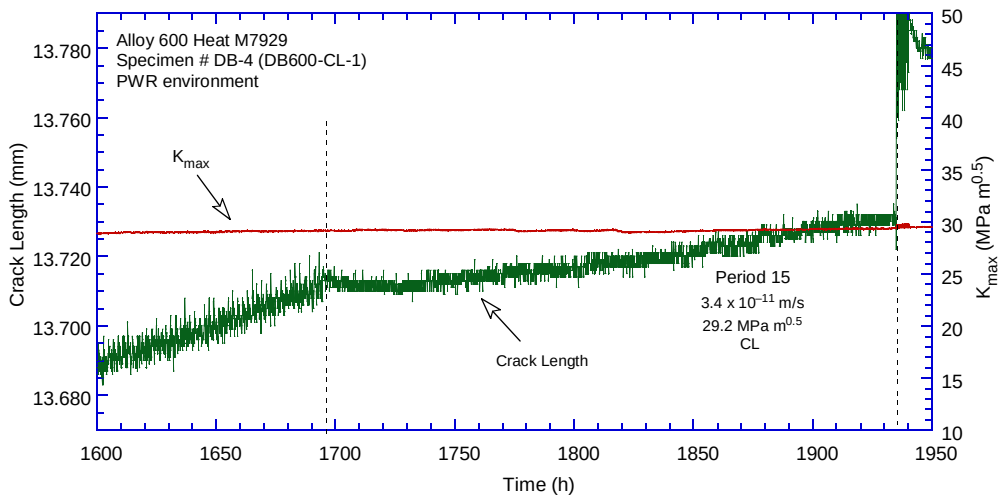

(j)

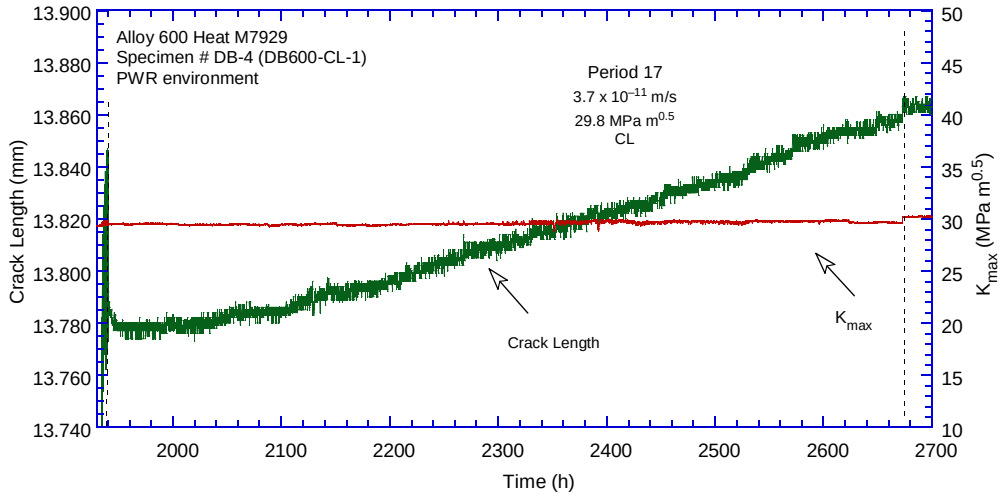

(k)

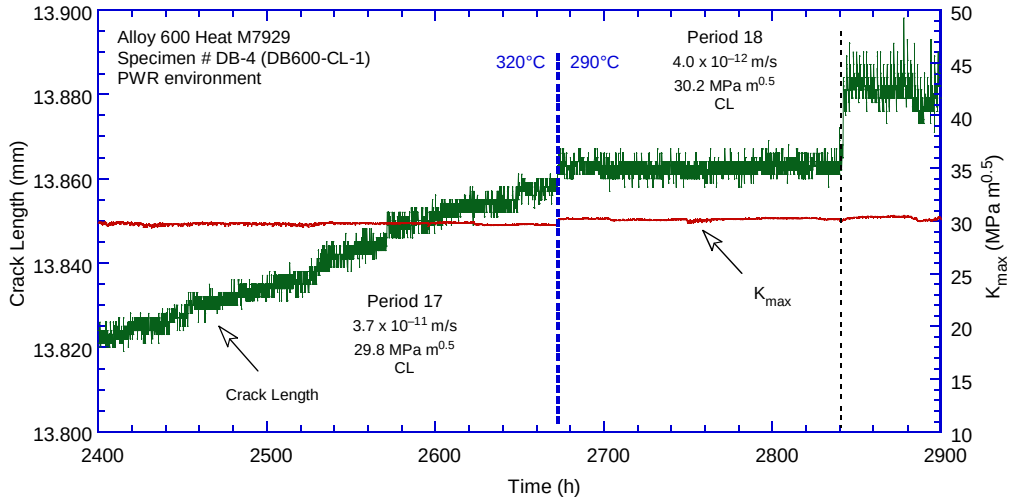

(l)

Figure 34. (cont.)

After the test was completed, Specimen DB-4 was examined in cross sections and at the fracture surface. Figures 35 and 36 show the two sides of the specimen in cross section; these are marked CS1 and CS2. The white arrows in each figure mark the end of the test. Both figures show that despite the large side grooves of this specimen, the crack was largely maintained in plane. Overall, the crack appears intergranular. Moreover, the IG fracture mode appears to start right from the notch. The feature indicated by a red arrow in Fig. 35 spans across the upper and lower crack surfaces, and it can readily be envisioned how it can confound the DC potential measurements by shorting the two surfaces.

The specimen was broken open, and the sample surface was examined by SEM. Figure 37 shows the entire fracture surface. The relationship with the two cross sections CS1 and CS2 is indicated in the figure. Overall, the fracture surface is relatively straight, and, as with the specimen DB-5, the fracture mode appears to be entirely IG. Figure 38 is a higher magnification micrograph from the center of the fracture surface (area between the two arrows in Fig. 37). The yellow arrows indicate the approximate end of transitioning, and the red arrows indicate the end of the test. The figure shows that the fracture mode stayed entirely IG throughout the test, with extensive secondary cracking and branching in the latter part of the test. Figure 39a (location A in Fig. 37) corresponds to the end of test period 2 and also coincides with the area where the actuator failed. The picture shows that despite the fast cycling that was introduced subsequently, the fracture surface stayed largely IG, with only a few small areas of TG cracking. By contrast, Fig. 39b shows the type of smooth IG observed predominantly on the fracture surface of this specimen. Figure 40 is a micrograph taken at the end of the test (location B in Fig. 37) in an area where the fracture mode was not obstructed by the ligaments that formed in the latter part of the test. The red arrows indicate where the test ended, and the figure demonstrates that the fracture mode remained IG through the test periods at 290°C [554°F].

As with the test on specimens DB-5, extensive secondary cracking and branching seem to have developed in the latter part of the test on specimen DB-4. Figure 41a (location C in Fig. 37) is one such example of secondary cracking, and Fig. 41b (location D in Fig. 37) shows an example of a ligament. As described previously in this report, such features can cause the DC potential measurements to underestimate the real crack advance.

Finally, a feature of great interest is the IG fracture mode that occurred during precracking in water. Figure 42 is an example obtained in the notch area of the specimen (location E in Fig. 37), and shows that IG cracking developed very early in the test, sometimes at the first grain boundary encountered. This fracture mode is atypical of the loading condition, and was observed only in companion specimen DB-5 from the Davis-Besse replacement reactor pressure vessel head nozzle #4 (Alloy 600 heat M7929) and the nozzle #3 (Alloy 600 heat M3935) obtained from the original Davis-Besse reactor pressure vessel head that was previously tested at ANL[2]. A typical alloy would have exhibited a transgranular fracture mode during fatigue precracking, which for Specimen DB-5 was approximately 450 μm [0.018 in]. IG fracture under such aggressive testing conditions suggests that the grain boundaries are highly susceptible to IG cracking.

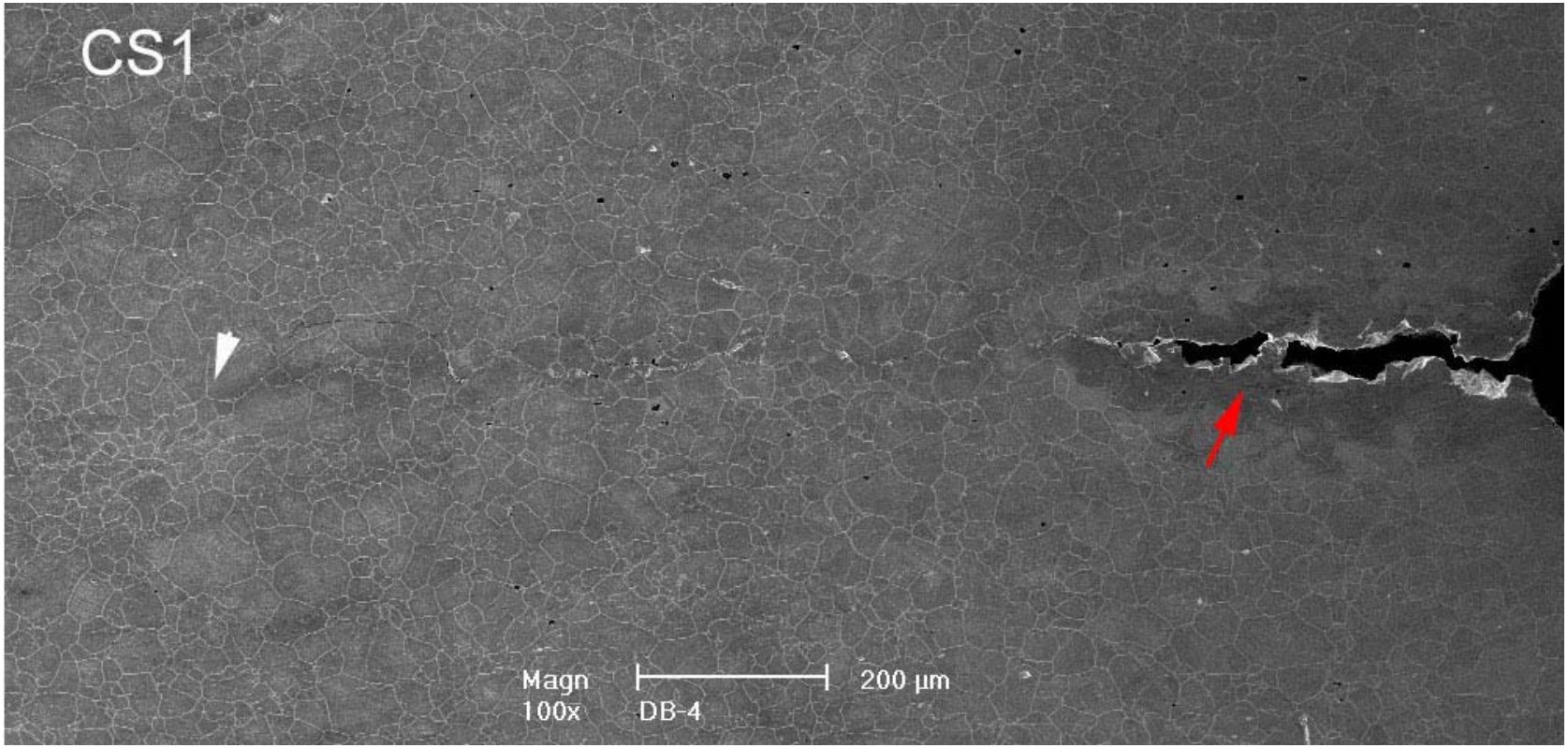

Figure 35. Cross section of specimen DB-4: first side. The white arrow indicates the end of the test. Crack advance is from right to left.

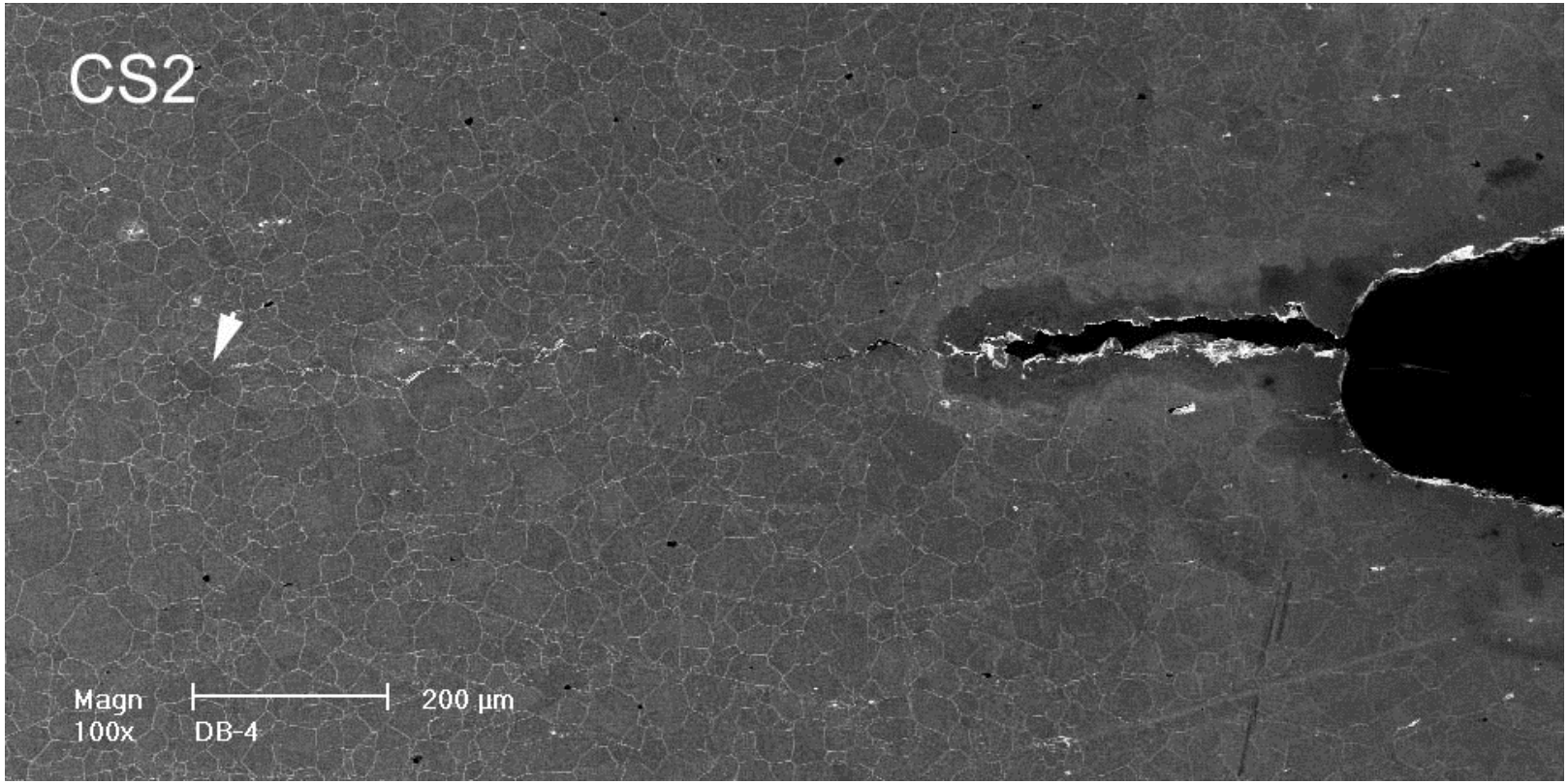

Figure 36. Cross section of specimen DB-4: second side. The white arrow indicates the end of the test. Crack advance is from right to left.

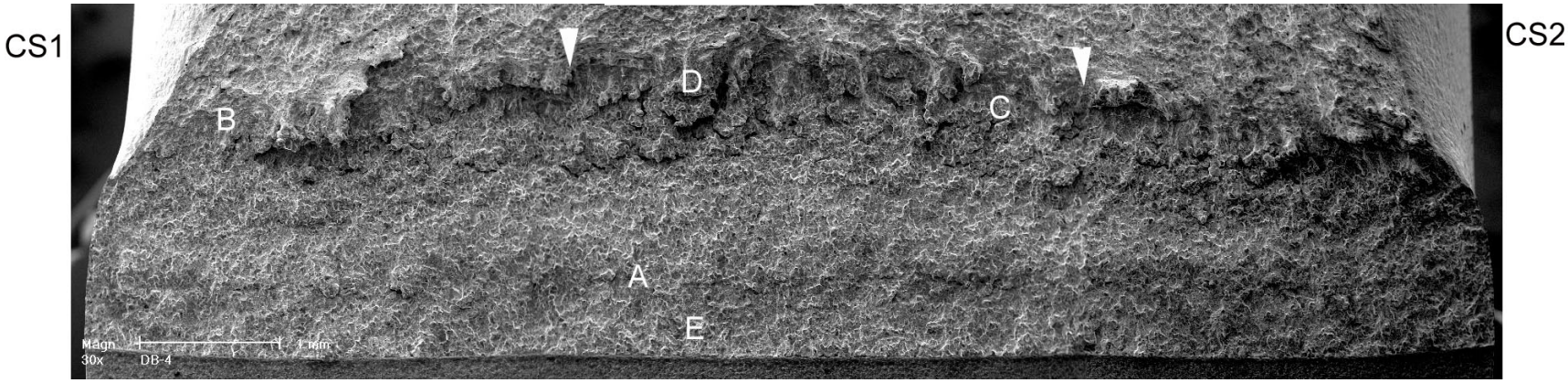

Figure 37. Full fracture surface of specimen DB-4 tested in primary water environment. Crack advance is from bottom to top.

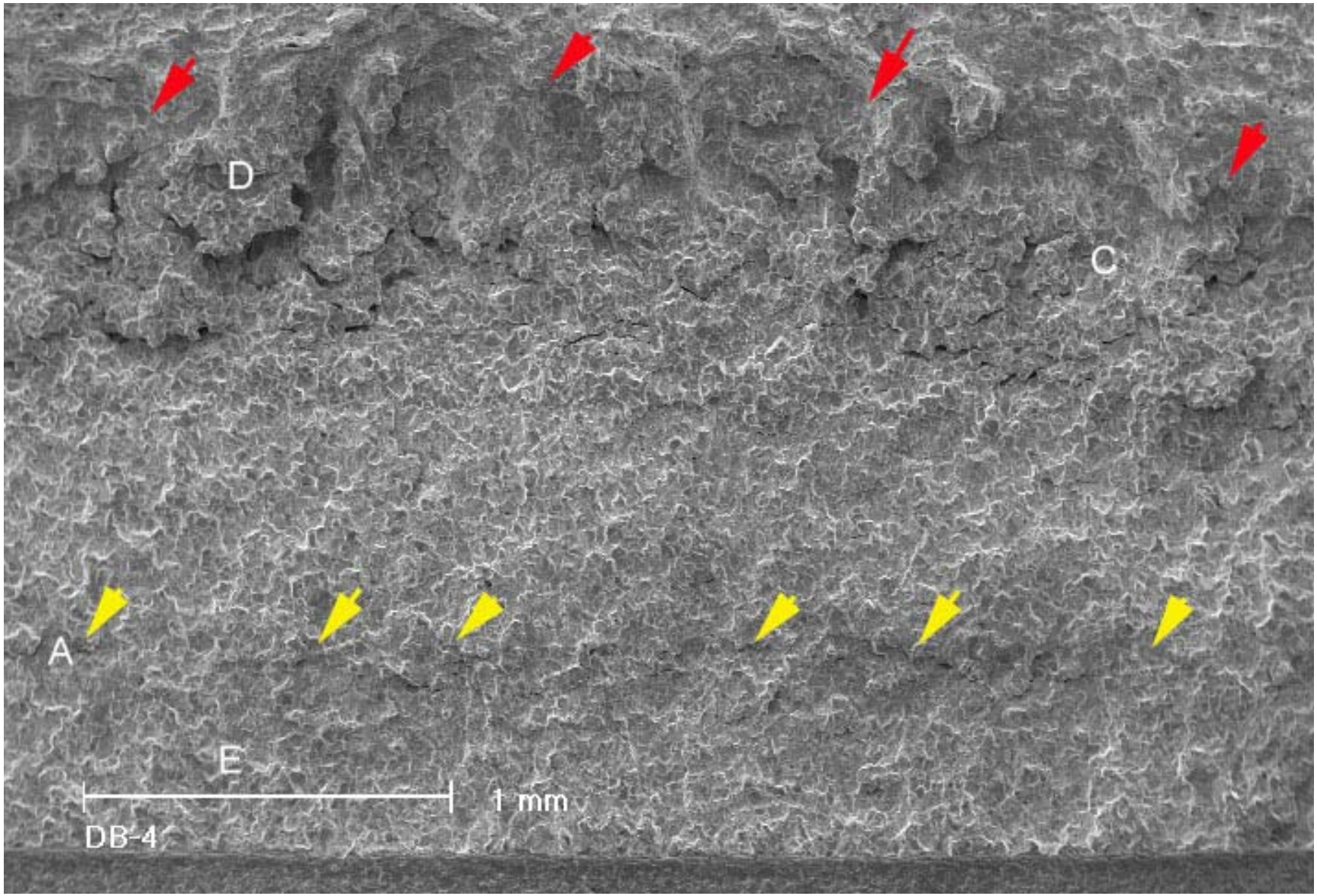

Figure 38. Higher magnification of full fracture surface of specimen DB-4 tested in primary water environment. The yellow arrows indicate the approximate end of transitioning, and the red arrows indicate the end of the test. Crack advance is from bottom to top.

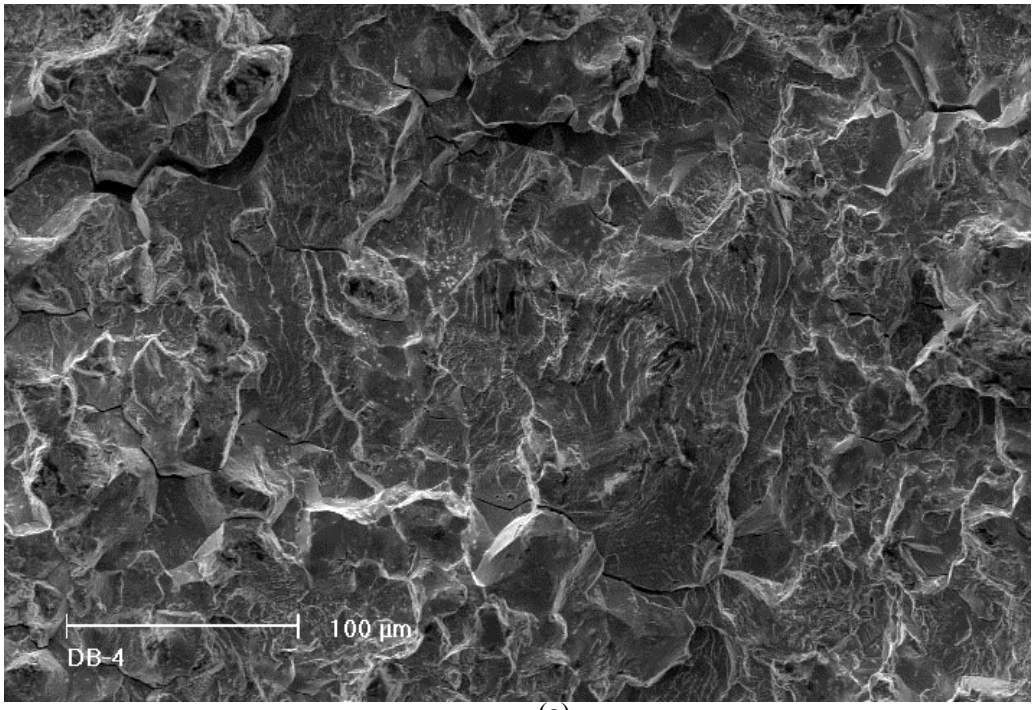

(a)

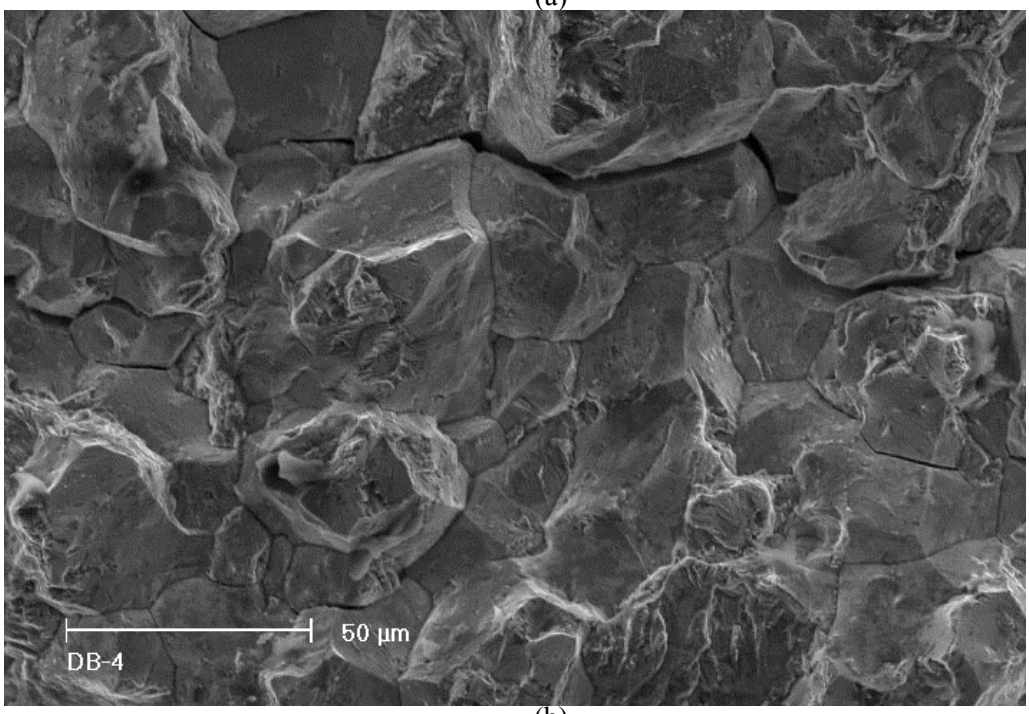

(b)

Figure 39. Fracture surface of specimen DB-4: (a) islands of TG fracture (location A in Fig. 38), and (b) example of smooth IG fracture observed predominantly on the fracture surface of this specimen. Crack advance is from bottom to top.

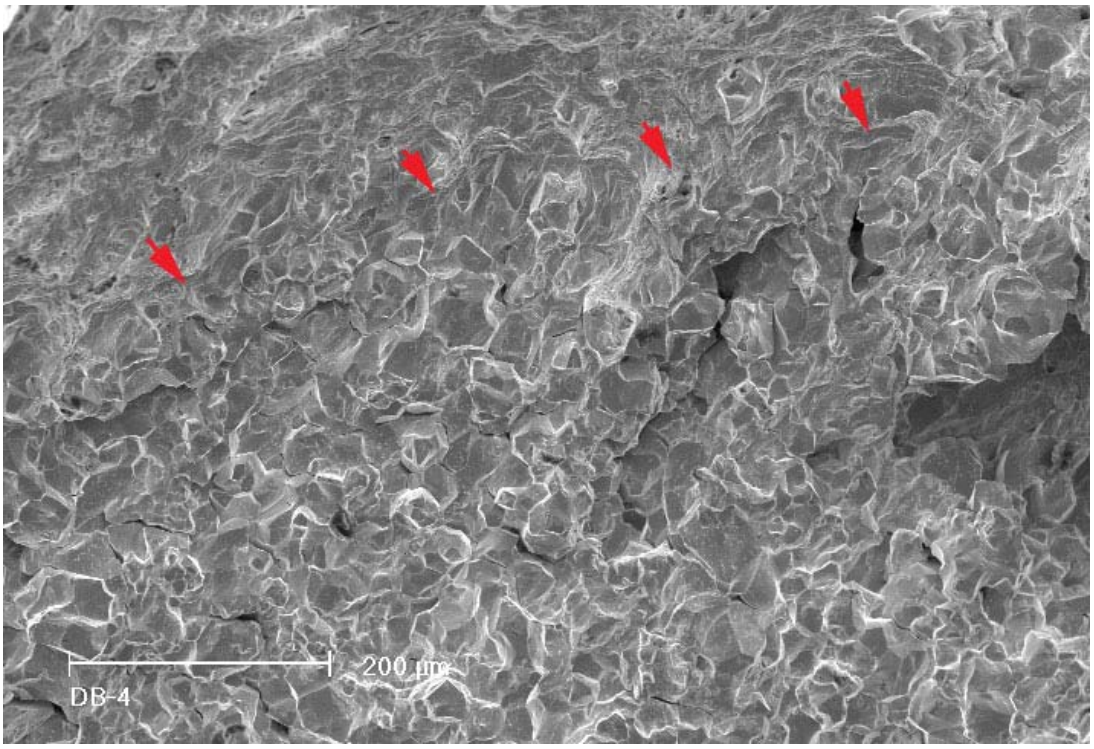

Figure 40. Intergranular fracture at the end of the test on specimen DB-4 (location B in Fig. 37). The red arrows indicate the end of the test. Crack advance is from bottom to top.

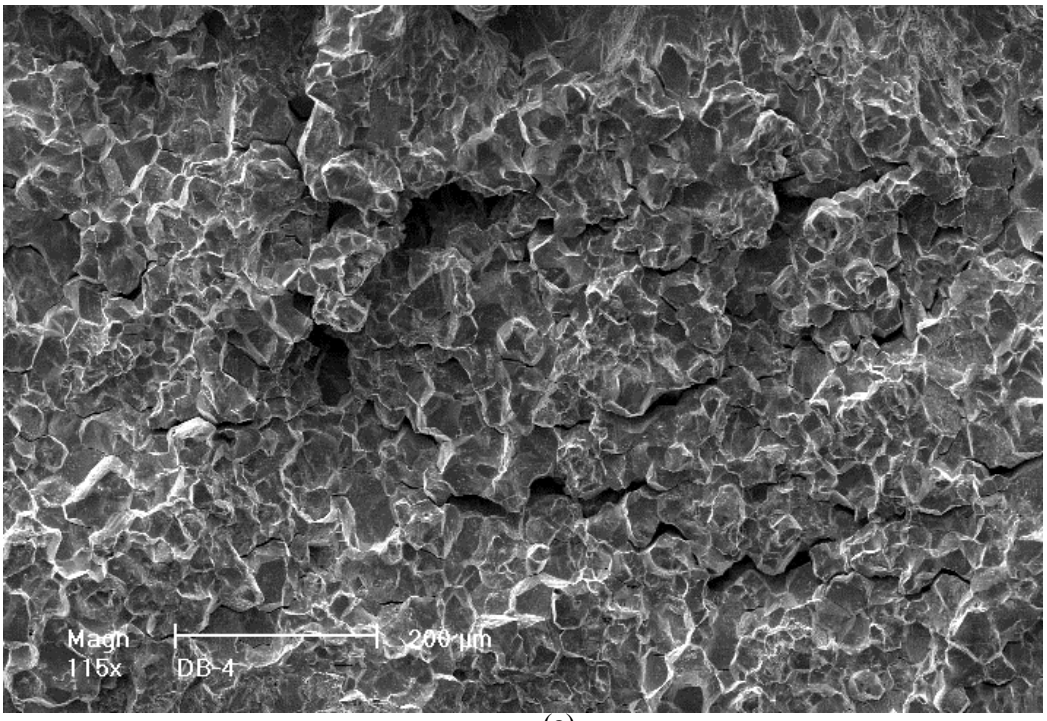

(a)

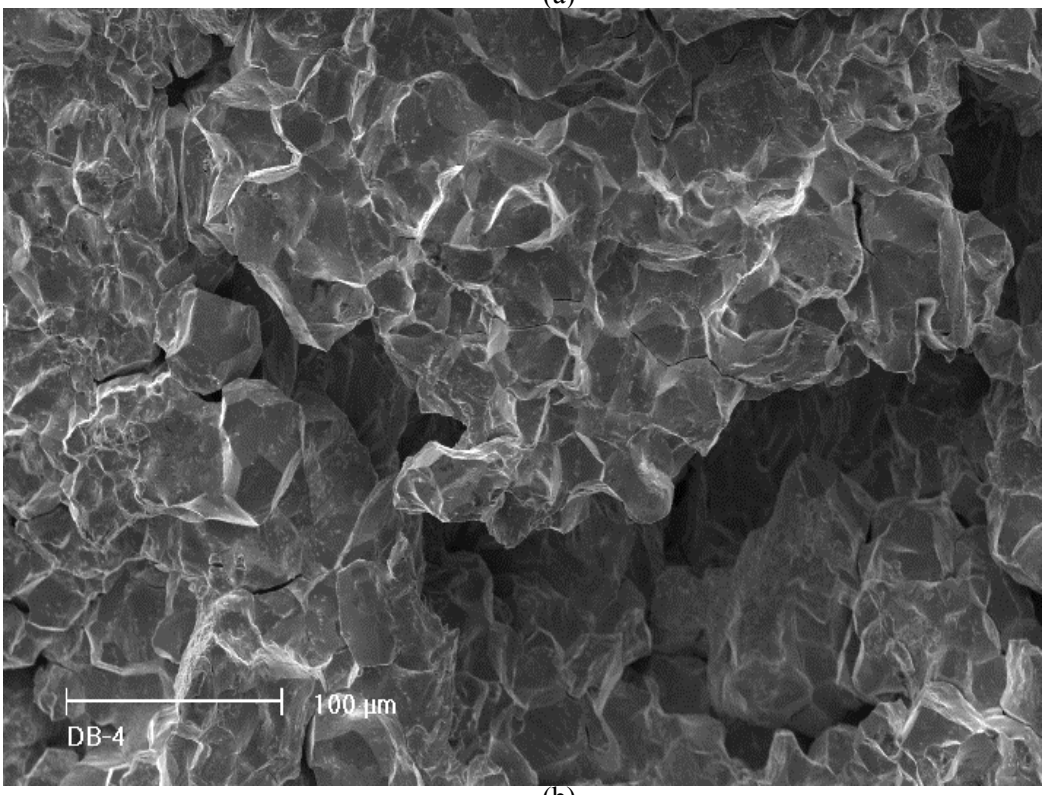

(b)

Figure 41. Fracture surface of specimen DB-4: (a) secondary cracking (location C in Fig. 37), and (b) ligament.(location D in Fig. 37). Crack advance is from bottom to top.

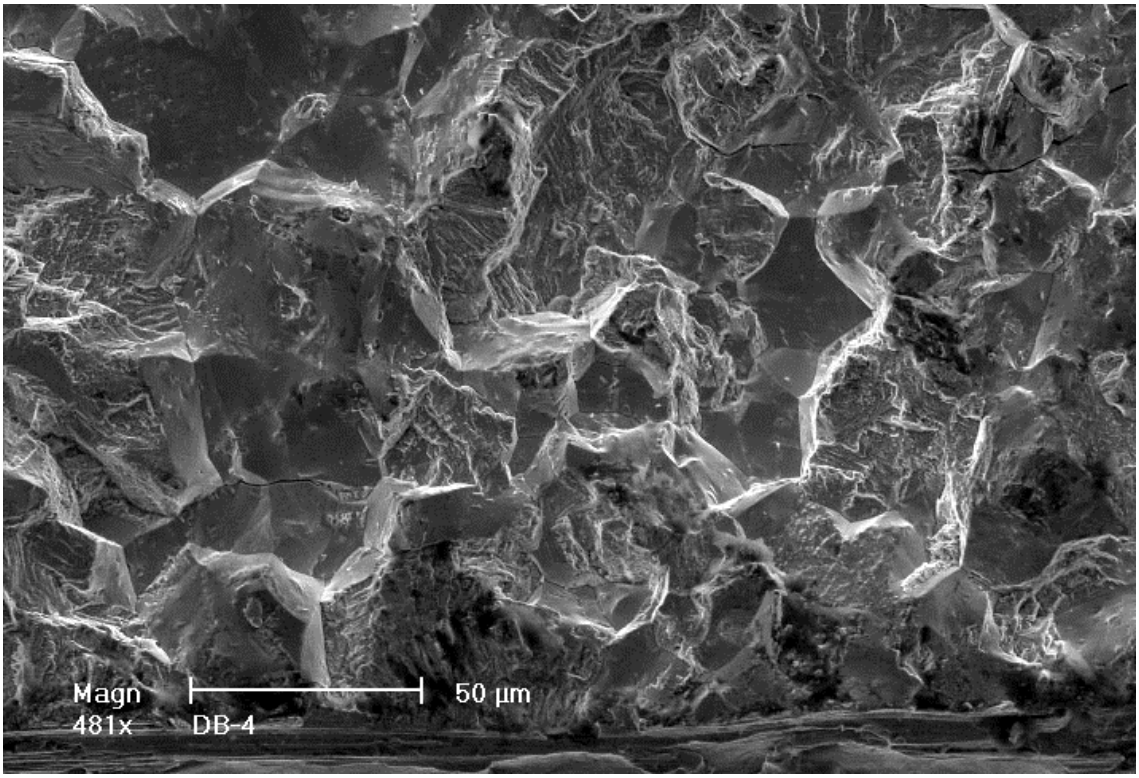

Figure 42. Intergranular fracture during fatigue precracking notch in specimen DB-4 tested in primary water (location E in Fig. 37)). Crack advance is from bottom to top.

4.3 Specimen DB-3

Specimen DB-3 was the third specimen of the Davis-Besse replacement nozzle Alloy 600 heat M7929 to be tested, however, it was the first one in the CR orientation, Figure 6. The objective for this test was to determine the SCC CGR behavior in the new orientation at two stress intensity levels, i.e., at a relatively low stress intensity factor and at the maximum stress intensity factor allowed for its 1/4T CT configuration. The testing conditions are given in Table 3, and the changes in crack length and K_{max} with time are shown in Fig. 43. The data presented in the table and in the figure reflect a 11% correction factor that was applied uniformly across the data set after the examination of the fracture surface.

As with the previous two tests, in-situ precracking was conducted in the PWR environment, however, these tests have shown that the fracture mode in the replacement alloy is largely IG irrespective of the loading condition. As such, a lengthy transitioning routine was unnecessary for this alloy. More, in order to minimize the formation of ligaments and their interference with the DC potential measurements and allow for the measurement of the SCC CGR at constant load, crack advance during precracking and transitioning was kept at a minimum. The straightness of the crack front was ensured by reproducing known fatigue CGRs several times during the test.

Initially, precracking was attempted at stress intensity values as low as 10 MPa $m^{1/2}$ [9.1 ksi $in^{1/2}$], Fig. 43a. Despite the otherwise aggressive loading (R=0.2, 2 Hz), cracking did not initiated readily until the stress intensity factor was gradually increased to 14 MPa $m^{1/2}$ [12.7 ksi $in^{1/2}$]. Hence, the low stress intensity stage of the test was conducted at in the range 14-15 MPa $m^{1/2}$ [12.7-13.6 ksi $in^{1/2}$]. After minimal transitioning, SCC CGRs were measured at constant load in periods 8-10. Overall, the growth at constant load is well-behaved, and the system resolution was approx. 0.3 μm. In all three constant load periods, the SCC CGRs were initially higher, however, a slight decrease was observed over time in each instance. In the EPRI MRP-55[11] framework, these rates rank at 75th percentile.

The test continued with fast/slow cycling at intermediate stress intensity factors (periods 11-14) with the purpose of re-confirming the environmental enhancement. The behavior observed in test period 14 (Fig. 43f) suggests that ligaments were forming even during gentle cyclic loading. Hence, in the subsequent test periods it was attempted to straighten the fracture surface by fast cycling, then setting the specimen directly at constant load. Such a sequence was attempted first in test periods 15 and 16. The high CGR observed at the introduction of cyclic loading in test period 17, Fig. 43h, suggests that the SCC CGR rate was larger than that measured by the DC potential. The approach was repeated in test periods 18-19, followed by and constant load with periodic unloading condition every 1h - the most aggressive loading condition allowed by the EPRI MRP-55[11] - in test period 20. However, the resulting rates were low. This test period was followed by constant load in period 21 for an extended period of time, and the measured CGR was again low. When cyclic was re-introduced in period 22, an initial high CGR was observed, Fig. 43l. As described previously in Section 2.4, this rapid growth is due to breaking of ligaments that had formed during the test period at constant load. If this extra growth (blue arrow in Fig. 42l) is accounted for in test period 21, the resulting rate (8×10^{-12} m/s, green dotted line in Fig. 43k) is in excellent agreement with that measured in period 20. The crack was advanced slightly (approx. 0.08 mm) in test periods 22-27, and set at constant load again in period 28, Fig. 43n. The resulting rate confirms the previous two measurements (test periods 20 and 21). In the EPRI MRP-55[11] framework, the SCC CGRs measured in test periods 20, 21, and 28 rank at 25th percentile.

Finally, the crack was advanced in fatigue by a more substantial 0.25 mm [0.0098 in] to a different microstructure, and the known fatigue behavior was reproduced in test period 34. As before, this test period was followed by two minimal transitioning test periods, and constant load in test period 37 (Fig. 43p). SCC growth under constant load was well-behaved, and the system resolution was better than 0.3 μm. Overall, growth rate in test period 37 was observed to diminish over time, but the average SCC CGR for this test period (5.4×10^{-11} m/s) ranks at the 90th percentile in the EPRI MRP-55[11] framework. For the final test period, the specimen was fatigued in the environment. Very fast growth was observed initially, then the rate settled at the expected fatigue CGR, Fig. 43q. The crack extent at which the fatigue CGR stabilizes is indicated by the blue arrow in the figure. If this additional growth is taken into account, the resulting SCC rate in test period 37 is closer to the 95% percentile rank.

Next, the system was brought to room temperature, drained, and the specimen was fatigued apart for the examination of the fracture surface.

Table 3. Crack growth data for Alloy 600 heat M7929 specimen DB-3 (DB600-CR-3) in PWR water[a].

Test Period	Test Time, h	Temp. °C	Load Ratio R	Rise Time, s	Down Time, s	Hold Time, S	K_{max}, MPa·m$^{1/2}$	ΔK, MPa·m$^{1/2}$	CGR_{env}, m/s	Estimated CGR_{air}, m/s	Crack Length, mm
Pre a	81	320.7	0.20	0.25	0.25		14.1	11.3	8.27E-09	1.12E-08	6.087
Pre b	105	320.6	0.20	0.25	0.25		14.2	11.3	1.09E-08	1.13E-08	6.135
Pre c	107	320.5	0.30	0.5	0.5		14.2	9.9	5.81E-09	4.15E-09	6.147
Pre d	109	320.5	0.30	1	1		14.3	10.0	2.23E-09	2.15E-09	6.161
Pre e	122	320.4	0.30	50	50		14.4	10.1	9.62E-11	4.39E-11	6.163
Pre f	123	320.4	0.30	1	1		14.4	10.1	2.32E-09	2.21E-09	6.168
1	171	320.5	0.50	300	12		14.4	7.2	1.18E-11	3.18E-12	6.170
2	177	320.4	0.50	30	4		14.5	7.2	5.40E-11	3.25E-11	6.171
3	194	320.4	0.50	300	4		14.4	7.2	1.61E-11	3.19E-12	6.172
4	283	320.3	1.00	0	0		12.6	0.0	2.53E-12	-	6.174
5	289	320.4	0.24	0.25	0.25		14.7	11.2	9.00E-09	1.18E-08	6.251
6	310	320.3	0.50	30	4		14.6	8.8	1.21E-10	5.32E-11	6.271
7	328	320.2	0.50	300	4		14.6	9.4	3.52E-11	6.25E-12	6.272
8	449	319.9	1.00	0	0		14.8	0.0	2.04E-11	-	6.287
9	599	319.4	1.00	0	0		15.0	0.0	1.89E-11	-	6.299
10	711	319.2	1.00	0	0		15.0	0.0	2.20E-11	-	6.307
11	765	319.5	0.28	2	2		16.9	12.2	6.41E-09	2.26E-09	6.412
12	785	319.6	0.46	60	12		17.2	9.3	1.47E-10	3.92E-11	6.419
13	791	319.6	0.46	80	12		18.9	10.2	3.76E-10	4.39E-11	6.428
14	808	321.2	0.46	600	12		19.0	10.3	1.27E-10	6.02E-12	6.430
15	811	321.2	0.29	2	2		17.9	12.7	5.05E-09	2.77E-09	6.448
16	884	320.2	1.00	0	0		19.1	0.0	1.90E-11	-	6.453
17	886	321.2	0.30	0.5	0.5		18.3	12.8	7.42E-09	1.18E-08	6.492
18	904	320.2	0.50	60	60	3600	19.5	9.7	2.32E-11	8.96E-13	6.495
19	910	320.7	0.30	0.5	0.5		18.6	13.0	7.18E-09	1.27E-08	6.540
20	1,092	320.2	0.50	12	12	3600	19.7	9.8	6.96E-12	9.37E-13	6.549
21	1,406	320.3	1.00	0	0		20.6	0.0	8.84E-12	-	6.552
22	1,412	320.6	0.30	0.5	0.5		19.1	13.4	2.61E-09	1.40E-08	6.583
23	1,414	321.0	0.20	0.5	0.5		19.0	15.2	6.07E-09	1.88E-08	6.616
24	1,435	320.6	0.30	50	12		19.1	13.4	7.14E-11	1.39E-10	6.622
25	1,437	320.7	0.20	0.25	0.25		19.2	15.3	1.23E-08	3.92E-08	6.651
26	1,454	320.5	0.30	50	12		19.3	13.5	1.19E-10	1.46E-10	6.662
27	1,460	320.6	0.30	300	12		19.4	13.6	3.11E-11	2.48E-11	6.663
28	1,623	320.4	1.00	0	0		19.3	0.0	5.65E-12	-	6.667
29	1,630	320.4	0.20	0.25	0.25		18.4	14.7	1.50E-08	3.32E-08	6.783
30	1,646	320.3	0.20	50	50		18.5	14.8	4.22E-10	1.70E-10	6.804
31	1,647	320.5	0.20	0.25	0.25		18.8	15.0	1.92E-08	3.61E-08	6.850
32	1,652	319.8	0.20	0.25	0.25		17.9	14.3	1.63E-08	2.93E-08	6.920
33	1,654	319.4	0.20	50	50		17.9	14.4	2.11E-09	1.48E-10	6.930
34	1,656	319.6	0.20	0.25	0.25		18.3	14.7	2.89E-08	3.24E-08	7.014
35	1,670	319.3	0.20	50	50		18.5	14.8	1.48E-09	1.68E-10	7.045
36	1,672	319.7	0.50	50	12		18.7	9.3	4.04E-10	5.49E-11	7.074
37	2,006	319.0	1.00	0	0		19.4	0.0	7.50E-11	-	7.127
38	2,008	319.0	0.20	1	1		18.9	15.1	8.62E-09	9.09E-09	7.192

[a]Simulated PWR water with 2 ppm Li, 1100 ppm B, and 2 ppm. DO<10 ppb. Conductivity was 21±3 µS/cm, and pH 6.4.

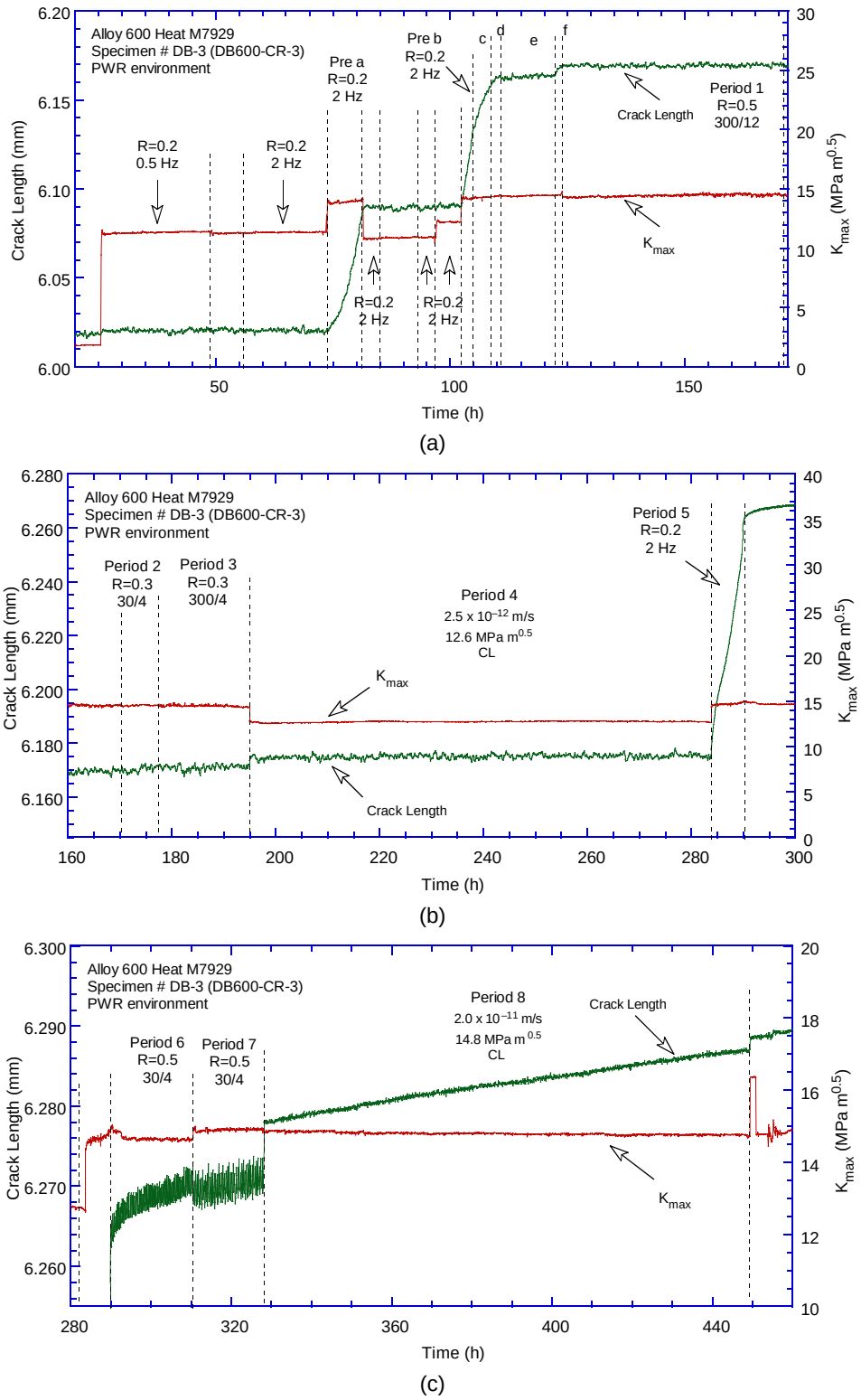

Figure 43. Crack–length–vs.–time for Alloy 600 heat M7929 specimen DB-3 in simulated PWR environment during test periods (a) precracking-1, (b) 2-5, (c) 6-8, (d) 9, (e) 10, (f) 11-15, (g) 16, (h) 17, (i) 18-19, (j) 20, (k) 21, (l) 22, (m) 23-27, (n) 28, (o) 29-36, (p) 37, and (q) 38.

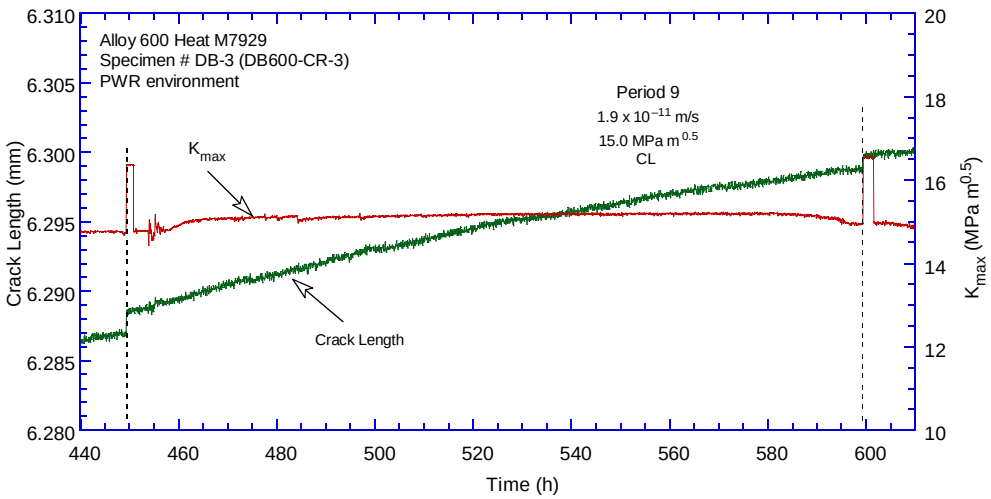

(d)

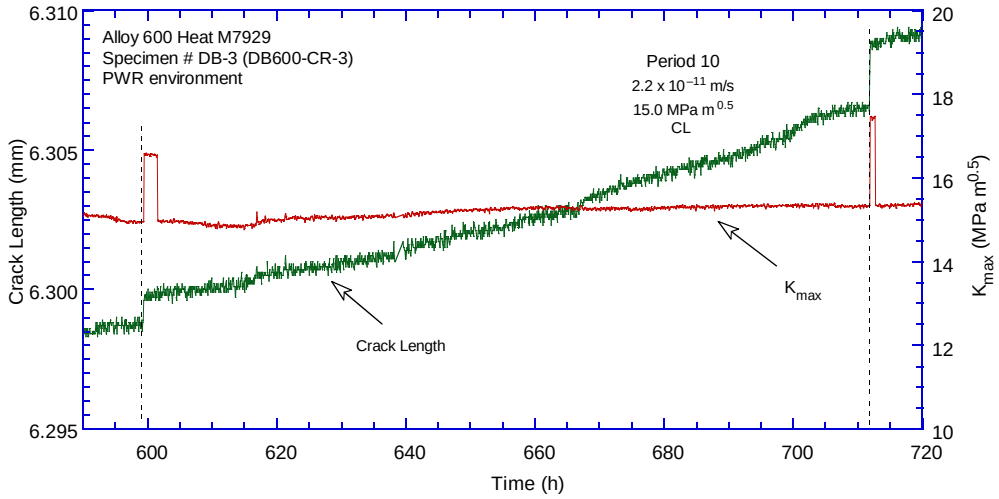

(e)

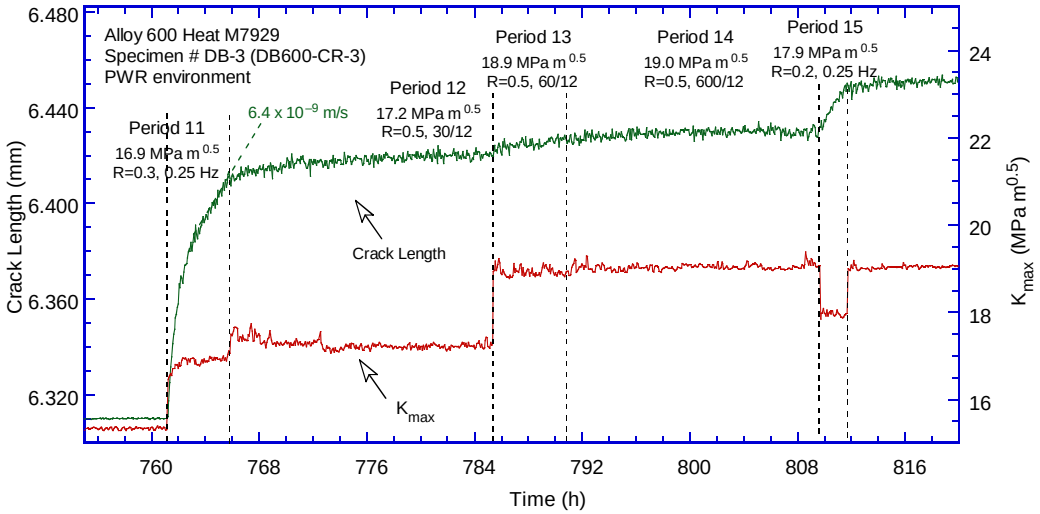

(f)

Figure 43. (Cont.)

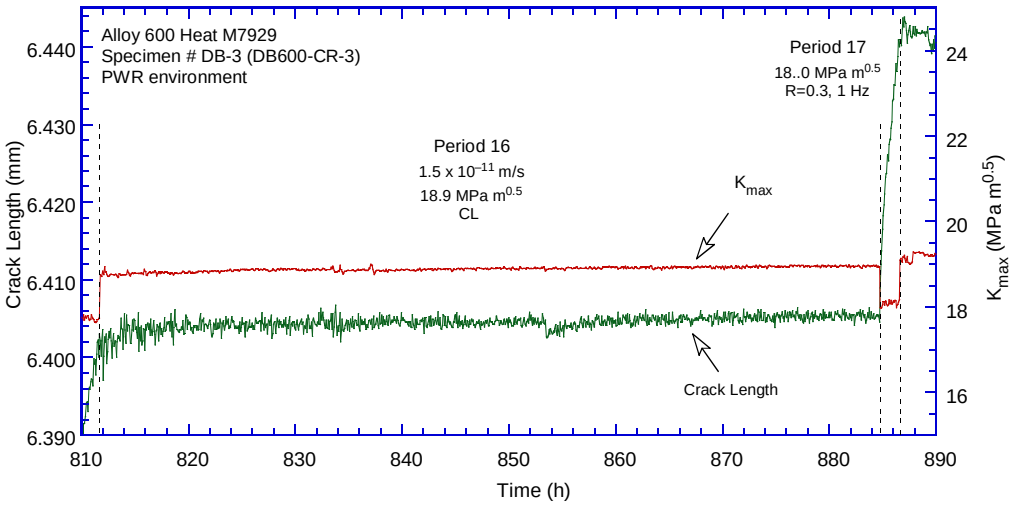

(g)

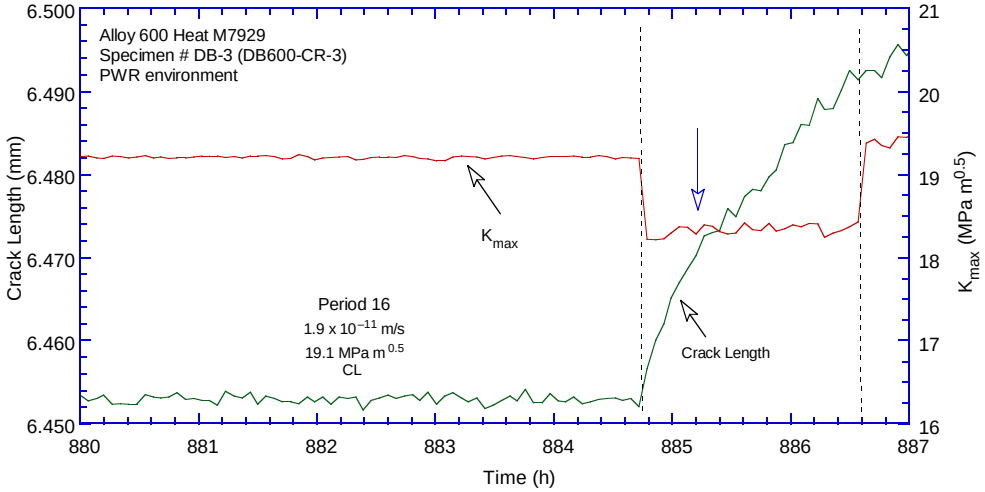

(h)

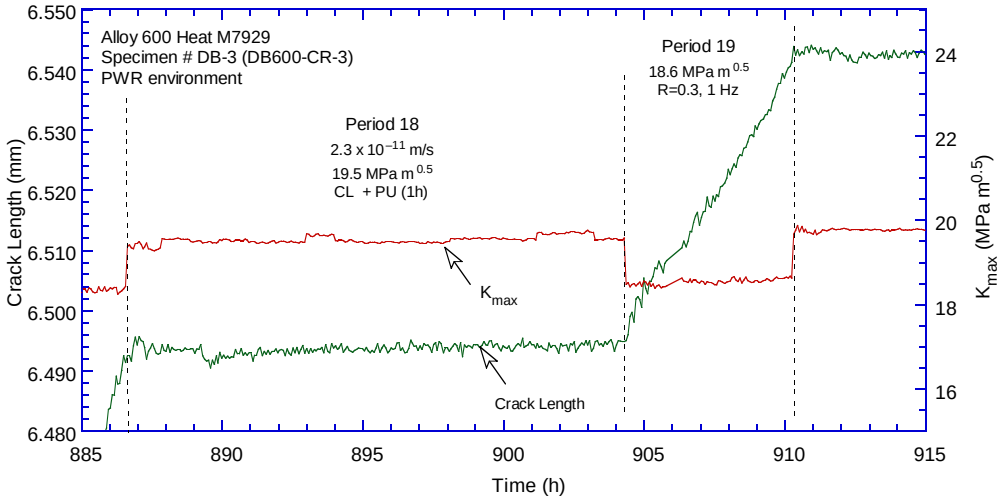

(i)

Figure 43. (Cont.)

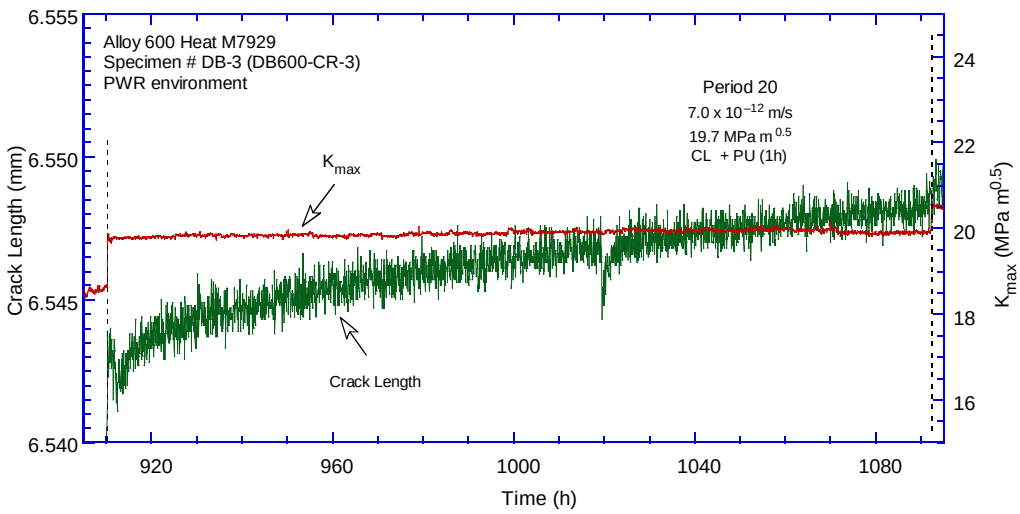

(j)

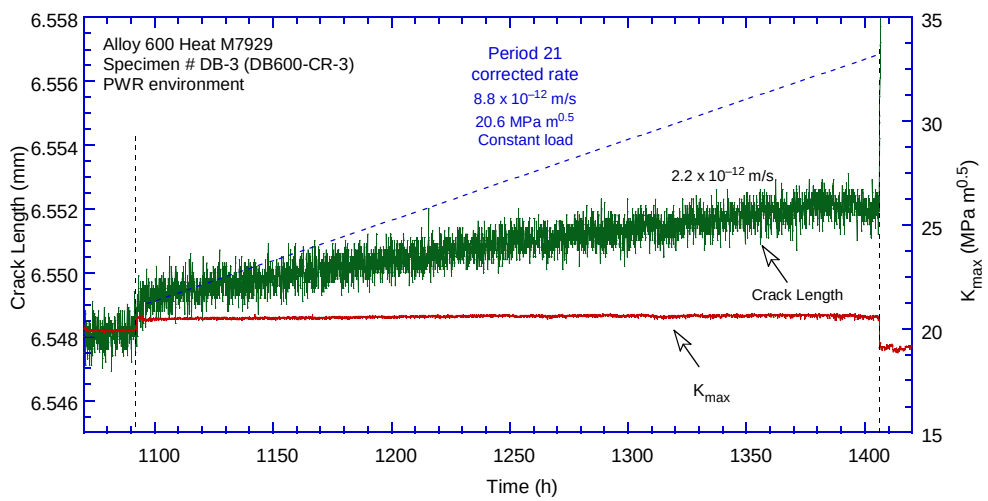

(k)

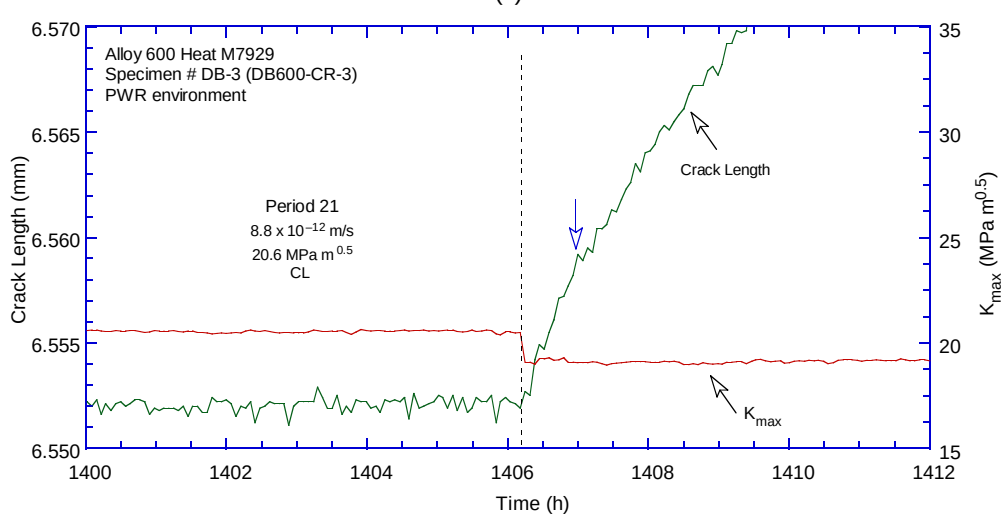

(l)

Figure 43. (Cont.)

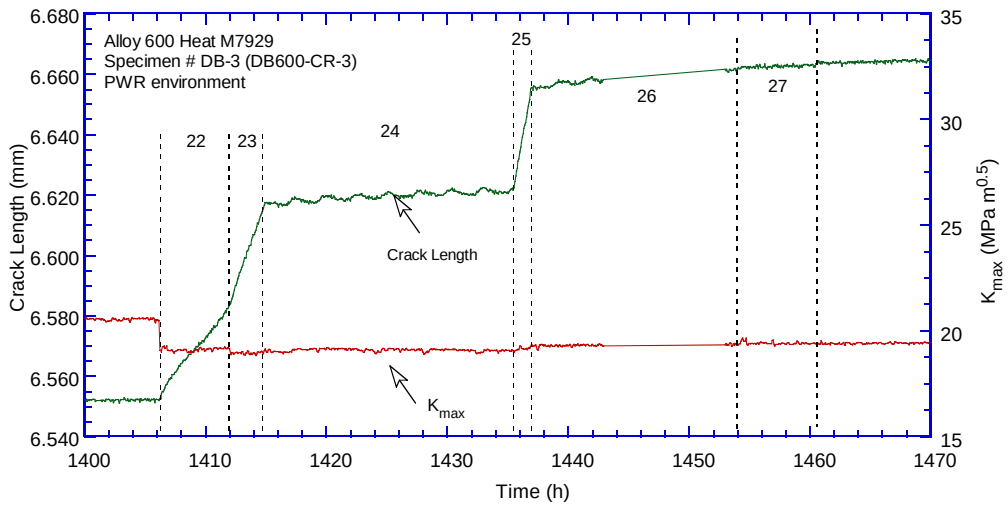

(m)

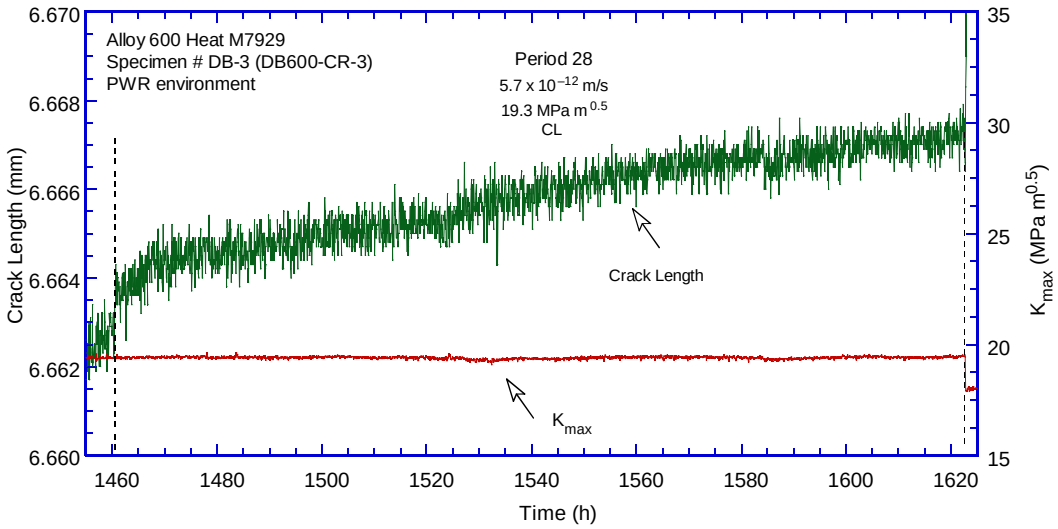

(n)

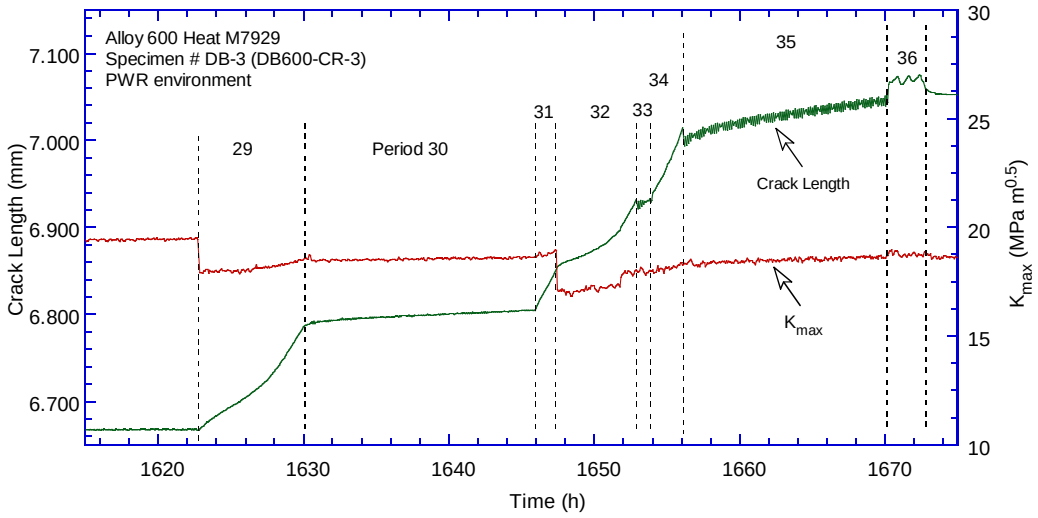

(o)

Figure 43. (Cont.)

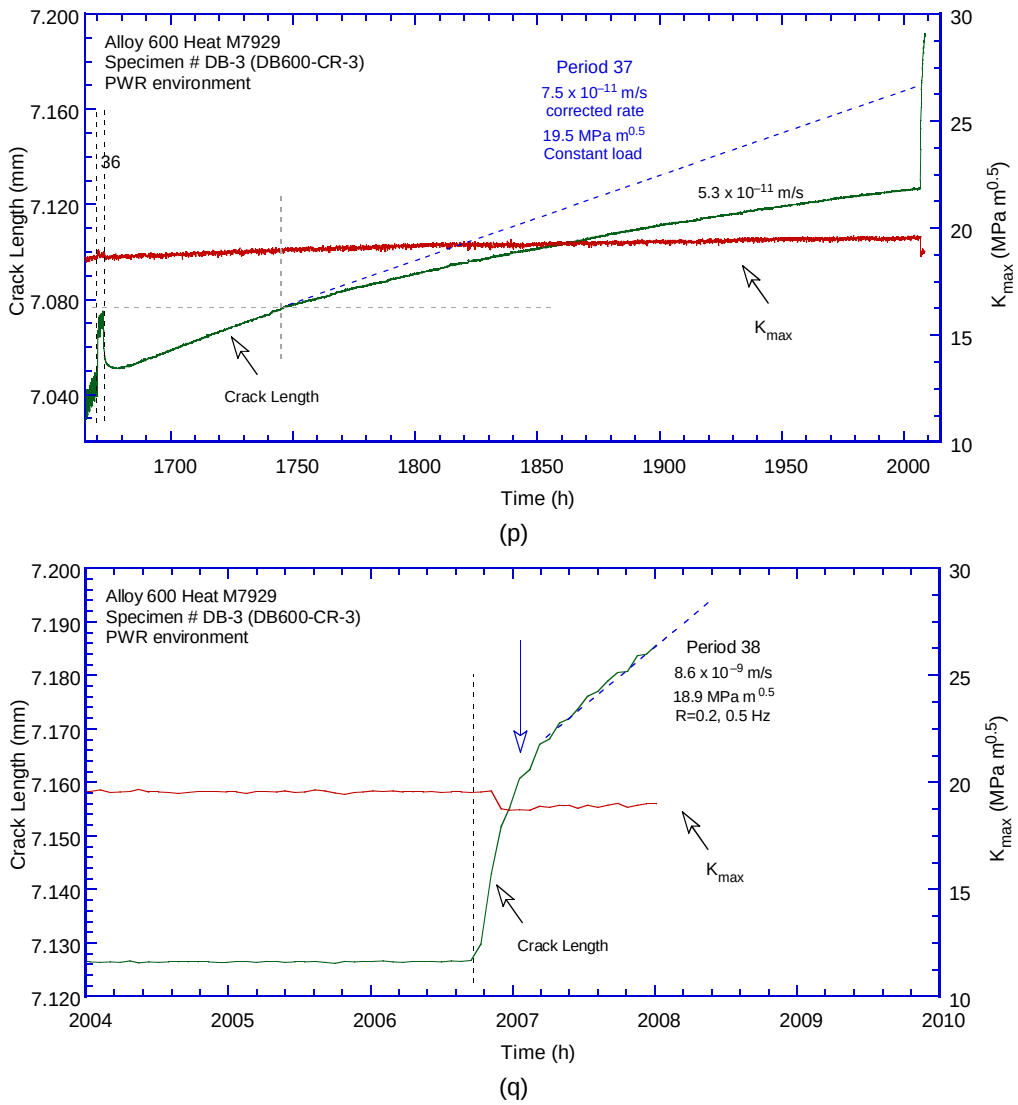

Figure 43. (Cont.)

Figure 44 shows the entire fracture surface of the specimen. Overall, the fracture surface is relatively straight, and, as with the previous two specimens, the fracture mode seems largely IG. Additional detail is provided in Fig. 44. This is a section of the fracture surface showing all stages of the test, from precracking – end, approximately at location A in Fig. 44. Figure 44a shows that the fracture mode was mixed TG-IG during precracking at low stress intensity, and is illustrated at larger magnification in Fig. 44b. The fracture mode changes completely to smooth IG after approximately 0.15-0.2 mm (see region marked IG-1 in Fig. 45a). The fracture mode stays largely IG for the remainder of the test, however, TG features can be observed during crack advance in fatigue in the second part of the test. An example is shown in Fig. 44c taken at location 2 in Fig. 44a. The fracture mode again changes completely to smooth IG towards the end of the test during constant load at the higher stress intensity factor (see region marked IG-2 in Fig. 45a). The fracture mode from this region is shown at higher magnification in Fig. 44d taken at location 3 in Fig. 44a. In summary, while the fracture mode appears largely IG, a complete IG fracture mode was apparently obtained only under constant load conditions. During the fatigue regions, a mixed mode was observed, and the amount of IG appears to increase with the stress intensity factor that was applied.

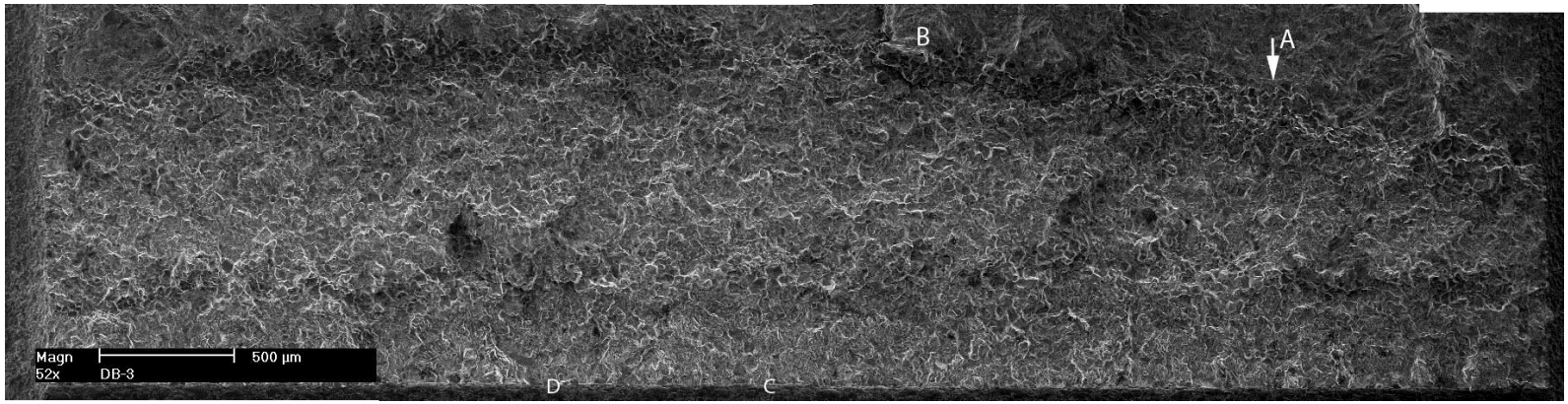

Figure 44. Fracture surface of specimen DB-3. Crack advance is from bottom to top.

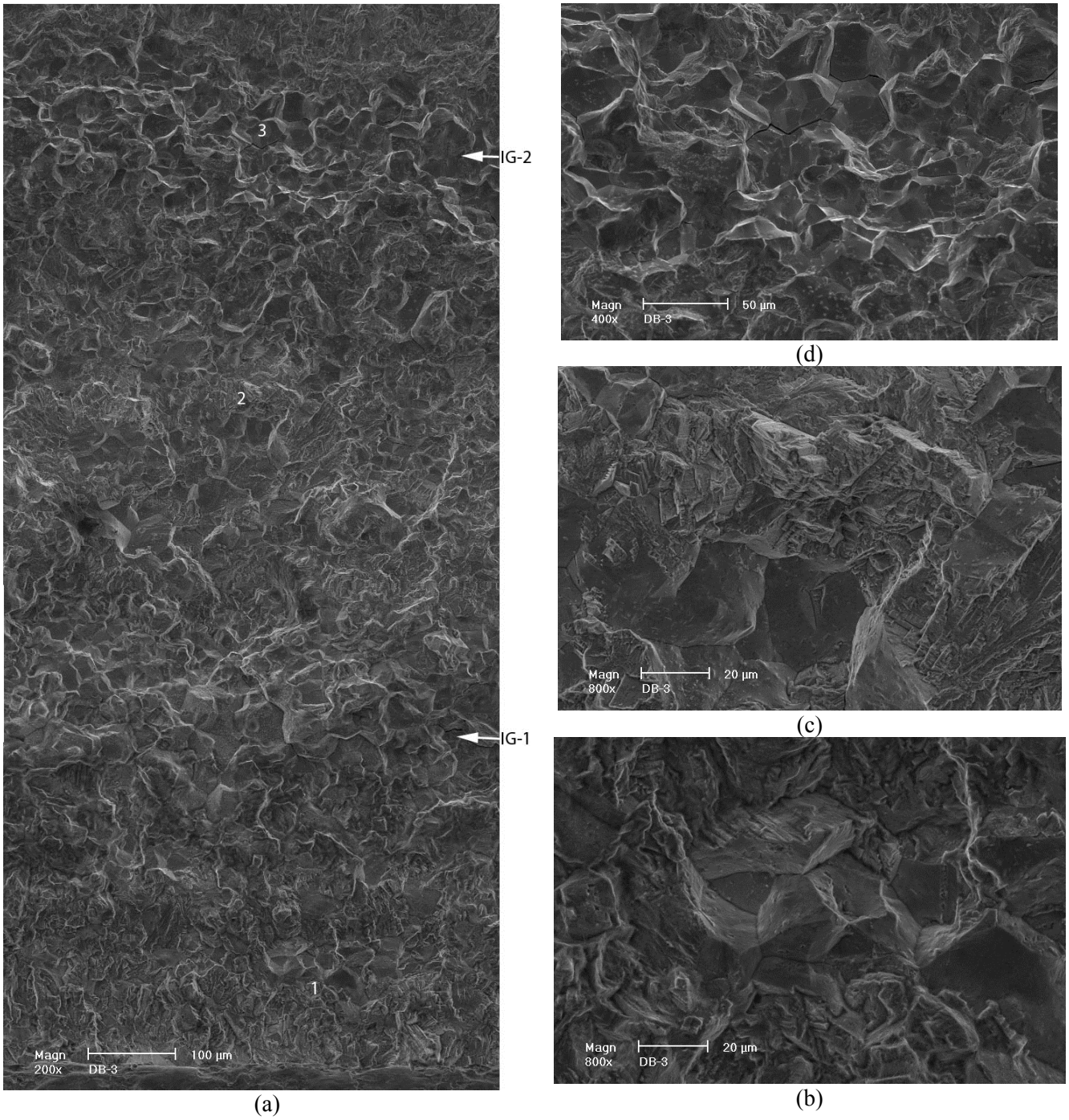

Figure 45. (a) Section of the fracture surface of Specimen DB-3 at location A in Fig. , (b) mixed TG-IG fracture mode at location 1, (b) mixed TG-IG fracture mode at location 2, and (c) intergranular fracture mode at location 3. Crack advance is from bottom to top.

As with the previous two specimens, crack branching and ligaments were also observed on the fracture surface of this specimen. Examples of out of plane cracking and crack branching and/or ligaments are shown in Fig. 46. These pictures were obtained at the approximate location B in Fig. 44. The secondary cracks/ligaments shown here are not as extensive as those observed on the previous two specimens, and validate the experimental approach used in this test. The location of those cracks suggests they most likely developed during the last test period at constant load, thus, had effect on the crack growth rate measured by DC potential.

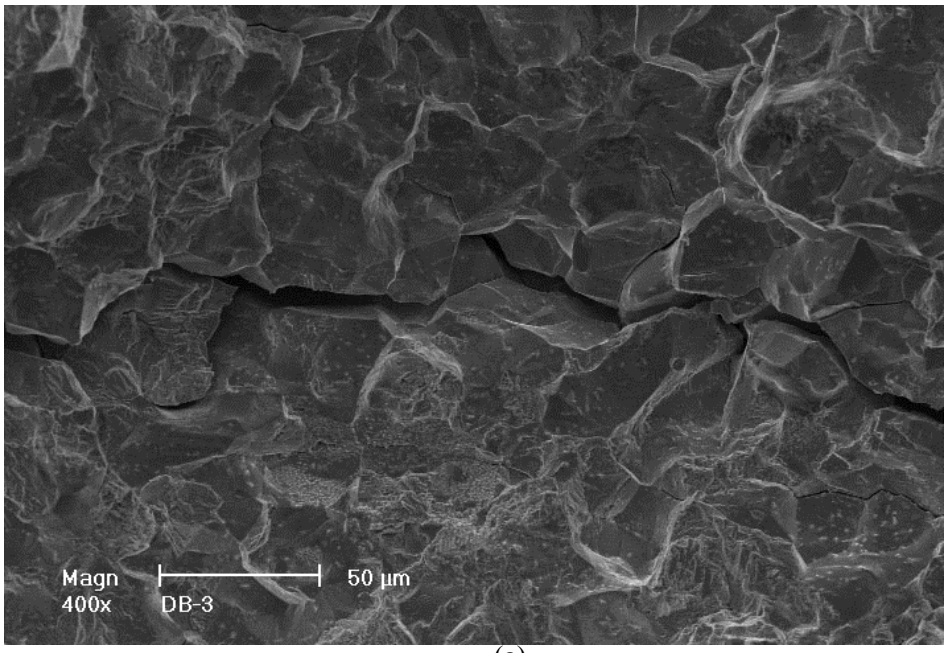

(a)

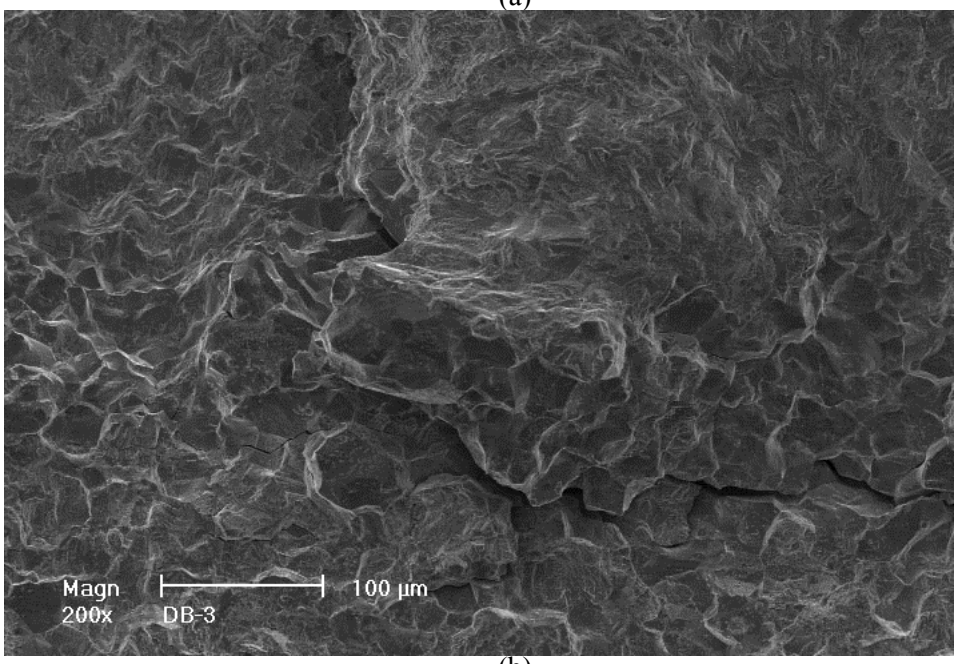

(b)

Figure 46. Fracture surface of specimen DB-3 (location B in Fig. 44): (a) secondary cracks/crack and (b) ligament. Crack advance is from bottom to top.

A feature of interest that was highlighted in the two previous tests as well, is the IG fracture mode that occurred during precracking in water. As mentioned previously in this report, this feature is atypical and was observed only in the two companion specimens from the Davis-Besse replacement reactor pressure vessel head nozzle #4 (Alloy 600 heat M7929) and the nozzle #3 (Alloy 600 heat M3935) obtained from the original Davis-Besse reactor pressure vessel head that was tested at ANL previously.[9] Two additional images from the notch area (locations C and D in Fig.44) are shown in Fig. 47, and select instances of smooth IG cracking are indicated by arrows in each picture. While there is a substantial presence of IG cracking, it is not as extensive as in the other two specimens. However, specimen DB-3 was precracked at a lower stress intensity factor than specimens DB-4 and DB-5. As such, there appears that in this particular alloy, the stress intensity factor affects the fracture mode during fatigue crack propagation. Nevertheless, the presence of IG cracking under fatigue conditions is remarkable.

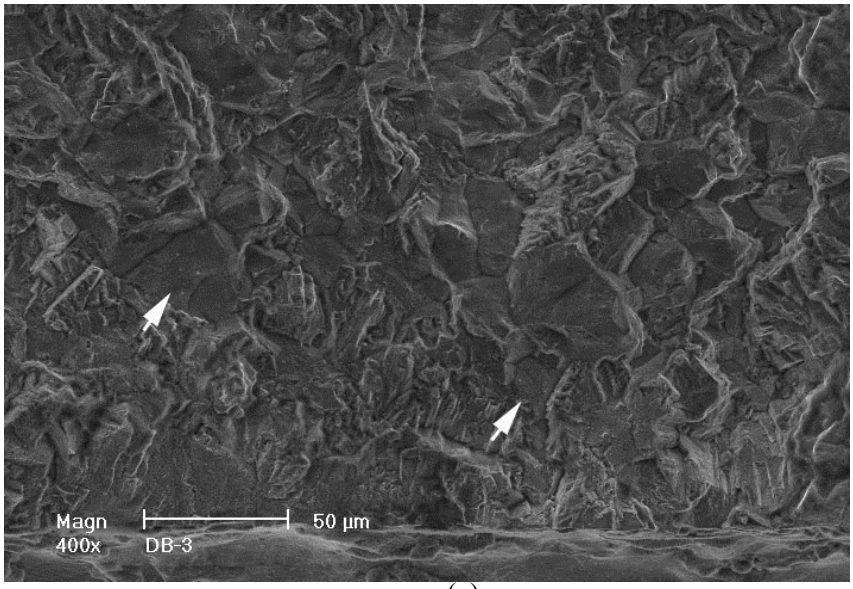

(a)

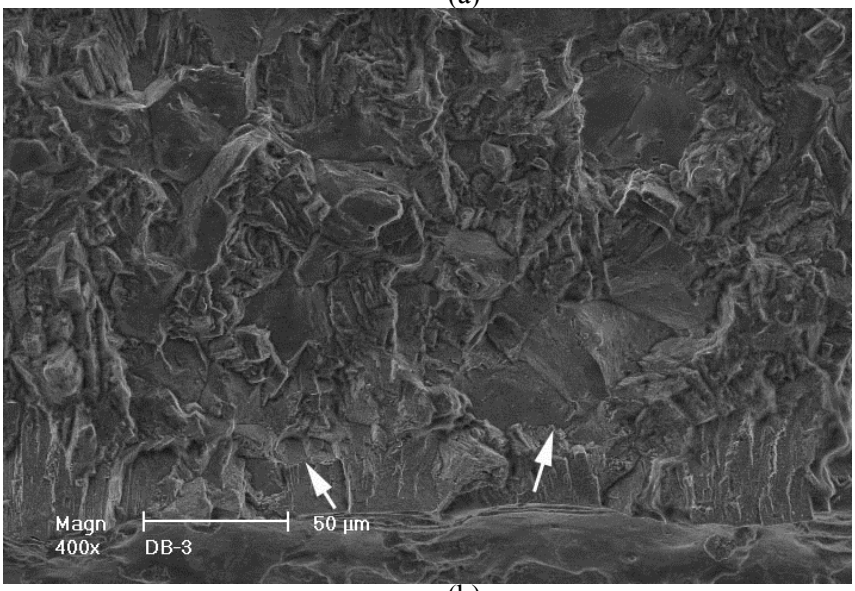

(b)

Figure 47. Fracture surface of specimen DB-3 during precracking. Select instances of smooth IG is shown with arrows. Crack advance is from bottom to top.

5. Discussion

The section summarizes the cyclic and SCC CGR results obtained on the replacement Davis-Besse CRDM nozzle #4 material, and compares them with the similar data obtained previously on the original nozzle #3 material. The SCC CGR data are discussed in the context of the disposition curves proposed by industry.

5.1. Cyclic CGRs

Figure 48 summarizes the cyclic CGR data for the three specimens obtained from nozzle #4 of the replacement Davis-Besse reactor pressure vessel head (heat M7929). The corrosion fatigue curve for generic Alloy 600 (Eq. 4, green) is included for comparison. The data from the first two specimens DB-4 and DB-5, Fig. 48a, for which precracking was initiated at approximately 21 MPa $m^{1/2}$ [19.1 ksi $in^{1/2}$] reproduce the known fatigue behavior for Alloy 600, and show substantial environmental enhancement. Both specimens exhibited IG fracture during precracking. The data set for specimen DB-3, Fig. 48b, for which precracking was initiated at approximately 14 MPa $m^{1/2}$ [12.7 ksi $in^{1/2}$] also reproduces the known fatigue behavior for this alloy, however, the initial environmental enhancement is less than expected (see the open sumbols in Fig. 48b). This behavior is reflected on the fracture surface in a much lower proportion of IG cracking (Fig. 45a,b), and may be due to the lower stress intensity factor at which the test was initiated. Nevertheless, as the stress intensity factor was increased to ≈17-19 MPa $m^{1/2}$ [15.5-17.3 ksi $in^{1/2}$], environmental enhancement increased (see the open sumbols in Fig. 48b), and this again is reflected in the higher proportion of IG cracking observed on the fracture surface in the second part of the test (Fig. 45a,c). In summary, the environmental degree of environmental enhancement seems to correlate well with the degree of IG cracking which, in turn, correlates well with the applied stress intensity factor. However, as mentioned previously, the presence of IG cracking under fatigue conditions is by itself remarkable.

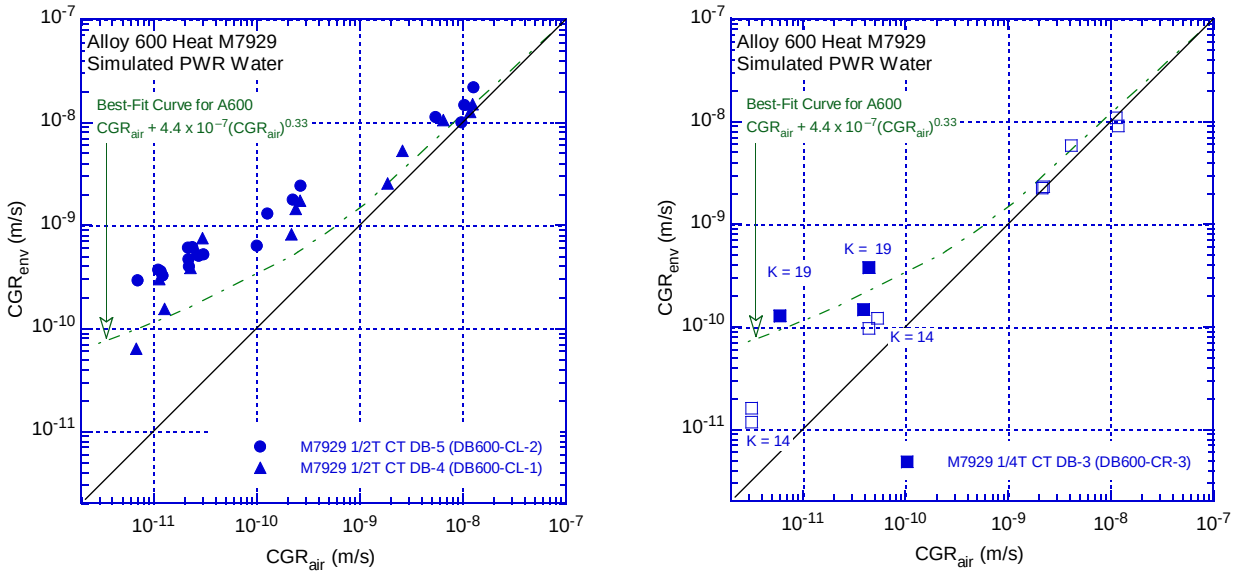

(a) (b)

Figure 48. Cyclic CGR data for Alloy 600 (heat M7929) specimens (a) DB-4, DB-5, and (b) DB-3.

Figure 49 shows the cyclic data for the DB-4 and DB-5 specimens obtained from nozzle #4 of the replacement Davis-Besse reactor pressure vessel head (heat M7929) as well as data obtained previously on the original Davis-Besse reactor pressure vessel head nozzle #3 (heat M3935) alloy. The corrosion fatigue curve for generic Alloy 600 (Eq. 4, green) is included for comparison. Also included is the corrosion fatigue curve calculated from Davis-Besse nozzle #3 (heat M3935) data exclusively (Eq. 5, red). Both heats, M3935 and M7926 show substantial environmental enhancement, yielding higher values than expected for typical Alloy 600. Also, both heats exhibited an IG fracture mode during precracking. Hence, the similarity between the data sets was to be expected.

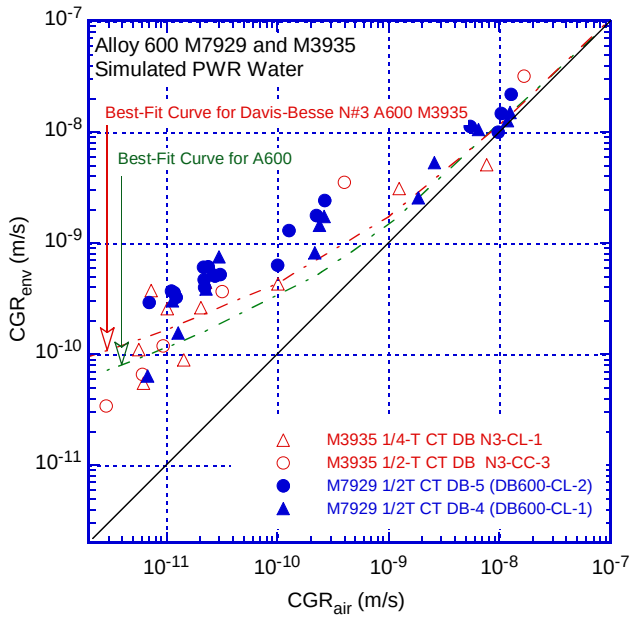

Figure 49.
Cyclic CGRs for Alloy 600 (heat M7929) specimens DB-4 and DB-5 from nozzle #4 of the Davis-Besse replacement reactor pressure vessel head (blue symbols) in simulated PWR environment. Data for Alloy 600 (heat M3935) from the original Davis-Besse reactor pressure vessel head nozzle #3[9] (red symbols), and corrosion fatigue curves for generic Alloy 600 (Eq. 4, green curve) and nozzle #3 (Eq. 5, red curve) are included.

5.2. SCC CGRs

Figure 50 summarizes the SCC CGR data obtained for the Alloy 600 heat M7929 specimens. For comparison, and the EPRI MRP-55 curves[11] for the 25th-95th percentile range. The SCC CGRs were normalized to 325°C [617°F] using an activation energy of 130 kJ/mol [31 kcal/mol].[11] The figure includes SCC CGR data generated both at constant load (open symbols) and at constant load with periodic unloading (solid symbols). Both loading types are acceptable in the framework of EPRI MRP-55[11], and both have been used to generate the EPRI MRP-55[11] database. Only data resulting from test periods where growth was at least 10 times the resolution were considered statistically significant and included in the plot. As expected, the figure shows that the data obtained at constant load are consistent with data obtained with some form of cyclic loading. Specimens DB-5 and DB-4 were 1/2T CTs and allowed[13,14] for testing at moderate (≈23-25 MPa m$^{1/2}$ [20.9-22.8 ksi in$^{1/2}$]) to high (≈27-30 MPa m$^{1/2}$ [24.6-27.3 ksi in$^{1/2}$]) stress intensity factors. In the modertate range, the SCC CGR data resulting from the specimen DB-5 rank rather consistently at approximately 75th percentile susceptibility. The lone data point in this stress intensity range from specimen DB-4 supports the DB-5 observations. In the high stress intensity range, there seems to be a cluster of SCC CGR data from both specimens at approximately the 75th percentile, but also lower (primarily DB-4) and higher (primarily DB-5). However, the data obtained from successive test periods seems to be more consistent with each other that that obtained from different locations within the sample. As such, there appears that the local microstructure affects the resulting CGR. A very similar microstructural effect was observed on specimen DB-3. This specimen was a 1/4T CT and allowed[13,14] for testing at a stress intensity factor up to approximately 20 MPa m$^{1/2}$ [18.2 ksi in$^{1/2}$]). Hence, this test was initiated at a stress intensity factor of approximately 15 MPa m$^{1/2}$

[13.6 ksi in$^{1/2}$], and a set of three consective SCC CGR measurements produced very consistent data ranking at the 75th percentile susceptibility. A short distance away (≈ 0.25 mm), another three successive test periods conducted at stress intensity factors in the (≈19-21 MPa m$^{1/2}$ [17.3-19.1 ksi in$^{1/2}$]) produced consistent SCC CGR rates ranking at the 25th percentile. After an additional ≈ 0.25 mm, the final test period of that test conducted at a similar stress intensity factor of 19.4 MPa m$^{1/2}$ [17.6 ksi in$^{1/2}$] produced an SCC CGR ranking above the 90th percentile. In summary, the SCC CGR dependence on the local microstructure observed on specimen DB-4 is consistent with the observations made on the other two specimens. Overall, the SCC CGRs for Alloy 600 heat M7929 appear to rank at the 75th percentile (EPRI MRP-55[11] proposed disposition curve), however, some microstructures can yield SCC CGRs at or above the 90th percentile rank.

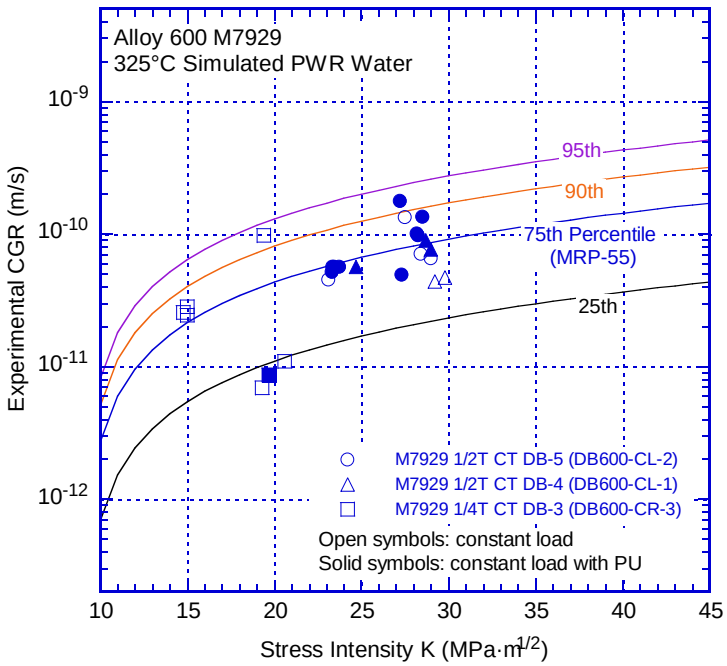

Figure. 50.
SCC CGR data for Alloy 600 heat M7929 from the Davis-Besse replacement reactor pressure vessel head The EPRI MRP-55[11] curves for 25th-95thpercentile are also shown.

Figure 51 compares the SCC CGR data for the Alloy 600 heat M7929 to those obtained previously for Alloy 600 from the DB nozzle #3 (alloy 600 heat M3935).[9] As described previously, most of the SCC CGRs for Alloy 600 heat M7929 appear to rank at the 75th percentile (EPRI MRP-55[11] proposed disposition curve), however, some microstructures were seen to yield SCC CGRs at the 90th percentile rank. While the Alloy 600 heat was found to produce rates in excess of the 95th percentile curve, both alloys appear to be relatively highly susceptible to SCC. It is also important to note, that the crack plane orientation (C-L vs. C-R, Fig. 6) does not seem to play a significant role in either alloy.

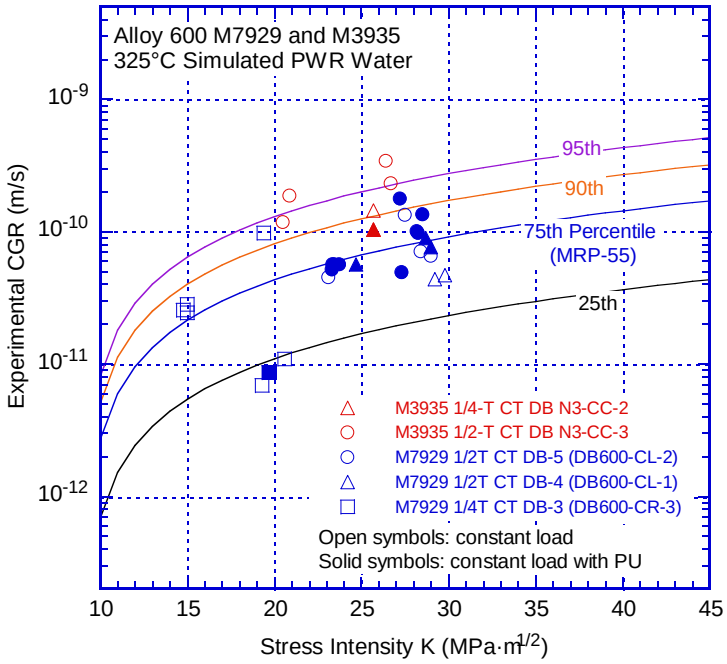

Figure. 51.
SCC CGR data for Alloy 600 heat M7929 from the Davis-Besse replacement reactor pressure vessel head and for Alloy 600 heat M3935 from nozzle #3 in the the original Davis-Besse reactor pressure vessel head.[9] The EPRI MRP-55[11] curves for 25th-95th percentile are also shown.

5.3. Microstructural Analysis

One of the observations in these tests was the IG fracture mode observed during precracking. As an illustration, Fig. 52 provides a side-by-side comparison between DB-5 from the replacement alloy (heat M7929) (Figs. 52a, b) and a Davis-Besse nozzle #3 (heat M3935) specimen (Fig. 52c). The appearance of the two fracture surfaces is very similar: the fracture mode turns IG either at the specimen notch or at one of the very first grain boundaries encountered. It is also important to note that the two alloys have very different microstructures, as illustrated in the side-by-side comparison shown in Fig. 53. While the M3935 heat had a microstructure consisting of equiaxed grains with adequate grain boundary carbide decoration, the M7929 heat used in the replacement reactor pressure vessel head apparently has a largely carbide-free grain boundary network. The carbides decorate what seem to be the ghost boundaries of a prior network. In short, these two field alloys have different microstructures, yet they display atypical but similar behavior in primary water. It is not clear why these alloys display IG cracking during fatigue precracking in water, but the feature suggests that the grain boundaries in both alloys have greater than average susceptibility to IG cracking.

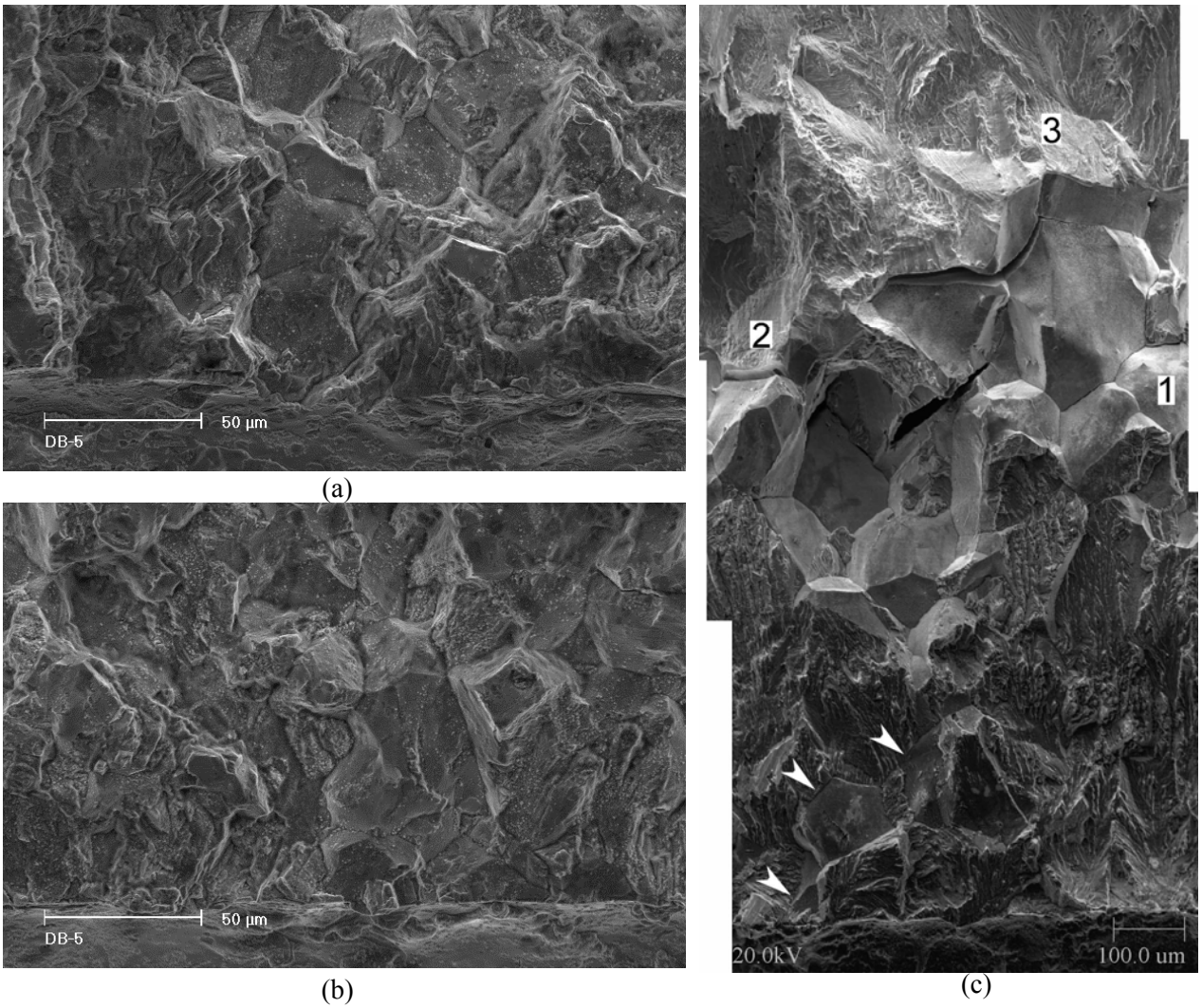

Figure 52. Area near the specimen notch in Alloy 600 heat M7929 Specimen DB-5 (a and b) and Alloy 600 heat M3935 N#3 specimen N3CC-3 (c). Crack advance is from bottom to top.

While the seemingly large difference in microstructure did not seem to affect the rate of SCC propagation in the two alloys in a significant manner, it is plausible that the resistance to SCC initiation may have been affected. In the framework of a mechanism for induction of IG SCC by grain-boundary sliding,[25] one can envision that those factors that significantly affect grain boundary sliding (such as grain boundary carbides) also affect SCC initiation. As such, based on the difference in microstructure only, the replacement alloy 600 heat M7929 used in CRDM nozzle #4 in the replacement head appears significantly more susceptible to SCC than the previously tested nozzle #3 (Alloy 600 heat M3935) material due to the lack of grain boundary carbides.

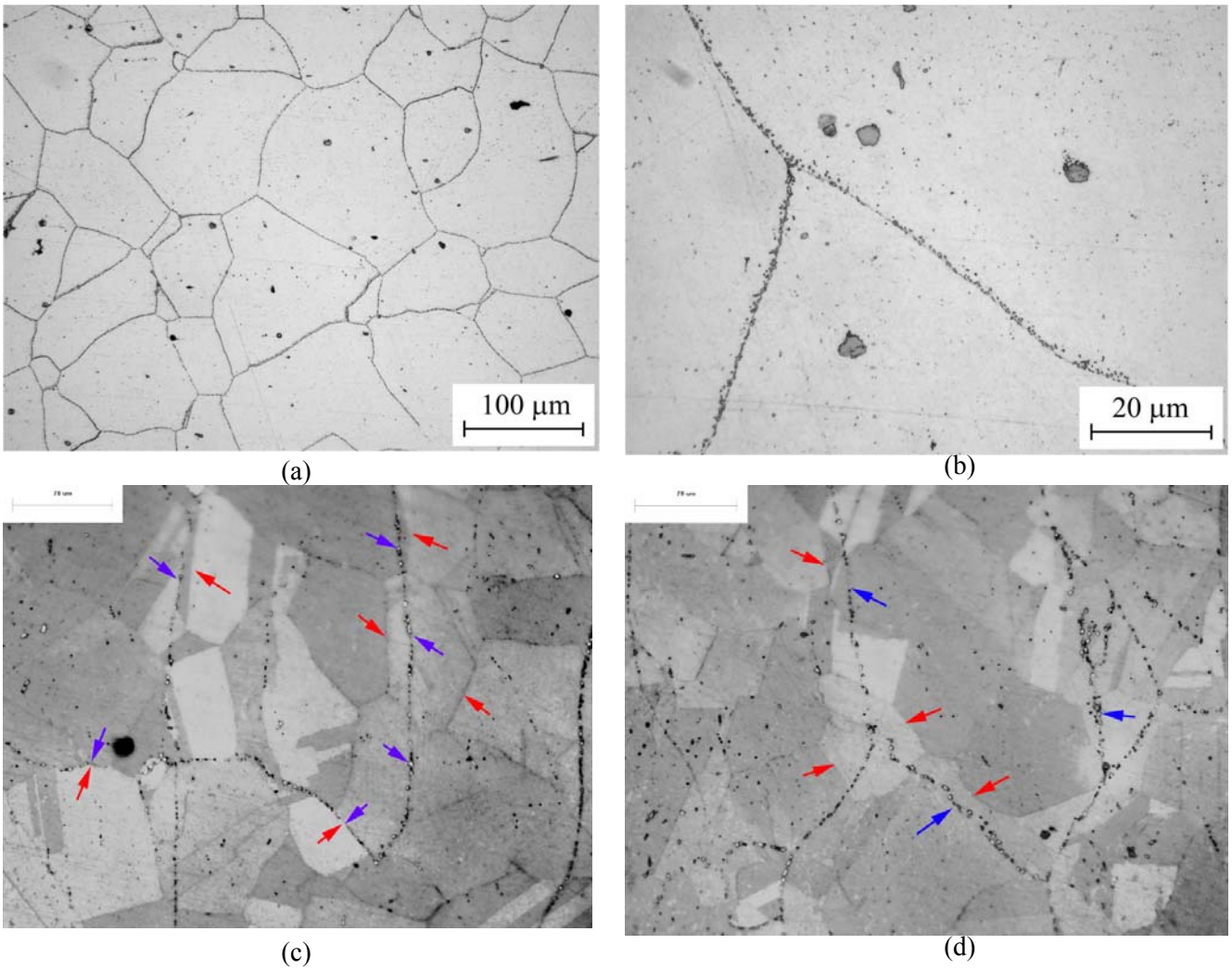

Figure 53. Microstructure of the original Davis-Besse reactor pressure vessel head nozzle#3 alloy 600 heat M3935 (a and b) and the alloy 600 sample obtained from nozzle #4 of the replacement Davis-Besse reactor pressure vessel head heat M7929 (c and d). Red arrows indicate grain boundaries and blue arrows indicate carbides. For images c and d, scale bars are 50 µm and 20 µm, respectively.

5.4. Activation Energy for SCC Growth

Figure 54 shows the SCC CGR data vs. temperature for specimens DB-5 and DB-4 (alloy 600 heat M7929). The SCC CGRs were measured at 350°C [662°F] and 325°C [617°F] on specimen DB-5, and at 320°C [608°F] and 290°C [554°F]on specimen DB-4. The CGRs were normalized to a common stress intensity factor (27 MPa $m^{1/2}$[26 ksi $in^{1/2}$]) using Eq. 6. The activation energy for SCC growth in the replacement DB alloy was calculated to be 145 kJ/mol [35 kcal/mol] from the best-fit curve in Fig. 54, which is consistent with the activation energy of typical Alloy 600 calculated in EPRI MRP-55 (130 kJ/mol [31 kcal/mol]).[11]

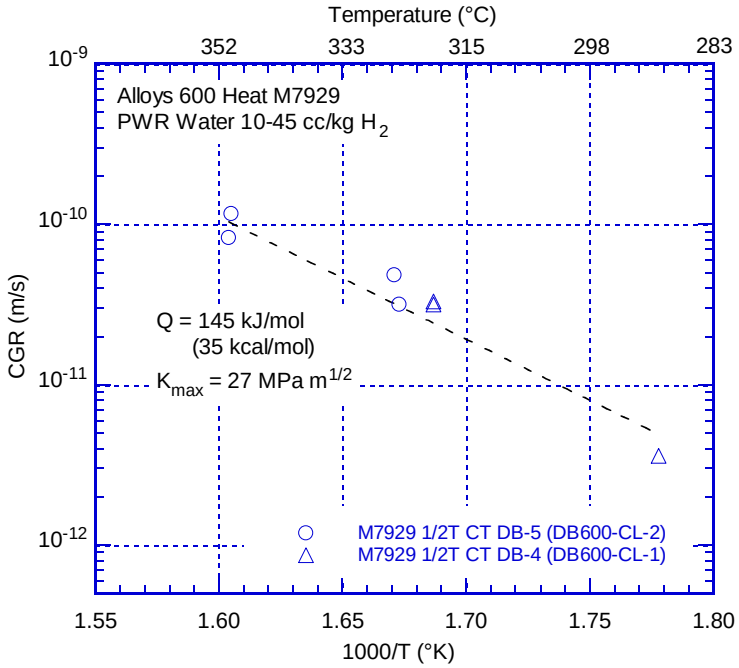

Figure. 54.
SCC CGR vs. temperature for the Alloy 600 (heat M7929) specimens DB-5 and DB-4 tested in PWR environment.

6 Conclusion

Cyclic and SCC CGRs have been measured under several loading conditions on three samples cut from the replacement Davis-Besse CRDM nozzle #4 in two orientations. Following testing in the PWR environment, the cross sections and fracture surfaces were examined. The findings can be summarized as follows:

1) The mechanical fatigue behavior of the replacement Davis-Besse alloy appears similar to that of typical Alloy 600. The environmental enhancement of cyclic rates is higher than that expected for typical Alloy 600. The corrosion fatigue behavior appears to be similar to that for samples extracted from nozzle #3 in the original Davis-Besse reactor pressure vessel head (Alloy 600 heat M3935).

2) Most of the SCC CGRs for the samples extracted from nozzle #4 (Alloy 600 heat M7929) in the Davis-Besse replacement reactor pressure vessel head appear to be at the 75th percentile (EPRI MRP-55[11] proposed disposition curve); however, some microstructures can yield SCC CGRs at the 90th percentile. The crack propagation direction (circumferential-longitudinal vs. circumferential-radial) does not seem to affect the measured CGRs.

3) The activation energy for SCC growth in the samples extracted from nozzle #4 (Alloy 600 heat M7929) in the Davis-Besse replacement reactor pressure vessel head appears similar to that of typical Alloy 600.

4) The examination of the cross section and fracture surface of both specimens revealed that the IG cracking was extensive. Secondary cracks, crack branching, and ligaments were observed.

5) The fracture surface revealed IG cracking under fatigue precracking in primary water. This behavior is unexpected for typical Alloy 600, but was observed in samples extracted from nozzle #3 (Alloy 600 heat M3935) in the original Davis-Besse reactor pressure vessel head specimens tested previously. This behavior suggests an increased susceptibility of the grain boundaries to IG cracking.

6) The microstructure of the samples extracted from nozzle #4 (Alloy 600 heat M7929) in the Davis-Besse replacement reactor pressure vessel head was examined. It was found that these samples had a largely carbide-free grain boundary network. The carbides decorate what seem to be the ghost boundaries of a prior network. By contrast, the nozzle #3 (Alloy 600 heat M3935) extracted from the original Davis-Besse reactor pressure vessel head had an adequate grain boundary carbide decoration. Based on the difference in microstructure only, due to the lack of grain boundary carbides, the M7929 heat in nozzle #4 of the Davis-Besse replacement reactor pressure vessel head appears more susceptible to SCC than the Alloy 600 heat M3935 removed from nozzle #3 in the original Davis-Besse reactor pressure vessel head. However, the seemingly large difference in microstructure did not seem to affect the rate of SCC propagation in the two alloys in a significant manner.

Aknowledgments

The authors thank E. Listwan for his contributions to the experimental effort. This work was sponsored by the Office of Nuclear Regulatory Research, U.S. Nuclear Regulatory Commission, under Job Code V6137, Program Manager Darrell Dunn.

References

1. U.S. NRC Generic Letter 97-01, "Degradation of Control Rod Drive Mechanism and Other Vessel Closure Head Penetrations," April 1, 1997.

2. Economou, J., A. Assice, F. Cattant, J. Salin, and M. Stindel, "NDE and Metallurgical Examination of Vessel Head Penetrations," 3rd Intl. Symp. of Fontevraud, Sept. 12–16, 1994.

3. Robinson, M. R., Duke Power Company, "Oconee Unit 1 and Unit 3 Reactor Vessel Head Leakage, Cracking of RV Head Penetrations due to Primary Water Stress Corrosion Cracking," NRC Meeting with the NEI EPRI Material Reliability Program Regarding CRDM Nozzle Crackling Issues, Rockville, MD, April 12, 2001.

4. Frye, C. R., T. Alley, M. L. Arey, Jr., and M. R. Robinson, "Cracking in Alloy 600/182 Reactor Vessel Head Penetrations," PVP–Vol. 437, Service Experience and Failure Assessment Applications ASME 2002, P. S. Lam, ed., American Society of Mechanical Engineers, New York, pp. 171–178, 2002.

5. U.S. NRC Information Notice 2001–05, "Through–Wall Circumferential Cracking of Reactor Pressure Vessel Head Control Rod Driver Mechanism Penetration Nozzle at Oconee Nuclear Station, Unit 3," April 30, 2001.

6. U.S. NRC Bulletin 2001–01, "Circumferential Cracking of Reactor Pressure Vessel Head Penetration Nozzles," Aug. 3, 2001.

7. Bennetch, J. I., G. E. Modzelewski, L. L. Spain, and G. V. Rao, "Root Cause Evaluation and Repair of Alloy 82/182 J–Groove Weld Cracking of Reactor Vessel Head Penetrations at North Anna Unit 2," PVP–Vol. 437, Service Experience and Failure Assessment Applications ASME 2002, P. S. Lam, ed., American Society of Mechanical Engineers, New York, pp. 179–185, 2002.

8. U.S. NRC Information Notice 2002–11, "Recent Experience with Degradation of Reactor Pressure Vessel Head," March 12, 2002.

9. Alexandreanu, B., O. K. Chopra, and W. J. Shack, "Crack Growth Rates of Nickel Alloys from the Davis-Besse and V. C. Summer Power Plants in a PWR Environment," NUREG/CR-6921, ANL-05/55, November 2005.

10. Ruther, W. E., W. K. Soppet, and T. F. Kassner, "Corrosion Fatigue of Alloys 600 and 690 in Simulated LWR Environments," NUREG/CR-6383, ANL-95/37, April 1996.

11. PWR Materials Reliability Program Alloy 600 Issues Task Group, "Materials Reliability Program (MRP) Crack Growth Rates for Evaluating Primary Water Stress Corrosion Cracking (PWSCC) of Thick-Wall Alloy 600 Materials," MRP-55, Revision 1, Electric Power Research Institute, Palo Alto, CA, 2002.

12. Xu, H., S. Fyfitch, J.W. Hyres, "Laboratory Investigation of PWSCC of CRDM Nozzle 3 and Its J-Groove Weld on the Davis-Besse Reactor Vessel Head", Proc. of the 12th Intl. Conference on Environmental Degradation of Materials in Nuclear Power Systems—Water Reactors, G. T.R. Allen, P.J. King, and L. Nelson, eds., TMS (The Minerals, Metals & Materials Society), 2005.

13. American Society for Testing and Materials, "Standard Test Method for Measurement of Fatigue Crack Growth Rates," West Conshohocken, PA, ASTM E647-08, DOI 10.1520/E0647-08, www.astm.org, 2008.

14. American Society for Testing and Materials, "Standard Test Method for Determining a Threshold Stress Intensity Factor for Environment-Assisted Cracking of Metallic Materials," West Conshohocken, PA, ASTM E1681-03, DOI 10.1520/E1681-03R08, www.astm.org, 2008.

15. Electric Power Research Institute, "PWR Primary Water Chemistry Guidelines," Volume 1, Revision 4, EPRI, Palo Alto, CA, 1999.

16. Attanasio, S. A., and D. S. Morton, "Measurement of the Nickel/Nickel Oxide Transition in Ni-Cr-Fe Alloys and Updated Data and Correlations to Quantify the Effect of Aqueous Hydrogen on Primary Water SCC," Proc. 11th Intl. Conf. on Environmental Degradation of Materials in Nuclear Power Systems—Water Reactors, NACE International, Houston, TX, 2003.

17. Dominion Engineering, Inc., "Materials Reliability Program Crack Growth Rates for Evaluating Primary Water Stress Corrosion Cracking (PWSCC) of Alloy 82, 182, and 132 Welds," MRP-115, EPRI, Palo Alto, CA, 2004.

18. Ruther, W. E., W. K. Soppet, T. F. Kassner, and W. J. Shack, "Environmentally Assisted Cracking of Alloys 600 and 690 in Simulated LWR Water," in Environmentally Assisted Cracking in Light Water Reactors, Semiannual Report, January 1998-July 1998, NUREG/CR-4667, Vol. 26, ANL-98/30, pp. 25-32, March 1999.

19. Chopra, O. K., W. K. Soppet, and W. J. Shack, "Effects of Alloy Chemistry, Cold Work, and Water Chemistry on Corrosion Fatigue and Stress Corrosion Cracking of Nickel Alloys and Welds," NUREG/CR-6721, ANL-01/07, April 2001.

20. Norring, K., J. Engstrom, and P. Norberg, "Intergranular Stress Corrosion Cracking in Steam Generator Tubing: Testing of Alloy 690 and Alloy 600 Tubes," Proc. of the Third Intl. Symp. on Environmental Degradation of Materials in Nuclear Power Systems—Water Reactors, G. J. Theus and J. R. Weeks, eds., Metallurgical Society, Warrendale, PA, p. 587, 1988.

21. Norring, K., J. Engstrom, and H. Timblom, "Intergranular Stress Corrosion Cracking of Steam Generator Tubing: 25000 Hours of Testing of Alloy 690 and Alloy 600 Tubes," Proc. of the Fourth Intl. Symp. on Environmental Degradation of Materials in Nuclear Power Systems—Water Reactors, D. Cubicciotti, ed., NACE International, Houston, TX, p. 12-1, 1990.

22. Was, G. S. and K. Lian, "Role of Carbides in Stress Corrosion Cracking Resistance of Alloy 600 and Controlled-Purity Ni-16% Cr-9% Fe in Primary Water at 360 °C," *Corrosion*, **54** (9), 675, 1998.

23. Hertzberg, J. L., and G. S. Was, "Isolation of Carbon and Grain Boundary Carbide Effects on the Creep and Intergranular Stress Corrosion Cracking Behavior of Ni-16Cr-9Fe-xC Alloys in 360 °C Primary Water," *Metallurgical and Materials Transactions A*, **29** (3A), 1035-1046, 1998.

24. Boland, A.T. to A.Barry, Davis-Besse Nuclear Power Station Special Inspection to Review Flaws in the Control Rod Drive Mechanism Reactor Vessel Closure Head Nozzle Penetrations 05000346/2010-008 (DRS) and Exercise of Enforcement Deiscretion, http://adamswebsearch2.nrc.gov/webSearch2/main.jsp?AccessionNumber='ML102930380'

25. Alexandreanu, B., and G. S. Was, "Grain Boundary Deformation-Induced Intergranular Stress Corrosion Cracking of Ni-16Cr-9Fe in 360°C Water," *Corrosion*, **59** (8), 705, 2003.

Nuclear Engineering Division
Argonne National Laboratory
9700 South Cass Avenue, Bldg. 212
Argonne, IL 60439-4838

www.anl.gov

Argonne National Laboratory is a U.S. Department of Energy
laboratory managed by UChicago Argonne, LLC